Centro de Investigación Científica de Yucatán, A.C.

Posgrado en Ciencias Biológicas

MAPEO DE LA EDAD Y LA BIOMASA AÉREA DE BOSQUES TROPICALES SECOS DE LA PENÍNSULA DE YUCATÁN

Tesis que presenta

STEPHANIE PATRICIA GEORGE CHACÓN

En opción al título de

DOCTORA EN CIENCIAS

(Ciencias Biológicas: OPCIÓN RECURSOS NATURALES)

Mérida, Yucatán, México

2022

CENTRO DE INVESTIGACIÓN CIENTÍFICA DE YUCATÁN, A. C.
POSGRADO EN CIENCIAS BIOLÓGICAS

RECONOCIMIENTO

Por medio de la presente, hago constar que el trabajo de tesis de **Stephanie Patricia George Chacón** titulado **"Mapeo de la edad y la biomasa aérea de bosques tropicales secos de la Península de Yucatán",** fue realizado en la **Unidad de Recursos Naturales**, línea de Cambio Global, Laboratorio de Sistemas de Información Geográfica del **Centro de Investigación Científica de Yucatán, A.C**. bajo la dirección del **Dr. José Luis Hernández Stefanoni**, dentro de la opción de **Recursos Naturales**, perteneciente al Programa de Posgrado en Ciencias Biológicas de este Centro.

Atentamente

Dra. Cecilia Hernández Zepeda
Directora de Docencia

Mérida, Yucatán, México, a 10 de marzo de 2022

DECLARACIÓN DE PROPIEDAD

Declaro que la información contenida en la sección de Materiales y Métodos, los Resultados y Discusión de este documento proviene de las actividades de investigación realizadas durante el período que se me asignó para desarrollar mi trabajo de tesis, en las Unidades y Laboratorios del Centro de Investigación Científica de Yucatán, A.C., y que a razón de lo anterior y en contraprestación de los servicios educativos o de apoyo que me fueron brindados, dicha información, en términos de la Ley Federal del Derecho de Autor y la Ley de la Propiedad Industrial, le pertenece patrimonialmente a dicho Centro de Investigación. Por otra parte, en virtud de lo ya manifestado, reconozco que de igual manera los productos intelectuales o desarrollos tecnológicos que deriven o pudieran derivar de lo correspondiente a dicha información, le pertenecen patrimonialmente al Centro de Investigación Científica de Yucatán, A.C., y en el mismo tenor, reconozco que si derivaren de este trabajo productos intelectuales o desarrollos tecnológicos, en lo especial, estos se regirán en todo caso por lo dispuesto por la Ley Federal del Derecho de Autor y la Ley de la Propiedad Industrial, en el tenor de lo expuesto en la presente Declaración.

Stephnie G

Stephanie Patricia George Chacón

Este trabajo se llevó a cabo en la Unidad de Recursos Naturales del Centro de Investigación Científica de Yucatán, A.C., y forma parte del proyecto titulado Forests 2020 bajo la dirección del Dr. José Luis Hernández Stefanoni.

AGRADECIMIENTOS

Al CONACyT por la beca de doctorado otorgada para el CVU 622704.

A los miembros de mi comité tutorial, predoctoral y revisor.

A Fernando Tun, técnico de la Unidad de Recursos Naturales, por todo su apoyo tanto en campo como en el laboratorio.

A mis compañeros del Laboratorio de Sistemas de Información Geográfica del CICY, por su compañía y su apoyo.

A Claudia Ramírez, por revisar una versión preliminar de esta tesis.

A mi comité tutorial por guiarme en cada paso, y siempre aportarme ideas para la mejora de mi formación académica, y para alimentar el trabajo de una manera constructiva.

A mi comité revisor, por el tiempo y esfuerzo para la revisión de esta tesis y cuyos comentarios ayudaron al enriquecimiento de esta tesis.

LISTA DE LOS PRODUCTOS GENERADOS

Artículo 1: Mapping the spatial distribution of stand age and aboveground biomass from Landsat time series analyses of forest cover loss in tropical dry forests

Artículo 2: Using satellite estimates of aboveground biomass to assess carbon stocks in a mixed-management, semi-deciduous tropical forest in the Yucatan Peninsula

DEDICATORIAS

A mi hijo Sebastián, quien motiva mis días y para quiero ser un ejemplo siempre.

A Claudia, que estuvo conmigo en cada paso, en cada caída y en cada desvelo.

A mis tres madres.

ÍNDICE

LISTADO DE FIGURAS

LISTADO DE CUADROS

ABREVIATURAS

CO_2	Dióxido de carbono
LiDAR	Light Detection and Ranging
ALOS	Advanced land Observing Satellite
PALSAR	Phased Array L-type Synthetic Aperture Radar
AGB	Aboveground Biomass
REDD+	Reducción de Emisiones por Deforestación y Degradación
UNFCCC	United Nations Framework Convention on Climate Change
IPCC	Panel Intergubernamental de Cambio Climático
INFyS	Inventario Nacional Forestal y de Suelos
ESA	European Space Agency
SAR	Synthetic Aperture Radar
FAO	Food and Agriculture Organization
DN	Diámetro Normal
CMNUCC	Convención Marco de las Naciones Unidas sobre Cambio Climático
NDC	Contribución Nacionalmente Determinada
LGCC	Ley General de Cambio Climático
OLS	Ordinary Least Squares
TCH	Total Canopy Height
LOO	Leave one out
NDVI	Normalized Difference Vegetation Index
BFAST	Breaks for Additive and Seasonal Trend
EP	El Palmar
KK	Kaxil Kiuic
FCP	Felipe Carrillo Puerto
R2	Coeficiente de determinación R cuadrada
RMSE	Root Mean Square Error
ASM	Angular Second Moment
SNIGF	Sistema Nacional de Información y Gestión Forestal

RESUMEN

La información espacialmente explícita y precisa de la biomasa aérea es esencial para conocer el papel de los bosques tropicales en el ciclo global de carbono y reducir la incertidumbre sobre la magnitud de los almacenes y emisiones de CO_2 ocasionadas por la deforestación y la degradación. Las estimaciones globales de almacenes de carbono terrestre tienden a subestimar la biomasa aérea de los bosques tropicales secos maduros y a sobreestimar la biomasa de bosques en edades sucesionales tempranas. Además, en muchos casos estas estimaciones carecen de protocolos apropiados para la propagación de la incertidumbre.

Debido a la estrecha relación entre la biomasa y la edad de los bosques, la incorporación de información espacialmente explícita de la edad del bosque puede ser importante para reducir la sobreestimación de la biomasa aérea en bosques jóvenes. Al utilizar el archivo histórico de imágenes Landsat, es posible obtener información espacialmente explícita de la edad del bosque a una resolución de 30 m, e identificar los cambios en la cobertura forestal a través del tiempo. Por otra parte, los datos del sensor LiDAR proveen de información precisa sobre la estructura del bosque, lo que permiten una estimación precisa de la biomasa área. Sin embargo, no se encuentran disponibles datos de LiDAR que cubran completamente muchos bosques tropicales en el mundo. Una alternativa para utilizarlos es reescalarlos a escala regional por medio de información continua, generalmente de otros sensores pasivos o activos. Los sensores pasivos únicamente proporcionan información de los estratos más altos del dosel y pueden ser afectados por nubes y humo, aunque pueden tener mayor resolución espacial. Los sensores activos, en cambio, pueden penetrar el dosel, no son afectados por nubes y humo, pero pueden ser afectados por la topografía y el contenido de humedad en la vegetación. La combinación de estos sensores ha sido poco explorada para la estimación de biomasa aérea, sin embargo, podría mejorar la precisión de las estimaciones al superar las limitaciones individuales de cada tipo de sensor.

El presente estudio busca aportar información y mejoras metodológicas que permitan reducir la incertidumbre de las estimaciones de la biomasa aérea de tres paisajes bosques tropicales secos de la Península de Yucatán. Para lograr esto, se utilizaron dos métodos principales: (i) incorporación de información espacialmente explícita de la edad del bosque, obtenida de la distribución espacial del año de pérdida de cobertura forestal identificado a partir de series de tiempo de imágenes Landsat en tres coberturas forestales: bosque tropical caducifolio, subcaducifolio y subperennifolio (ii) mediante el escalamiento de datos LiDAR a escala regional por medio de la combinación de Sentinel 2 A, un sensor pasivo, y ALOS PALSAR, un sensor activo. Adicionalmente, se realizó la evaluación de la distribución de la biomasa aérea en diferentes categorías de protección y manejo de un bosque tropical subcaducifolio.

La pérdida de cobertura forestal fue estimada con mayor precisión en el bosque tropical subperennifolio, mientras que fue subestimada en el bosque tropical caducifolio y subcaducifolio, donde, se detectaron las mayores áreas de pérdida y un incremento en el área de pérdida de cobertura vegetal del año 2000 hasta el año 2020. La estimación espacialmente explícita de la edad se obtuvo a partir del último año de pérdida forestal para cada año. Utilizando esta información y la relación de la biomasa aérea y la edad del bosque, se obtuvieron mapas de biomasa para bosques menores a 20 años cuya media y rangos fueron más similares a la biomasa estimada con datos de campo, en comparación con estudios previos de estimación a través de sensores remotos realizados en el área.

Por otro lado, la combinación de sensores permitió la estimación de la biomasa aérea de manera más precisa y con menor error (R^2 = 0.70, %RMSE = 27.8 %) que por separado (ALOS R^2 = 0.50 %RMSE = 36.2, Sentinel R^2 = 0.66, %RMSE = 29.5). La validación independiente indica que la precisión es mucho mayor dentro del área de calibración (R^2 = 0.49, %RMSE = 24.6) que fuera de ella (R^2 = 0.17, %RMSE = 39.3), sin embargo, el 94 % de las observaciones se encontraron dentro de los límites de la predicción.

Se encontraron diferencias en la distribución de valores de biomasa entre categorías de protección, lo que resalta las ventajas de las áreas protegidas para conservar la biomasa aérea de bosques tropicales secos. De manera importante, se señala que las áreas designadas como aptas para restauración presentan grandes áreas con valores bajos de biomasa que de ser conservadas o restauradas podrían representar un secuestro importante de carbono en los bosques tropicales secos de la Península de Yucatán.

ABSTRACT

Spatially explicit information on the aboveground biomass (AGB) of tropical forests is essential for reducing uncertainty in CO_2 emissions due to deforestation and degradation and to understand the role of tropical forests in the global carbon cycle. Global estimations of the terrestrial carbon stock in AGB tend to underestimate the AGB contained in tropical dry forests, overestimate the AGB of forests in early ages of succession and/or lack appropriate protocols for the propagation of uncertainty throughout the estimation process.

Because of the strength of the relationship between AGB and forest age, taking into account spatially explicit information of forest age, may reduce the overestimation of AGB in young forests. Through the Landsat archive it is possible to obtain spatially explicit information of forest cover loss, which can be used to estimate forest age, at 30 m every 16 days. On the other hand, LiDAR provides precise information of forest structure, however, is unavailable for large parts of the tropics, or available discontinuously, in patches across many tropical forests. One alternative for using these data to map AGB can be to upscale them to a regional scale using continuous information from passive and active sensors. Passive sensors provide information of the top canopy layers and can be affected by clouds or smoke, however, these often have high spatial resolutions. Meanwhile, active sensors can penetrate the canopy and provide structural information of the lower strata and are generally not affected by clouds nor smoke. The combination of information from both sensors has been less explored, although it could potentially leverage individual sensor's limitations.

The present study seeks to provide information which allows to reduce the uncertainty in AGB estimations of three tropical dry forests of the Yucatan Peninsula. To achieve this, two approaches were followed: (i) estimation of AGB from spatially explicit information of the timing of forest cover loss obtained by time series analysis in three forest covers of the Yucatan Peninsula from the year 2000 until 2020 and (ii) by the upscaling of LiDAR data to regional scale using a combination of ALOS PALSAR, an active sensor and Sentinel 2, a passive sensor, in a semi deciduous tropical dry forest with mixed management and conservation areas.

Forest cover loss was estimated with a higher precision in semievergreen tropical forests, while there was a clear underestimation for the semi-deciduous and deciduous forests. Critically, the largest areas of forest cover loss and an increasing trend in deforestation area were found in these forests. Forest age was calculated from the time of last deforestation event onward. AGB

for < 20-year-old forests was obtained using this information and the relationship between forest age and AGB obtained from chronosequence data. The ranges and mean AGB obtained from this approach were more similar to field estimated AGB than other estimations from the same areas.

On the other hand, in a semi deciduous tropical dry forest the combination of sensors provided the most precise estimations of AGB (R^2 = 0.70, %RMSE = 27.8 %) compared to estimations with individual sensors (ALOS R^2 = 0.50 %RMSE = 36.2, Sentinel R^2 = 0.66, %RMSE = 29.5). A spatially independent validation indicated a much higher fit (R^2 = 0.49) inside the LiDAR calibration area than outside (R^2 = 0.17), however 94% of observations were found within our 95% confidence interval, indicating a robust prediction of errors. Important differences in the distribution of AGB were found among management and conservation categories, highlighting the usefulness of natural protected areas for the conservation of AGB in tropical forests. Importantly, areas designated for restoration show large areas of low AGB, which could, through natural regeneration and given enough time, represent a significant carbon sequestration in the tropical dry forests of the Yucatan Peninsula.

INTRODUCCIÓN

Los bosques proveen de recursos forestales maderables y no maderables; contribuyen a la biodiversidad global dado que albergan la mayor diversidad terrestre de plantas y animales terrestres; protegen los suelos; y regulan los ciclos biogeoquímicos (Pan et al., 2011; Bonan, 2008). Además, los bosques juegan un papel importante en el ciclo de carbono global y en la mitigación de los efectos adversos del calentamiento global, dado que capturan dióxido de carbono 'CO_2' y almacenan el carbono en su biomasa y en el suelo. Sin embargo, procesos ecológicos como la respiración y la mortalidad, así como perturbaciones provenientes de diversas fuentes (naturales, como huracanes e incendios forestales o antrópicos como la deforestación) liberan cantidades importantes de CO_2 a la atmósfera. Estos procesos varían de acuerdo con la edad y el tipo de bosque, entre otros factores, lo cual implica que algunos bosques, bajo algunas circunstancias, actúan como fuentes importantes de emisiones de CO_2 (Houghton, 2005).

La comprensión del papel de los bosques en el ciclo de carbono global, y la predicción de sus cambios a través del tiempo es importante ante el aumento de temperatura ¿ambiental? derivado del calentamiento global. Para ello es necesario obtener estimaciones precisas de los almacenes y flujos de carbono de los diferentes tipos de bosque y de sus cambios a través del tiempo. En la actualidad, las tasas de emisión de gases de efecto invernadero por medio de la deforestación y la degradación del bosque son considerados los componentes más inciertos en el ciclo de carbono global (Mitchard 2018; Pan et al., 2011). Esto se debe, en parte, a la dificultad de obtener estimaciones espacialmente explícitas precisas del carbono almacenado en diferentes tipos de bosques a través del tiempo. Esta información puede ser de utilidad para crear programas internacionales dedicados a la mitigación del cambio global, así como para diseñar y aplicar estrategias de conservación y manejo a nivel local y regional que aseguren la conservación de los servicios ecosistémicos que proveen los bosques (Houghton et al., 2009).

Algunos esfuerzos internacionales se dirigen a mejorar las estrategias de mitigación de los efectos del cambio climático global a través de la implementación de programas internacionales, como el programa REDD+ (Reducción de las Emisiones por Deforestación y Degradación) de la Convención Marco de las Naciones Unidas sobre el Cambio Climático (CMNUCC) (IPCC 2014; 2006). Sin embargo, la estimación de los almacenes de carbono debe cumplir con lineamientos específicos del Panel Intergubernamental de Cambio Climático (IPCC por sus siglas en inglés), una tarea desafiante, especialmente en áreas donde la información precisa y/o suficiente del contenido de carbono es escasa, y la dinámica de sus procesos de almacenamiento y ciclado no se ha comprendido a cabalidad (Houghton et al., 2009).

La biomasa aérea de los bosques es un almacén importante de carbono, dado que aproximadamente el 47 % de su composición escarbono (Martin & Thomas, 2011). Sin embargo, es el almacén más susceptible a ser emitido a la atmósfera por medio de eventos de deforestación (pérdida de cobertura total), y procesos de degradación (pérdida del contenido de biomasa sin una pérdida de cobertura total) (Houghton et al., 2009). Es importante señalar que los esfuerzos internacionales dirigidos a la estimación de la biomasa aérea se han enfocado principalmente en bosques templados. Sin embargo, las tasas de deforestación a gran escala en los bosques tropicales son mucho mayores en comparación con los bosques templados (Bastin et al., 2019; Crowther et al., 2015; FAO, 2016). Dada la gran magnitud de la incertidumbre de las estimaciones de emisiones por deforestación y degradación en áreas tropicales (Houghton et al., 2009; Pan et al., 2011), los esfuerzos deben ser redirigidos hacia la obtención de estimaciones precisas de la biomasa aérea de los bosques tropicales, especialmente cuando se estima que las áreas tropicales contienen alrededor del 50 % del carbono del mundo (Pan et al., 2011). Adicionalmente, bajo escenarios de enriquecimiento de carbono atmosférico, aumento de temperatura e incremento en la variabilidad de los regímenes pluviales, la capacidad de los bosques para almacenar carbono será afectada, y el tiempo de residencia del carbono se verá disminuido (Büntgen et al., 2019). Por otro lado, debido al aumento de la temperatura y la variabilidad en los regímenes de precipitación proyectados en los escenarios de cambio climático, se proyecta que los bosques tropicales más secos puedan convertirse en emisores netos de carbono (Goodman & Herold, 2014).

Algunos intentos previos para la estimación de la biomasa aérea en áreas tropicales (Avitabile et al., 2016; Cartus et al., 2014; Baccini et al., 2012; Saatchi et al., 2011) presentan grandes incertidumbres asociadas. Incluso, se ha estimado que existen grandes diferencias entre los productos de estas estimaciones y que potencialmente subestiman la biomasa aérea de los bosques tropicales secos maduros y sobreestiman la biomasa en bosques de edades de sucesión tempranas (Hernández-Stefanoni et al., 2020). Las diferencias en los protocolos de estimación de la biomasa aérea con datos de campo, insumos de percepción remota utilizados, y/o algoritmos de análisis de datos, incrementan la variabilidad en las estimaciones de biomasa aérea de bosques tropicales y reducen la comparabilidad de los resultados. Esto sin mencionar el hecho alarmante de que el papel de los bosques tropicales en el ciclo global de carbono, la magnitud de sus emisiones de CO_2 y el potencial secuestro de carbono que representa, pueden estar sesgados o erróneos (Mitchard 2018; Mitchard et al., 2013). Por lo tanto, es clave identificar las fuentes de variabilidad para reducir la incertidumbre asociada a las estimaciones de biomasa aérea para fin de redirigir nuevas estrategias de estimaciones espacialmente explícitas y obtener resultados más precisos, consistentes y comparables.

Existen varias consideraciones importantes para obtener estimaciones precisas de biomasa aérea en los bosques tropicales. Primero, la disponibilidad de datos de campo de referencia para grandes áreas. En México, existe un muestreo de la vegetación a gran escala que proporciona datos de la estructura de la vegetación para todo el país: El Inventario Nacional Forestal y de Suelos (INFyS). Sin embargo, a pesar de la gran magnitud de este inventario, es necesario obtener estimaciones continuas a escala de paisaje, lo cual es posible por medio de la percepción remota.

Los sensores pasivos ofrecen imágenes de diferentes resoluciones espectrales, espaciales y temporales de grandes extensiones y/o áreas inaccesibles. Sin embargo, uno de los retos principales en su utilización para la estimación de biomasa aérea, es la comprensión de los factores que controlan su variación espacial a nivel regional y local, con lo cual se puedan obtener variables informativas que tengan un significado ecológico y que puedan ser medidas fácilmente por medio de la percepción remota. La expansión urbana acelerada y la conversión de bosques a terrenos agrícolas son las principales causas de la deforestación o pérdida de cobertura forestal en los trópicos (Houghton et al., 2009). El abandono posterior de los terrenos agrícolas resulta en un paisaje compuesto de mosaicos de parches de vegetación con diferentes edades de abandono. Dado que los bosques aumentan en biomasa, y por tanto en el carbono almacenado a medida que crecen, la edad del bosque es un factor clave para la estimación del carbono almacenado en los bosques (Becknell & Powers, 2014; Coursolle et al., 2012). La obtención de estimaciones espacialmente explícitas de la edad del bosque puede ayudar a reducir incertidumbres en la estimación de los almacenes de carbono.

En particular, los archivos históricos de imágenes de satélite Landsat, ofrecen cobertura global de imágenes con resolución espacial de 30 m cada 16 días. Esta información puede ser de utilidad para detectar cambios en la cobertura de los bosques y, a partir de ellos estimar su edad. Sin embargo, con una resolución de 30 m existe la posibilidad de obtener la información espectral de diferentes tipos de bosque, o bien, bosques de diferentes edades en un solo píxel. Asimismo, Landsat es potencialmente incapaz de diferenciar doseles de diferentes edades con estructuras similares a causa de su baja resolución radiométrica (8 – 12 bits), y presenta efectos de sombreado en sitios de mayor complejidad topográfica (Lu, 2006; Lu et al., 2012) lo que dificulta su uso para estimar la biomasa aérea a partir de información de la estructura de la vegetación. Otras plataformas como Sentinel 2A de la Agencia Espacial Europea (ESA por sus siglas en inglés), tienen gran potencial debido a su alta resolución espacial (10 m), sin embargo, la información de los estratos bajos puede estar ausente o no ser capturada adecuadamente, ya que los sensores pasivos únicamente proporcionan información de los estratos más elevados del dosel. Para superar esta limitación, se pueden calcular medidas de textura de la imagen que tienen potencial para capturar variaciones en la estructura del bosque, a partir de las variaciones en los valores de reflectancia de la imagen (Hernández-Stefanoni et al., 2020).

Por otra parte, los sensores activos como el Radar de Apertura Sintética (Synthetic Aperture Radar, SAR), ofrecen información continua de la estructura de la vegetación. La información obtenida a partir de sensores activos puede superar limitaciones de los sensores ópticos dado que la señal de retrodispersión no se ve afectada por efectos atmosféricos como la presencia de nubes. Igualmente, LiDAR (Light Detection and Ranging) provee información precisa de la estructura tridimensional de la estructura de la vegetación. Esto permite mejorar la estimación al capturar información precisa de los estratos medios y bajos por lo que el rango de estimación será más amplio. Asimismo, la alta resolución espacial de LiDAR permite ser re-escalada a la extensión de imágenes ópticas (Matasci et al., 2018), para obtener estimaciones continuas de la estructura de la vegetación. La combinación de información de LiDAR e imágenes ópticas puede complementar los datos de campo para proveer estimaciones espacialmente explícitas, a nivel de pixel, de la biomasa aérea de los bosques (Asner et al., 2018) en diferentes resoluciones espaciales y temporales. Igualmente, la combinación de información de sensores pasivos y activos permite superar las limitaciones individuales de los sensores y, por lo tanto, potencialmente aumentar la precisión y reducir la incertidumbre de la estimación.

Los dos objetivos principales de este trabajo fueron: (i) estimar la biomasa aérea a partir de la edad del bosque obtenida mediante el último año de pérdida de cobertura forestal e información de la relación biomasa- edad obtenida por medio de cronosecuencias, en tres tipos de bosques secos con diferentes usos de suelo de la Península de Yucatán y comparar las estimaciones con trabajos previos en los mismos sitios de estudio y datos de campo de referencia; (ii) estimar la biomasa aérea por medio del escalamiento en dos etapas, la primera de datos de campo, a datos LiDAR y posteriormente con las estimaciones de biomasa en áreas con datos LiDAR de manera continua a la extensión de las imágenes ópticas. En esta última utilizando sensores pasivos, activos y/o su combinación. Se espera encontrar una mayor área de pérdida de cobertura forestal en los bosques más secos donde el uso de suelo más extensivo es la agricultura de roza tumba y quema, y donde la estructura de la vegetación facilita el desmonte. Por otra parte, se espera una disminución en la sobre-estimación de la biomasa aérea de bosques jóvenes al incorporar información de la edad debido a que ésta refleja la recuperación de la biomasa a lo largo de la sucesión. Por otra parte, se espera que al realizar el escalamiento de datos LiDAR para estimar la biomasa, la combinación de sensores pasivos y activos minimice la saturación y produzca una estimación más precisa de la biomasa aérea que utilizando cada sensor por separado.

CAPÍTULO I

1.1 ANTECEDENTES

1.1.1 CAMBIO CLIMÁTICO GLOBAL

Existe suficiente evidencia para creer que la actividad humana ha ocasionado el calentamiento global. Esta evidencia incluye un incremento sustancial en las temperaturas atmosféricas y oceánicas, la reducción de los glaciares árticos, el incremento del nivel del mar, la acidificación de los océanos, alteraciones a la criósfera y el ciclo del agua en comparación con la simulación de cambios climáticos proyectados excluyendo la actividad humana (IPCC 2021; 2014; 2006). Por ende, estos cambios no pueden ser atribuidos únicamente a forzamientos naturales como variaciones en la radiación solar, volcanes o variabilidad interna (Ciais et al., 2013).

La temperatura media superficial de la tierra se ha incrementado de 0.5 a 1.3 °C desde el inicio era industrial (ca.1900), cuya causa más probable es el aumento en la concentración de gases de efecto invernadero (IPCC 2021). Los gases de efecto invernadero (GEI) representan la fase gaseosa de los ciclos biogeoquímicos, que controlan las transformaciones y flujos de elementos entre la atmósfera, el océano y la tierra, por medio de procesos bióticos y abióticos. Los GEI absorben y emiten radiación en el rango del espectro infrarrojo ocasionando cambios en el flujo energético de la tierra, fenómeno llamado forzamiento radiativo (medido en W/m^2). Por ende, el cambio en la composición de la atmósfera (concentración de los GEI) produce cambios en los parámetros climáticos de la tierra (Ciais et al., 2013). El dióxido de carbono (CO_2), metano (CH_4) y el óxido nitroso (N_2O) constituyen el 80% de la concentración de GEI que se han incrementado desde la era industrial debido a la actividad humana, siendo el CO_2 el GEI de larga vida con el mayor forzamiento radiativo. El incremento en la concentración de estos gases en la atmósfera es ocasionado por la quema de combustibles fósiles como fuente primordial de energía y el cambio del uso de suelo, particularmente la reducción de áreas de bosque debido a la expansión de campos agrícolas y áreas urbanas (IPCC 2014).

Se ha reportado que la concentración de CO_2 atmosférico ha incrementado de 390.5 ppm en 2011 (Ciais et al., 2013) a 419 ppm hasta el año 2021 (IPCC, 2021). Desde el inicio de la revolución industrial, las emisiones antrópicas totales estimadas son de 555 ± 85 GtC (10^9 ton de carbono), de los cuales 375 ± pueden ser atribuidos a la quema de combustibles fósiles y la producción de cemento y 180 ± 80 GtC al cambio de uso de suelo. La mitad de las emisiones fue removida de la atmósfera por sumideros en los reservorios del ciclo de carbono: el reservorio oceánico almacenó 155 ± GtC y los reservorios terrestres comprendidos por la biomasa de vegetación y de suelos almacenaron 160 ± 90 GtC (Ciais et al., 2013).

El IPCC (2013) ha proyectado que la captura de carbono de los océanos se incrementará hasta 2100 correspondiendo al incremento en la concentración atmosférica de CO_2, sin embargo, el futuro de la captura de carbono terrestre es incierto, dado que algunas proyecciones apuntan a un sumidero de carbono (transferencia neta de carbono de la atmósfera hacia la tierra) y otras a una fuente neta (transferencia neta de carbono de la tierra a la atmósfera). El proceso de incrementar el carbono contenido en un almacén de carbono (diferente de la atmósfera) es llamado secuestro o captura de carbono (IPCC 2006). Es importante señalar que el reservorio de carbono en los suelos se encuentra protegido y no es fácilmente liberado a la atmósfera, sin embargo, el carbono contenido en la biomasa aérea de los bosques es liberado por medio de la deforestación, causada por la conversión de los bosques a otros usos de suelo e incendios naturales y derivados de actividades antrópicas. La falta de estimaciones precisas de la distribución espacial de la biomasa aérea de los bosques es un factor importante que contribuye a la incertidumbre de las emisiones por deforestación y, por consiguiente, de las estimaciones del ciclo de carbono terrestre (Pan et al., 2011).

1.1.2. EL CICLO DE CARBONO EN LOS BOSQUES

El papel de los sistemas naturales en el ciclo de carbono es crucial. Los bosques cubren el 30% de la superficie terrestre (4.04 mil millones de hectáreas) (FAO, 2016) y contienen el reservorio de carbono más grande en su biomasa y suelos. Sin embargo, el carbono es liberado a la atmósfera a través de procesos naturales como la respiración y la descomposición (Goodman & Herold 2014). La vegetación terrestre cicla alrededor de 120 GtC por año, fijando alrededor de 123 GtC y liberando 119 GtC a través de la respiración vegetal (Figura 1, Ciais et al., 2013).

El ciclo de carbono en los bosques está conformado por una serie de reservorios de carbono donde este se almacena y acumula, y almacenes de carbono que están constantemente intercambiando carbono a través del tiempo. La diferencia neta entre la asimilación de CO_2 y su conversión a materia orgánica por medio fotosíntesis, y la oxidación de los carbohidratos y su liberación por medio de la respiración, determina la acumulación neta de carbono a través del tiempo. El carbono en la biomasa viva de plantas se distribuye en biomasa leñosa (tallos y ramas) y no leñosa (hojas, estructuras reproductivas, raíces y rizomas). El remanente corresponde en gran medida a la materia orgánica en suelos, que se origina a partir de la descomposición de hojarasca y la biomasa muerta de plantas, incluyendo madera muerta, importantes fuentes de nutrientes para el crecimiento vegetal. En los bosques de la biósfera el carbono se encuentra distribuido, el 44% en los suelos, el 42% en la biomasa (aérea y subterránea), mientras que el mantillo contiene 5% y la madera muerta 8% (Pan et al., 2011).

La productividad primaria bruta o fotosíntesis bruta es la cantidad total de CO_2 asimilado por la vegetación en el bosque (dosel, arbustos, hierbas, etc.). De esta, aproximadamente la mitad se utiliza para construir nuevo tejido durante el crecimiento y la reparación del tejido existente o manutención del tejido. La suma de estos dos procesos (respiración por crecimiento, y respiración de manutención) constituye la Respiración autótrofa, la cual libera CO_2 a la atmósfera (Gower et al., 2003). Entonces, la productividad primaria neta es la diferencia entre la productividad primaria bruta y la respiración autótrofa, determina la acumulación neta de biomasa y se expresa en unidades de carbono por unidad de área por año. La diferencia entre productividad primaria neta y respiración heterótrofa (respiración y descomposición de materia orgánica por organismos vivos) sería la producción ecosistémica, que es el intercambio neto de CO_2 entre la atmósfera y los ecosistemas terrestres, incluyendo la vegetación y el suelo (Gower et al., 2003).

Los reservorios de carbono terrestre de la vegetación contienen de 450 a 650 GtC (Friedlingstein et al., 2020). Se estima que 3.4 (2.5 – 4.3) GtC son absorbidos por la vegetación cada año, mientras que los flujos hacia a la atmósfera por cambio de uso de suelo se estiman en 1.6 (0.9 – 2.3) GtC. El balance indica que existe un secuestro neto de 1.8 (0.6 – 2.0) GtC por año (Friedlingstein et al., 2020).

1.1.3 LOS BOSQUES TROPICALES

Los reservorios terrestres de carbono que se encuentran en los bosques templados y tropicales, aportan el 60% de la fotosíntesis global (Pan et al., 2011); son responsables de aproximadamente 33% de la productividad primaria neta global (Clark et al., 2001; Field & Raupach, 2004); capturan 72 GtC por año y almacenan de 200 – 300 GtC (~25%) del carbono terrestre (Le Quéré et al., 2018, 2016). Sin embargo, estos bosques también liberan una cantidad similar de carbono a través de la respiración (Goodman & Herold 2014; Bonan 2008). Por lo tanto, pequeños cambios en el secuestro o la liberación de CO_2 a la atmósfera pueden resultar en una fuente o sumidero neto de carbono.

El papel de los bosques tropicales como fuentes o sumideros netos de carbono es altamente incierto. Las emisiones de carbono derivadas de la deforestación (remoción total de la cobertura forestal) y la degradación (remoción de una cantidad de carbono forestal, sin ocasionar un cambio en la cobertura, o transición hacia cualquier categoría “no bosque”) en bosques tropicales puede alcanzar una magnitud de 3.5 GtC por año (Baccini et al., 2017). Asimismo, se estima que la superficie de pérdida de cobertura forestal se ha incrementado en la última década (Hansen et al., 2013), de la cual una gran parte se atribuye a la rápida expansión de campos agrícolas (FAO 2016). Sin embargo, es difícil obtener estimaciones precisas de la biomasa perdida a causa de la deforestación debido a las diferencias entre las estrategias de estimación. Incluso existen diferencias importantes en las tendencias de pérdida de bosque proyectadas para el futuro (Mitchard, 2018).

Hasta ahora, a pesar de la gran incertidumbre presente en las estimaciones de carbono en los bosques tropicales, la falta de estimaciones consistentes a través del tiempo, las diferencias entre los métodos de estimación y sus incertidumbres asociadas, el consenso general es que los bosques tropicales son aproximadamente neutrales excepto en años excepcionalmente cálidos en donde pueden actuar como fuentes netas de carbono (Baccini et al., 2017; Pan et al., 2011). Los sumideros de carbono se estiman en 2.7 ± 0.7 GtC por año, lo cual es aproximadamente el 70% del sumidero bruto de carbono en los bosques, sin embargo, liberan una cantidad similar a través de la respiración y la deforestación (2.8 ± 0.5 GtC por año) (Pan et al., 2011). Igualmente, un estudio de simulación señala que la capacidad de almacenamiento de los bosques se verá reducida en temperaturas más cálidas debido a un aumento en la mortalidad y, por tanto, una disminución el tiempo de residencia del carbono en los bosques (Büntgen et al., 2019).

1.1.3.1 LOS BOSQUES TROPICALES SECOS

Los bosques tropicales secos (BTS) ocupan alrededor de 519,597 km^2 de la superficie terrestre global de los cuales más del 50% se encuentra en el continente americano, y México contiene el 38 % de éstos (Portillo-Quintero & Sánchez-Azofeifa, 2010; Sanchez-Azofeifa et al., 2013). Estos bosques presentan menores alturas y estructuras más simples (1 o 2 estratos) que sus contrapartes más húmedas (Murphy & Lugo, 1986; Pennington et al., 2009) y se caracterizan por presentar una marcada estacionalidad, con una estación seca que puede durar de 5 a 6 meses. Debido a esto, su vegetación consiste predominantemente de especies tolerantes a la sequía (Murphy & Lugo 1986). Los BTS se distribuyen en toda el área tropical donde la temperatura media anual es mayor a los 25°C y la precipitación varía de 250 a 2000 mm por año, por lo que varían estructural y funcionalmente a lo largo de gradientes de precipitación (Murphy & Lugo, 1986). Estructuralmente pueden dividirse en bosques bajos (menores a 15 m de altura) y medianos (de 15 a 30 m), y de acuerdo con su porcentaje de árboles deciduos pueden también dividirse en caducifolios (contienen más del 75 % de árboles caducifolios), subcaducifolios (contienen del 50 al 75 % de árboles caducifolios) y subperennifolios (contienen el 25 % de árboles caducifolios).

Sumando a su heterogeneidad y dinámica natural, los BTS se encuentran sujetos a grandes presiones de conversión para la producción agrícola y el establecimiento y expansión de las ciudades (Portillo-Quintero y Sánchez-Azofeifa 2010). A su vez, estos bosques se encuentran en continua regeneración y expansión debido al establecimiento y abandono de terrenos agrícolas y/o a prácticas agrícolas comunes en los trópicos como la agricultura de roza, tumba y quema, práctica de agricultura tradicional donde un período de cultivo corto es sucedido por un período largo de recuperación (barbecho) (Portillo-Quintero y Sánchez-Azofeifa 2010; Houghton et al., 2009). Por esta razón los bosques secos representan tanto una fuente de emisiones de carbono por deforestación y degradación, como un sumidero de carbono debido a la regeneración y el crecimiento (Philipson et al., 2020; Chazdon, 2017; Griscom & Ashton, 2011; Vieira & Scariot, 2006). Debido a la falta de estimaciones espacialmente explícitas de la biomasa aérea, las emisiones por deforestación y degradación, y por lo tanto el potencial de mitigación o emisión de los bosques tropicales, continúan siendo el componente más incierto del ciclo de carbono global (Pan et al., 2011).

1.1.3.2. LOS BOSQUES TROPICALES SECOS DE LA PENÍNSULA DE YUCATÁN

La Península de Yucatán presenta un marcado gradiente de precipitación que varía desde los ambientes más secos del noreste de la Península con precipitación media anual de 500 mm hasta los 1500 mm en el sureste (Orellana et al., 2003; Islebe et al., 2015). A lo largo de este gradiente se extiende una de las mayores extensiones continuas de bosques tropicales secos en Latinoamérica (Dupuy et al., 2015) en donde se reconocen tres coberturas principales (Cuadro 1.1) en las cuales se centra este trabajo.

Cuadro 1.1. Características relevantes de los bosques en los que se centra este estudio: Extensión (ha), porcentaje que ocupan en la Península de Yucatán, características ambientales (precipitación y temperatura), fenológicas (porcentaje de especies deciduas) y usos de suelo predominantes de los bosques (Islebe et al., 2015, Durán y Contreras 2010; Rzedowski 2007, Orellana et al., 2003).

Tipo de cobertura	**Extensión (km) (% en la PY)**	**Precipitación (mma)**	**Temperatura °C**	**Porcentaje de Árboles deciduos**	**Uso de suelo**
Bosque tropical Caducifolio	914,808.35 (7 %)	500 – 800	26 – 27	> 75	Agricultura de temporal, y roza tumba y quema
Bosque tropical Subcaducifolio	1,987,633.98 (14 %)	800 – 1200	24 – 26	50 – 75	Agricultura de temporal, roza tumba y quema pastizales inducidos
Bosque tropical Subperennifolio	4,240,293.83 (31 %)	1100 – 1300	25 – 26	25 – 50	Agricultura de roza tumba y quema, extracción selectiva

Estos bosques han sido sujetos a diferentes presiones a lo largo de la historia. Los bosques caducifolios, los más secos del noreste de la Península, se han establecido principalmente en terrenos abandonados del estado de Yucatán donde previamente se cultivaba el henequén (*Agave fourcroydes* Lem.) (Ellis et al., 2017). El centro y suroeste de la Península contiene bosques subcaducifolios donde el uso principal es la agricultura de temporal y de roza, tumba y quema, con algunos terrenos dedicados a pastizales (Armenta-Montero et al., 2020). En el sureste de la Península, donde se encuentran los bosques subperennifolios, el uso de suelo más común es la extracción selectiva y el manejo comunitario (Ellis et al., 2017) y algunos pastizales para ganado (Armenta-Montero et al., 2020).

1.1.4. BIOMASA FORESTAL

Las plantas verdes asimilan el dióxido de carbono (CO_2) atmosférico a través de la fotosíntesis, proceso mediante el cual convierten el CO_2 en carbohidratos como glucosa y almidón (Chen et al., 2013; Malhi, 2012). Estos productos de la fotosíntesis son subsecuentemente usados para la construcción de biomasa, que es en esencia, tejido vegetal vivo.

Tejidos como las hojas, tallos o troncos, ramas y estructuras reproductivas constituyen la biomasa aérea, la cual se estima que constituye el 70% de la biomasa total; estructuras como las raíces, rizomas y otras estructuras de fijación al sustrato constituyen la biomasa subterránea, que representa el 30% restante (IPCC 2006). Adicionalmente, se estima que ~47% de la biomasa seca está constituida de carbono y que, en promedio, alrededor del 50 % del carbono total de una planta se encuentra almacenado en estructuras leñosas como los troncos y ramas (Martin & Thomas 2011). Dado que la biomasa aérea es vulnerable a la deforestación e incendios, cantidades importantes de carbono pueden ser liberadas a la atmósfera mediante la conversión de bosques a otros usos de suelo, la extracción de madera, e incendios naturales y derivados de actividades humanas (Goodman & Herold 2014, Houghton et al., 2009). Las interacciones entre la atmósfera y los bosques son dinámicas y complejas, especialmente en bosques tropicales donde incluso la deforestación a baja escala puede afectar las condiciones ambientales locales como la precipitación y la formación de nubes (Bonan 2008).

Además de los desastres naturales como los incendios forestales, eventos de sequía intensa, huracanes y disturbios ocasionados por el ser humano como la tala, incendios y el cambio de uso de suelo, la distribución espacial de la biomasa varía dependiendo de factores ambientales como la distribución de la precipitación en el espacio y el tiempo, la temperatura y variaciones locales en el contenido de nutrientes del suelo y procesos de interacción como la competencia (Bonan 2008, Houghton et al., 2009). Estudios previos sobre los principales factores de los que depende la distribución espacial de la biomasa aérea sugieren que los factores ambientales pueden ser los principales determinantes de la variación en la biomasa aérea de los bosques tropicales (Soriano-Luna et al., 2018; Adhikari et al., 2017), por lo tanto, tomar en cuenta estos factores para explicar la variación espacial de su biomasa aérea potencialmente podría aumentar la precisión y reducir el error en las estimaciones. Otra consideración importante en la estimación de la biomasa aérea es la variación temporal asociada a los disturbios naturales y antrópicos (IPCC 2006). Este factor es especialmente importante dado que las tasas de acumulación de biomasa en los bosques varían temporalmente, donde los bosques jóvenes acumulan biomasa a una tasa mayor que los bosques maduros (Houghton et al., 2009). Por lo tanto, la variación espacial de la biomasa aérea es afectada por el cambio de uso de suelo, la dinámica de disturbio-regeneración, y gradientes ambientales, edáficos y climáticos.

1.1.5. FACTORES QUE AFECTAN LA DISTRIBUCIÓN ESPACIAL DE LA BIOMASA AÉREA

1.1.5.1. SUCESIÓN SECUNDARIA Y EDAD SUCESIONAL DEL BOSQUE

Después de disturbios naturales o antrópicos severos no permanentes como los incendios forestales o la conversión de bosques a parcelas agrícolas o pastizales y su posterior abandono, los bosques sufren cambios direccionales en su estructura y composición, un proceso denominado sucesión secundaria (Chazdon, 2008; Chazon, 2014). Por lo tanto, los bosques pueden ser divididos en bosques primarios o maduros, y bosques secundarios o que se encuentran en un proceso de regeneración natural. En los bosques tropicales, emergen dos estrategias contrastantes que corresponden a dos limitaciones ambientales importantes: ambientes secos (con baja disponibilidad de agua) *versus* ambientes húmedos (con baja disponibilidad de luz). En los bosques donde la disponibilidad de agua no es un factor limitante (bosques húmedos), las plantas se encuentran limitadas por su capacidad para captar la luz solar. Durante las etapas tempranas de sucesión, cuando la luz no es limitante, las especies dominantes están caracterizadas por tener tasas de crecimiento más rápidas y una mayor eficiencia en la adquisición de recursos, aunque también una menor conservación de los recursos (especies pioneras); en cambio, en las etapas tardías de sucesión dominan las especies con tasas de crecimiento más lentas y una estrategia de mayor conservación de los recursos (Lohbeck et al., 2013).

En contraste, en ambientes con estaciones secas de mayor duración, las especies se encuentran limitadas por su capacidad de sobrevivir en ambientes de alta radiación y baja disponibilidad de agua (Poorter, 2009). Por lo tanto, estas especies se encuentran limitadas por la disponibilidad de agua, la temperatura del aire y la humedad relativa (Lebrija-Trejos et al., 2011). En etapas sucesionales tempranas, la radiación es mayor y la disponibilidad de agua es menor a causa de la disminución en la cobertura del dosel, por lo que las especies con estrategias conservadoras tienen una mayor probabilidad de sobrevivir. En contraste, durante la sucesión tardía, el estrés ambiental se ve considerablemente reducido, por lo que en rodales más viejos dominan las especies con una mayor eficiencia en la adquisición de recursos (Poorter et al., 2019; Markesteijn et al., 2011a; Markesteijn, et al., 2011b). Los cambios estructurales que ocurren en la vegetación durante la sucesión secundaria son el incremento en el área basal, biomasa y altura (Chazdon 2008). Este patrón ha sido observado tanto en bosques secos (Dupuy et al., 2012; Ruiz et al., 2005) como húmedos (Letcher et al., 2009; Feldpausch et al., 2007). Sin embargo, los patrones sucesionales de los bosques secos y húmedos difieren, por lo que la relación entre la biomasa y la edad podría cambiar a través de gradientes climáticos (Zhu et al., 2018; Chen et al., 2016; Poorter & Nagel, 2000). Por ejemplo, la densidad de la madera es mayor en las etapas tempranas de la sucesión en bosques secos, y disminuye conforme la edad avanza. En contraste, en bosques húmedos, la densidad de la madera es menor al inicio de la sucesión y se incrementa con la edad hasta convergir con la densidad de bosques secos (Poorter et al., 2019). Dado que la densidad de la madera es un atributo que tiene un impacto significativo en la biomasa aérea (Chave et al., 2005), la relación entre la biomasa y la edad entre estos dos ambientes podría ser diferente. Si bien la biomasa aumenta en función del tiempo hasta alcanzar un estado estable en el que los incrementos en la biomasa por crecimiento y reclutamiento son compensados por las pérdidas por mortalidad, la biomasa se recupera más rápidamente en las edades tempranas, mientras que los bosques maduros presentan una recuperación de biomasa más lenta al aproximarse al estado estable (Poorter et al., 2016). Esto ha sido observado en una gran variedad de bosques incluyendo los bosques tropicales secos (Hernández-Stefanoni et al., 2011; Ruiz et al., 2005). Sin embargo, la influencia de la edad sucesional del bosque en la cantidad de biomasa es multifactorial y compleja. Conforme los bosques crecen, diferentes factores tienen influencia en la distribución de la biomasa, entre ellos, variaciones temporales en las propiedades y disponibilidad de nutrientes del suelo (Guariguata & Ostertag, 2001). Generalmente, se espera una relación directa entre biomasa aérea y edad sucesional, sin embargo, la máxima cantidad de biomasa que un bosque puede alcanzar depende de factores que limitan el crecimiento (Turner, 2010). Asimismo, especies con tasas de crecimiento diferentes se establecen en etapas sucesionales conforme los bosques maduran, por lo tanto, la cantidad de biomasa de un bosque será directamente afectada por este proceso.

El estudio de la sucesión ecológica de los bosques puede ser de manera directa, utilizando parcelas que son monitoreadas para estudiar su estructura y composición a través del tiempo, sin embargo, pocos estudios cuentan con períodos de tiempo tan amplios como para obtener un panorama completo de la dinámica de los bosques. Frecuentemente, los estudios de la dinámica de sucesión ecológica de los bosques se llevan a cabo por medio de cronosecuencias, donde se muestrean y comparan parcelas de diferentes edades (se sustituye el tiempo por el espacio) (Guariguata & Ostertag 2001). Estos estudios, proveen de información sobre la estructura y composición en diferentes edades sucesionales, sin embargo, tienen limitaciones importantes que deben ser consideradas. Aunque la selección de los sitios debe ser muy ciudadosa para evitar diferencias en las condiciones ambientales como diferencias en el clima y el tipo de suelo, podrían presentar diferencias en la composición inicial, así como en la disponibilidad de semillas y nutrientes, e historia de uso de suelo, factores importantes que determinan los patrones de estructura y composición de los bosques (Chazdon 2008). Estas limitaciones conllevan a supuestos poco realistas, que limitan la información que aportan los estudios de cronosecuencias. Es importante considerar que en muchas ocasiones no es posible estandarizar las condiciones ambientales, historia de uso de suelo o condiciones topográficas. En particular, pueden existir diferencias importantes en la trayectoria sucesional de las parcelas ocasionadas por diferencias en condiciones iniciales subyacentes. Por ejemplo, las diferencias en la intensidad del disturbio inicial pueden ocasionar que bosques más maduros se regeneran en áreas donde el uso de suelo ha sido menos intensivo, lo cual ocasionaría una diferencia importante en la trayectoria sucesional con las parcelas donde el uso de suelo ha sido más intenso (Chazdon 2014). Las cronosecuencias son más útiles para predecir atributos que cambian de manera relativamente predecible a través del tiempo, tales como riqueza de especies o la acumulación de atributos como biomasa y materia orgánica del suelo, sin embargo, son menos útiles para predecir cambios en atributos más difusos, como la composición de especies (Walker et al., 2010).

1.1.5.2. PROPIEDADES DEL SUELO

Las propiedades del suelo varían en los bosques tropicales, y estas variaciones afectan las tasas de crecimiento, determinan el tamaño de los árboles (Becknell & Powers, 2014) y la productividad de los bosques tropicales (Quesada et al., 2012; Griscom & Ashton, 2011). Las propiedades del suelo, ya sea físicas o químicas, varían espacialmente a causa de la variación en las condiciones climáticas y geológicas. La distribución de micro y macro-nutrientes en suelos está fuertemente asociada con la distribución de las especies, y por lo tanto afecta la variación espacial de la biomasa y el almacén de carbono en los bosques (Quesada et al., 2012, Poorter et al., 2019). Propiedades físicas como la textura, la estructura y la profundidad tienen un gran impacto en la habilidad de las raíces para adquirir nutrientes y en la cantidad de agua que pueden retener. También, medidas de la fertilidad del suelo como la capacidad de intercambio catiónico, concentraciones de iones intercambiables como potasio (K+) y fósforo (P+) han mostrado asociaciones positivas con la biomasa aérea (Quesada et al., 2012; Slik et al., 2010). Sin embargo, la interacción de factores biogeográficos, edáficos y climáticos pueden oscurecer las relaciones entre estos factores, por ejemplo, algunas especies de rápido crecimiento están asociadas a suelos más fértiles, sin embargo, esto podría estar más relacionado con un componente biogeográfico (dado el acervo local de especies), que con un componente ambiental *per se* (Quesada et al., 2012).

1.1.5.3. FACTORES CLIMÁTICOS

Es ampliamente aceptado que la distribución de la vegetación está, hasta cierto punto, determinada por el clima. Sin embargo, la relación entre los factores climáticos y las propiedades de la vegetación no es simple, dado que los factores climáticos no actúan individualmente. La actividad de un factor tiene impacto sobre otros factores que pueden tener influencia decisiva sobre la distribución de las plantas. Estos factores incluyen la formación de suelo, la topografía, y la distribución de microorganismos y animales

Diversos estudios han intentado encontrar correlaciones entre factores climáticos y atributos de la vegetación, sin embargo, existe poca información acerca de la influencia de la variación en las condiciones climáticas sobre la distribución espacial de la biomasa aérea de los bosques. Se ha sugerido que la temperatura media y la precipitación anual, su combinación y la precipitación de la estación seca (Corona-Núñez et al., 2018; Reich et al., 2014), tienen un efecto en la distribución de la biomasa, junto con otros factores climáticos mencionados anteriormente. Sin embargo, existe la posibilidad de que estos factores tengan diferentes impactos en localidades distintas, debido a las capacidades y limitaciones intrínsecas de cada especie. Muchas de las relaciones propuestas entre factores climáticos y la cantidad de biomasa aérea de los bosques han sido evaluadas en un sólo tipo de vegetación, lo cual dificulta la extrapolación a otros tipos de vegetación; ya que se ha demostrado que no se cumplen cuando se consideran múltiples tipos de bosque. La biomasa de los bosques se ha asociado positivamente a la precipitación media anual y la precipitación de la época de sequía en los bosques tropicales secos, sin embargo, esta relación no se observa en bosques húmedos (Stegen et al., 2011). Un estudio reciente encontró que la precipitación local y un déficit climático de agua (la diferencia entre precipitación y evapotranspiración en la estación seca) están relacionados con una recuperación más rápida de la biomasa en bosques secundarios neotropicales (Poorter et al., 2016). Asimismo, Ortiz-Reyes et al. (2021) demuestran que variables climáticas y espectrales, especialmente aquellas relacionadas con la precipitación y la temperatura, son capaces de explicar la variabilidad de la biomasa aérea en selvas medianas subcaducifolias y subperennifolias de la Península de Yucatán.

1.1.6 MÉTODOS DE ESTIMACIÓN DE BIOMASA AÉREA EN BOSQUES

1.1.6.1. ESTIMACIÓN DE BIOMASA AÉREA EN CAMPO

Se ha sugerido previamente que uno de los componentes más importantes para incrementar la precisión de las estimaciones espacialmente explícitas de la biomasa aérea es la disponibilidad de datos de referencia para todos los tipos de bosque (Avitabile et al., 2016). La biomasa aérea calculada a partir de ecuaciones alométricas y datos de estructura obtenidos de censos de campo proveen una medida de la masa de los árboles y pueden ser sumados para obtener la biomasa aérea contenida en una parcela. Las ecuaciones alométricas son utilizadas para estimar propiedades que no son fácilmente medibles, como la biomasa aérea o el volumen, a partir de propiedades que son más fácilmente medibles como altura o longitud y el diámetro del tronco, o diámetro normal (DN) a 1.30 m de altura, una medida de la densidad específica de la madera (Chave et al., 2005). Estas ecuaciones se construyen a partir de procedimientos destructivos que consisten en derribar y dividir las plantas, secar y pesar cada componente para determinar su biomasa directamente (Picard et al., 2012). Las características físicas de los árboles pueden variar en respuesta a factores ecológicos y ambientales locales, por lo que es importante considerar ecuaciones alométricas desarrolladas localmente y utilizar datos de estructura obtenidos localmente para estimar la biomasa aérea. Para los bosques tropicales, las ecuaciones alométricas para estimar la biomasa aérea son, en general, una función del DN, la densidad específica de la madera y la altura total del árbol (Chave et al., 2005). Sin embargo, estos atributos, pueden variar entre coberturas forestales en diferentes condiciones ambientales y edades de sucesión (Swenson & Zambrano, 2017). Esta variación puede ser un factor clave para determinar los patrones espaciales de distribución de la biomasa aérea (Svob et al., 2014; Slik et al., 2010).

La información que sirve de insumo para el uso de estas ecuaciones puede obtenerse de inventarios nacionales o censos forestales. En México, la Comisión Nacional Forestal (CONAFOR) ha colectado datos de campo a través de toda la República Mexicana desde 1961 a través del Inventario Nacional Forestal y de Suelos (INFyS). Por lo menos dos inventarios nacionales a gran escala se han llevado a cabo: el primero de 1961 a 1985 y el segundo de 2009 a 2014, los cuales incluyen remediciones entre períodos y algunos inventarios de menor escala en 1991, 1994 y 2000. La magnitud temporal y espacial de este inventario la convierte en un insumo atractivo para monitorear cambios en la vegetación, sin embargo, la adquisición de datos podría no ser igualmente apropiada entre las coberturas forestales del país. El INFyS obtiene información de las alturas, el DN, el número de tallos y la abundancia de todas las especies de plantas leñosas con un DN mayor a 7.5 cm en conglomerados de 4 parcelas de

400 m². Mientras que el umbral de DN puede representar a la mayoría de los individuos en los bosques perennifolios de mayores alturas, y podría excluir una gran cantidad de individuos en bosques más secos como el subcaducifolio y caducifolio, así como en bosques secundarios más jóvenes de todos los tipos de bosques.

1.1.6.2 ESTIMACIÓN DE LA BIOMASA AÉREA POR MEDIO DE PERCEPCIÓN REMOTA

La percepción remota ofrece herramientas capaces de capturar información sobre atributos de la vegetación en áreas grandes, donde no es posible obtener información de campo ya sea por barreras físicas o por limitaciones financieras, temporales o logísticas. Una de las principales ventajas es que los productos y herramientas abarcan áreas extensas y que los métodos para procesarlas son relativamente eficientes, adquiriendo así grandes cantidades de información en períodos cortos de tiempo e incluso periódicamente, lo que permite así la caracterización de cambios a través del tiempo.

La gran gama de sensores y métodos que se han utilizado para caracterizar atributos de la vegetación se puede dividir en sensores pasivos y activos. Los sensores pasivos, o sensores ópticos, capturan información de las longitudes de onda que son reflejadas por los diferentes elementos en el paisaje, y por tanto diferentes coberturas del suelo. Los sensores activos permiten tomar medidas directamente utilizando su propia fuente de energía (radiación electromagnética), llamada pulso, y midiendo el retorno, muchas veces llamado retrodispersión. Estos sensores son capaces de medir distancias de una manera muy precisa. Existen varios estudios que exploran la combinación de sensores y datos auxiliares para la estimación de biomasa aérea en bosques templados o boreales (E.g. Matasci et al., 2018; Pflugmacher et al., 2014) y en bosques tropicales secos (Bispo et al., 2020; Hernández-Stefanoni et al., 2020; Corona-Núñez et al., 2018; Rodríguez-Veiga et al., 2016).

1.1.6.3. ESTIMACIÓN DE BIOMASA AÉREA POR MEDIO DE SENSORES PASIVOS

En la última década, ha habido un incremento en el interés por utilizar el archivo histórico de imágenes Landsat para estimar atributos de la vegetación relacionados con la biomasa aérea (Matasci et al., 2018; Pflugmacher et al., 2014; Cartus et al., 2014) . El archivo histórico de Landsat ofrece una cobertura global de imágenes con resolución espacial de 30 m y una resolución temporal muy alta, tomando imágenes desde 1970 cada 16 días, lo que lo convierte una herramienta útil para la caracterización de cambios en la vegetación. Las imágenes se encuentran disponibles a través del programa Landsat en el U.S. Geological Survey (USGS) de la NASA (National Aeronautics Space Administration).

Uno de los métodos más utilizados para la estimación de biomasa aérea por medio de la estructura del bosque es utilizar las medidas de estructura como un sustituto de la edad, debido a que se relacionan positivamente. Debido a la alta resolución temporal de Landsat, que contiene información de 1972 a 1983 de las misiones Landsat 1 – 3, 1983 a 2013 de Landsat 4 y 5 y de 1999 en adelante para las misiones Landsat 7, es posible determinar cortes en la vegetación por medio de la detección de cambios de un píxel de bosque a un píxel de no bosque. De acuerdo con la magnitud, esta información puede determinarse como un punto de quiebre donde ocurre una pérdida de cobertura. Al restar el año donde ocurre el punto de quiebre más grande en la historia del píxel al año de mapeo, obtenemos una medida de la edad del bosque (o los años sin cambio significativo) (Hermosilla et al., 2015). Por esta razón, la resolución temporal de Landsat es uno de sus atributos más importantes para la estimación de biomasa aérea. Landsat 8 tiene una resolución espectral de 11 bandas (Cuadro 2).

Cuadro 1.2. Relación del nombre y número de banda, resolución espectral y espacial de Landsat Thematic Mapper (TM), Enhanced Thematic Mapper (ETM) y Operational Land Imager (OLI).

	Landsat OLI (8)			Landsat ETM (7)			Landsat TM (4,5)		
Nombre	**Resolución espectral**	**#**	**Resolución espacial (m)**	**Resolución espectral**	**#**	**Resolución espacial (m)**	**Resolución espectral**	**#**	**Resolución espacial (m)**
Violeta	0.433 - 0.453	1	30	-	-	-	-	-	-
Azul	0.450 - 0.515	2	30	0.45 - 0.515	1	30	0.45 - 0.52	1	30
Verde	0.525 - 0.600	3	30	0.525 - 0.605	2	30	0.52 - 0.60	2	30
Rojo	0.630 - 0.680	4	30	0.63 - 0.69	3	30	0.63 - 0.69	3	30
Cercano a Infrarrojo	0.845 - 0.885	5	30	0.775 - 0.90	4	30	0.76 - 0.90	4	30
Infrarrojo de onda corta	1.560 - 1.660	6	30	1.55 - 1.75	5	30	1.55 - 1.75	5	30
Infrarrojo de onda corta 2	2.100 - 2.300	7	30	2.08 - 2.35	7	30	2.08 - 2.35	7	30
Pancromática	0.500 - 0.680	8	15	0.52 - 0.9	8	15	-	-	-
Cirrus	1.360 - 1.390	9	30	-	-	-	-	-	-
Térmica 1	10.6 - 11.2	10	100	10.4 - 12.5	6	60	10.14 - 12.5	6	120
Térmica 2	11.5 - 12.5	11	100	-	-	-	-	-	-

Por otra parte, el satélite Sentinel 2 de la Agencia Espacial Europea (ESA por sus siglas en inglés), tiene un tiempo de revisita de 5 días, por lo que potencialmente puede capturar patrones fenológicos debidos a la estacionalidad. Sus imágenes se encuentran disponibles desde el 2015 y tiene un tiempo de órbita planeada para 7.5 años. Sentinel 2 está cargado con un escáner multiespectral de 13 bandas con diferentes resoluciones. Debido a la alta resolución

(10 m) de sus bandas azul (0.49 µm longitud central), verde (0.56 µm) y roja (0.665 µm), Sentinel 2 tiene potencial para producir estimaciones más precisas al evitar la mezcla de firmas espectrales en un solo píxel. Adicionalmente, Sentinel 2 incorpora borde rojo en tres bandas (0.705, 0.740, 0.783 y 0.865 µm) con resolución espacial de 20 m, el cercano a infrarrojo (0.842 µm) a 10 m, vapor de agua (0.945 µm) a 69 m, infrarrojo de onda corta cirrus (1.375 µm) a 60 m, y dos bandas adicionales de infrarrojo de onda corta (1.610 y 2.190 µm) a 20 m (Figura 1). Las plantas verdes, absorben las longitudes de onda pertenecientes al espectro visible, en particular el rojo y el azul, y reflejan el infrarrojo, por lo que la combinación de la alta resolución de las bandas del espectro visible, la incorporación de las bandas de borde rojo y la resolución temporal de Sentinel 2 lo convierten en una herramienta útil para el mapeo de la vegetación y sus atributos (Saini & Ghosh, 2018).

Otros enfoques para la estimación de biomasa involucran el uso de las propiedades espectrales de la imagen para estimar cambios en la cobertura forestal que pueden estar asociados a disturbios y regeneración (Powell et al., 2010). Uno de los índices más utilizados es el Índice Normalizado de la Diferencia en la Vegetación (NDVI por sus siglas en inglés) que puede ser obtenido por medio una combinación de bandas, e identifica la presencia de vegetación en un determinado píxel. Sin embargo, como todos los sensores pasivos, sólo obtiene la información del estrato más alto de la vegetación (Huete et al., 2014). Por lo tanto, frecuentemente se utilizan en conjunción con sensores activos, que tienen la capacidad de penetrar el dosel y obtener información de los estratos más bajos, para reducir el sesgo y producir estimaciones más precisas (Pflugmacher et al., 2014; Baccini & Asner, 2013; Lu, 2006).

1.1.6.4. ESTIMACIÓN DE BIOMASA POR MEDIO DE SENSORES ACTIVOS

Debido a su capacidad para penetrar el dosel, los sensores activos pueden proveer información precisa de la estructura de la vegetación. El Radar de Apertura Sintética (SAR por sus siglas en inglés) ha sido utilizado para estimar la estructura del bosque por medio de sus bandas P (70 cm λ central), sensible a troncos y estructuras grandes, y L (23 cm), sensible a los troncos y ramas. La retrodispersión de onda más corta, como las bandas X y C (3 cm y 6 cm respectivamente), también han sido utilizadas para estimar la estructura del bosque, sin embargo, son sensibles a las estructuras más pequeñas como hojas y tallos pequeños, por lo que la información de las bandas P y L resultan de mayor utilidad para estimar biomasa aérea.

Sin embargo, las estimaciones de biomasa aérea por medio de retrodispersión de los sensores de radar se saturan en bosques con biomasa aérea superior a los 150 Mg ha^{-1} y la señal es afectada por variaciones topográficas y en el contenido de humedad del suelo y de la vegetación (Cartus et al., 2014), por lo que no es apropiado para estimar la distribución en todos los tipos de bosque.

Por otro lado, LiDAR (Light Detection and Ranging) puede obtener información tridimensional de la estructura de la vegetación, superando así los umbrales de saturación. Las métricas de altura y cobertura de LiDAR han sido utilizadas para estimar biomasa aérea en bosques tropicales de la Península de Yucatán con ~80% de la variación explicada (Hernández-Stefanoni et al., 2014), un incremento del alrededor del 30% en comparación con estimaciones hechas con ALOS PALSAR. Adicionalmente, estas estimaciones muestran una sobreestimación de la biomasa aérea en bosques de la Península de Yucatán y las variables derivadas de ALOS PALSAR no fueron identificadas como predictores importantes (Cartus et al., 2014). Otra posibilidad involucra el uso de parcelas de cortes de datos LiDAR como sustitutos de nuevas parcelas de campo para incrementar el tamaño de muestra sin incrementar el costo de los censos de campo (Matasci et al., 2018). En general, este procedimiento, llamado escalamiento, consiste en ajustar un modelo de datos de campo de referencia a métricas de altura y cobertura de LiDAR. Después, aplicar el modelo a la extensión de los datos LiDAR y así aumentar la cantidad de parcelas de referencia (Matasci et al., 2018). Sin embargo, el uso de LiDAR para realizar el escalamiento hacia estimaciones regionales, requiere de protocolos de validación que permitan cuantificar el efecto de la autocorrelación espacial que introducen los datos LiDAR, al tener coberturas únicamente en áreas localizadas (Ploton et al., 2020; Yanai et al., 2020; Duncanson et al., 2019).

Recientemente se ha resaltado la importancia de contar con protocolos de validación exhaustivos, que exploren la propagación de error que es introducido en cada etapa del proceso de escalamiento, especialmente para uso en estrategias de reporte y verificación de emisiones de gases de efecto invernadero y para programas como REDD +, cuyo objetivo es reducir las emisiones por deforestación y degradación en países tropicales como México (REDD+) (Yanai et al., 2020; Duncanson et al., 2018).

1.2 JUSTIFICACIÓN

En el año de 1992 el gobierno de México firmó su compromiso a reducir las emisiones por deforestación y degradación ante la Convención Marco de las Naciones Unidas ante el Cambio Climático (CMNUCC). A partir de entonces México se ha enfocado en desarrollar estrategias que favorezcan las acciones de mitigación y reducción de emisiones de gases de efecto invernadero, en particular del CO_2. Entre los logros del país, presentados en el 2015 como parte del acuerdo de París, está la estimación de la Contribución Determinada a Nivel Nacional (NDC), en la que se establecen metas puntuales de reducción de emisiones a nivel nacional y que fueron incorporadas a la Ley General de Cambio Climático (LGCC).

Dentro de las premisas que conforman la NDC y la LGCC se destaca que el sector forestal es clave para la mitigación de los efectos adversos del cambio climático, sin embargo, son necesarias las estimaciones puntuales tanto de los almacenes de biomasa aérea, que son los más susceptibles a ser emitidos por deforestación y degradación (Houghton, 2005), como del potencial de mitigación que ofrecen los bosques en regeneración.

Hasta el momento, existen vacíos de información importantes con relación a la distribución espacial de la edad y de la biomasa aérea de los bosques tropicales, y en particular de los bosques tropicales secos de la Península de Yucatán. Existen estimaciones espacialmente explícitas de la edad reportadas en trabajos anteriores (Hansen et al., 2013), sin embargo, éstas se derivan de información global y no reportan pasos metodológicos específicos ni estimaciones de incertidumbre asociada. Por otra parte, las estimaciones de biomasa aérea existentes para Yucatán y México (Hernández-Stefanoni et al., 2020; Rodríguez-Veiga et al., 2016; Cartus et al., 2014) tienden a sobreestimar el contenido de biomasa en bosques jóvenes. De esta manera, el segundo capítulo de este trabajo pretende llenar estos vacíos de información y reducir la sobreestimación de la biomasa aérea de bosques jóvenes de la Península de Yucatán mediante la inclusión de información espacialmente explícita de la edad del bosque.

Por otra parte, existe la necesidad de mejorar las estimaciones espacialmente explícitas de la biomasa aérea de los bosques tropicales secos y de propagar las incertidumbres asociadas a cada paso de la estimación. Esta información debe reportarse explícitamente (Yanai et al., 2020). El Capítulo 3 de este trabajo pretende estimar la biomasa aérea mediante la combinación de sensores pasivos y activos, con el fin de mejorar las estimaciones de biomasa aérea para bosques tropicales secos de la Península de Yucatán y de propagar las incertidumbres asociadas a cada paso de la estimación de manera espacialmente explícita, llenando un vacío de información importante para futuras estimaciones de los acervos de carbono en la biomasa aérea de los bosques secos tropicales.

Esta información puede servir de guía para la elaboración de protocolos de estimación que permitan mejorar las estimaciones de biomasa aérea, reducir la sobreestimación de bosques jóvenes y reportar las incertidumbres asociadas de manera explícita, que deben ser reportados a nivel nacional. Igualmente, esta información puede ser de utilidad para la elaboración de los inventarios de gases de efecto invernadero y los acervos de carbono contenidos en la biomasa aérea de los bosques tropicales secos de la Península de Yucatán.

1.3 PREGUNTAS DE INVESTIGACIÓN

1. ¿Cómo varía espacial y temporalmente la extensión de pérdida de vegetación en los tres tipos de bosques secos más extensos de la Península de Yucatán?
2. ¿Cómo varía la precisión de las estimaciones de pérdida de cobertura forestal obtenidas del análisis de series de tiempo de NDVI en los tres tipos de bosques secos de mayor extensión de la Península de Yucatán?
3. ¿Se puede reducir la sobreestimación de las estimaciones de biomasa aérea de los bosques jóvenes de la Península de Yucatán por medio de la incorporación de información de la edad del bosque medida por cambios en la cobertura vegetal de series de tiempo de Landsat?
4. ¿Qué tanto se puede incrementar la precisión en la estimación espacial de la biomasa aérea de un bosque tropical subcaducifolio por medio del escalamiento de datos de campo a información de reflectancia y textura de imágenes obtenidas de sensores pasivos y activos?
5. ¿Cuál es la magnitud de la diferencia en la precisión entre utilizar una combinación de texturas y reflectancia de un sensor pasivo y un sensor activo para estimar biomasa aérea en un bosque tropical subcaducifolio y realizar las estimaciones de cada sensor por separado?
6. ¿Cómo varía espacialmente la incertidumbre en las estimaciones de la biomasa aérea de un bosque tropical subcaducifolio?
7. ¿Cómo varía la distribución de la biomasa aérea de un bosque tropical subcaducifolio de la Península de Yucatán entre diferentes tipos de manejo forestal (áreas con aptitud para producción forestal, restauración o conservación)?

1.4 HIPÓTESIS

1. La distribución espacial de la pérdida de vegetación está asociada fuertemente a las condiciones ambientales del bosque y el uso de suelo previo. En bosques con condiciones ambientales de mayor sequía, donde se llevan a cabo actividades como la roza-tumba-quema, la reducción del área de bosque es mayor, comparado con ambientes más húmedos y/o de manejo comunitario de menor impacto, donde la pérdida de cobertura forestal es menor. Esperamos encontrar mayores áreas de cambio en los bosques (tropical caducifolio y subcaducifolio) donde se practica la agricultura de roza tuba y quema, que en (bosque tropical subperennifolio) donde se lleva a cabo un manejo comunitario de menor impacto como la extracción selectiva.

2. La precisión en la estimación de la pérdida del área de bosque es afectada por procesos como la regeneración después de un disturbio y la estacionalidad. Debido a que el modelo harmónico de BFast puede tomar en cuenta la estacionalidad, puede diferenciar la senescencia foliar de la estación de sequía de una pérdida de cobertura, por lo que podemos obtener estimaciones precisas de la pérdida de cobertura en los tres tipos de bosque.

3. Debido a que la edad del bosque refleja los patrones de acumulación de biomasa a lo largo del tiempo, puede ayudar a reducir la sobreestimación de la biomasa de bosques en etapas tempranas de regeneración, donde comúnmente es sobreestimada. Se espera que las estimaciones de biomasa aérea por medio de la edad estimada a partir del último evento de pérdida de cobertura forestal serán menores que las estimadas a partir de otros métodos de percepción remota, y más similares a los datos de referencia de campo.

4. El tipo de sensor utilizado tendrá un efecto en la estimación de biomasa aérea: A) Debido a la alta resolución (10 m) de las imágenes Sentinel 2 A y a que la reflectancia de las imágenes pasivas, particularmente las bandas que abarcan del espectro rojo al

infrarrojo, ha sido previamente relacionada con la estructura de la vegetación, será posible estimar la biomasa aérea del bosque tropical subcaducifolio utilizando Random Forests y reflectancia de imágenes Sentinel 2 A de manera precisa. B) Asimismo, debido a que los sensores activos tienen la capacidad de penetrar nubes y humo, y que pueden registrar de manera precisa la estructura del dosel, será posible estimar de manera precisa la biomasa aérea de un bosque tropical subcaducifolio utilizando Random Forests y la retrodispersión de ALOS PALSAR. C) Sin embargo, debido a la mayor resolución espacial de las imágenes de Sentinel 2A (10 vs 25 m) y a la saturación de ALOS-PALSAR en ambientes con biomasa superior a las 150 Mg ha –1, Sentinel producirá estimaciones más precisas de la biomasa aérea en un bosque tropical subcaducifolio.

5. Debido a que la textura en las imágenes tiene la capacidad de captar la variación espacial de la reflectancia y/o la retrodispersión, y que ésta refleja la variación entre los elementos del paisaje, el incorporar medidas de textura en la imagen hará posible detectar la estructura del dosel de manera precisa y permitirá incrementar la precisión en las estimaciones de biomasa aérea en un bosque tropical subcaducifolio.

6. La combinación de ambos sensores permitirá compensar las limitaciones individuales de cada uno, incorporando información de la estructura, sin ser afectada por nubes y humo mediante ALOS PALSAR y a la resolución espacial de Sentinel 2A (10 m). Por esta razón, la combinación de los dos sensores producirá estimaciones de biomasa aérea de un bosque tropical subcaducifolio con mayor precisión y menor error.

1.5 OBJETIVO GENERAL

2. Estimar la distribución espacial de la edad sucesional del bosque por medio del año de pérdida de cobertura forestal y de la biomasa aérea de los tres tipos de bosque más extensos de la Península de Yucatán y comparar la precisión de las estimaciones con trabajos previos realizados en los sitios de estudio.

3. Estimar la distribución espacial de la biomasa aérea y su incertidumbre por medio de sensores pasivos y activos, y comparar los valores obtenidos entre diferentes categorías de manejo forestal en un bosque tropical subcaducifolio de la Península de Yucatán.

1.6 OBJETIVOS ESPECÍFICOS

1. Estimar el área de pérdida de vegetación para cada año desde el año 2000 al 2020 utilizando de series de tiempo de NDVI y el algoritmo de detección de cambios BFAST en los tres tipos de vegetación forestal más extensos de la Península de Yucatán.
2. Estimar la biomasa aérea de los bosques jóvenes a partir de la relación entre la edad sucesional del bosque y la biomasa aérea obtenida de datos de cronosecuencia de un trabajo previo, en los tres tipos de vegetación forestal más extensos de la Península de Yucatán, y comparar la precisión de las estimaciones obtenidas con las de otros trabajos realizados por medio de percepción remota y datos de referencia de campo.
3. Estimar la biomasa aérea para la extensión del censo de LiDAR utilizando la altura total del dosel calculada de LiDAR e información de campo.
4. Estimar la biomasa aérea en la escala regional utilizando la reflectancia y texturas de imágenes Sentinel 2A y ALOS PALSAR, por separado y en combinación, y la biomasa calculada por medio de LiDAR.
5. Obtener la distribución de frecuencias de los valores de biomasa aérea para áreas con diferentes categorías de manejo (áreas dedicadas a la conservación, áreas con aptitud para la producción o para la restauración).

1.7 ESTRATEGIA EXPERIMENTAL

El segundo capítulo de este trabajo se centra en la aplicación del algoritmo de detección de cambios Breaks For Additive and Seasonal Trends (BFAST) a una serie de tiempo de imágenes Landsat que abarca el período 1985 a 2020 para obtener información precisa de la edad de los bosques jóvenes de selva baja caducifolia, selva mediana subcaducifolia y selva mediana subperennifolia de la Península de Yucatán. Este algoritmo se seleccionó debido a que es capaz de utilizar varias imágenes por año y discernir las tendencias de cambio de cobertura de las tendencias estacionales de pérdida de follaje características de los bosques tropicales. Posteriormente, se utilizó la relación entre la biomasa aérea y la edad, obtenida por medio de cronosecuencias previamente establecidas en la selva subcaducifolia y la selva subperennifolia, para obtener modelos de biomasa y edad que permitan estimar espacialmente la biomasa aérea de los bosques tropicales secos.

El tercer capítulo de este trabajo se centra en la obtención de mapas de biomasa aérea de una selva mediana subcaducifolia de la Península de Yucatán mediante el escalamiento de datos de biomasa obtenidos en parcelas de campo a escala de paisaje. El primer paso es el escalamiento de datos de campo a datos LiDAR mediante un modelo linear de efectos fijos. El segundo paso consiste en el escalamiento de datos LiDAR a escala de paisaje utilizando una combinación de datos de sensores pasivos (imágenes Sentinel 2 A) y activos (ALOS-PALSAR) por medio de Random Forest, un algoritmo de Machine Learning que permite obtener estimaciones mediante árboles de decisión.

CAPÍTULO II

2. MAPPING THE SPATIAL DISTRIBUTION OF STAND AGE AND ABOVEGROUND BIOMASS FROM LANDSAT TIME SERIES ANALYSES OF FOREST COVER LOSS IN TROPICAL DRY FORESTS

Artículo publicado en Remote Sensing in Ecology and Conservation DOI:10.1002/rse2.247

ABSTRACT

Spatial information on the timing of forest cover loss is important to identify and map stand age, which is a key factor driving the recovery of carbon pools and can also be used to estimate aboveground biomass (AGB) based on its relationship with stand age. Here, we estimated the spatial distribution of stand age and AGB of young forest (< 20 years) in three types of tropical dry forest in the Yucatan peninsula using Landsat NDVI (normalized difference vegetation index) time-series from 2000 to 2020. We estimated AGB based on chronosequence data and compared these results to reference field data and estimations obtained from remote-sensing studies. The overall and user accuracy of the age map was high (95.7 - 99.9% and 87.35 - 98.5% respectively). However, lower producer accuracy values (from 31.2 to 67.2%) suggest an underestimation of the extension of young forests. We found a greater extent of young forests in the semi-deciduous and deciduous forests compared to the semi-evergreen ones. Mean AGB estimated from stand age (53.1 Mg ha $^{-1}$) was lower than that estimated from remote-sensing studies (67.5 to 95.2 Mg ha $^{-1}$). These results indicate that spatial information of forest age can be accurately assessed from Landsat time series, and that the combination of stand age with chronosequence data can reduce the overestimation of AGB of recovering forests commonly found in remotely sensed data.

2.1. INTRODUCTION

Habitat loss, and particularly deforestation, is one of the most important environmental problems in the anthropocene. Deforestation alters biogeochemical cycles, including the carbon cycle, thereby compromising the potential for carbon sequestration and climate change mitigation (Portillo-Quintero et al., 2015). It also leads to the loss of biological diversity (Malhi et al., 2008), which is crucial for the resilience of forest landscapes in the age of global change (Thompson et al., 2009). The loss of forest cover is most extensive in tropical areas due to the conversion of forest to agriculture or urban settlements (Keenan et al., 2015), especially in tropical dry forests (Allen et al., 2017; Bhaskar et al., 2018), which are responsible for approximately half of the carbon storage capacity in tropical forests worldwide (Keith et al., 2009). However, forests can regenerate after a disturbance event and, depending on the intensity and type of disturbance, attributes such as species richness (Norden et al., 2009) and aboveground biomass (AGB) can recover and approach pre-disturbance conditions within a few decades (Chazdon, 2008; Poorter et al., 2016). Other attributes such as species composition recover at much slower rates or might never reach primary forest levels (R. Chazdon, 2008; Rozendaal et al., 2017). Therefore, the time since the last disturbance (year of latest forest cover loss) can be related to stand age, and since AGB is strongly related to successional age (Read & Lawrence, 2003), it is possible to use this information to estimate the spatial distribution of AGB in recovering forests.

The spatial distribution of AGB has been estimated at multiple scales using a wide variety of remotely sensed products and methods (Avitabile et al., 2016; Saatchi et al., 2011; Rodriguez-Veiga et al., 2016; Hernández-Stefanoni et al., 2020). However, there is a clear tendency for remote sensing methods not only to underestimate AGB in mature forest due to a saturation of remotely sensed data, but also to overestimate the AGB in young forests (Rodriguez-Veiga et al., 2016; Hernández-Stefanoni et al., 2020). Forest age is a key factor driving the recovery of carbon pools, and thus, carbon balance in tropical forests (Coursolle et al., 2012; Gao et al., 2016). Therefore, the estimation of the spatial distribution of young forest could accurately reflect the changes in vegetation attributes such as AGB that take place during early succession. In addition, this information could help to locate recovering forests, which have a large carbon sequestration potential (Poorter et al., 2016).

The Yucatan peninsula holds the second largest extent of continuous forested land in Latin America after the Amazon. The forests here are characterized by presenting a gradient of forest cover types which transition from deciduous tropical dry forests in the drier northern part of the Peninsula to semi deciduous and semi-evergreen forests in the more humid south-east (Dupuy et al., 2015). Forests in the Yucatan Peninsula have had a long and unique history of land cover changes which varies spatially leading to a mosaic of patches of forest in different stages of recovery (stand age), and other land uses. Additionally, there is a high incidence of natural disturbances such as hurricanes and forest fires, which are also important drivers of forest dynamics (Mascorro et al., 2016) . Obtaining spatially explicit information of the year of the most recent forest cover loss in these ecosystems could provide a proxy for stand age. In particular for disturbances that are patchy and generally of small spatial and/or temporal scale, such as those associated with swidden agriculture, extraction of forest products, hurricanes and fires, which characterize most of the forests of the Yucatán Peninsula. This could help to identify areas of young recovering forests, thus aid conservation efforts and landscape-level management of these forests. However, obtaining exact information on the spatial distribution of stand age can be a challenging task especially for tropical forests, where field-based information of stand age is often obtained from interviews to local informants, and it is often unavailable for large extents.

Remote sensing offers methods for obtaining extensive historical data that have been used to overcome this challenge. The Landsat archive provides a global archive of 30 m resolution imagery from March 1984 to date, with a temporal resolution of 16 days (USGS 2020). A number of land cover change detection algorithms have been developed, taking advantage of the temporal extent of the Landsat Archive, to locate areas where a loss of forest cover has occurred by constructing time series of images and identifying changes in forest cover from time x to times x + 1, x + 2, and so on. Changes in forest cover are usually tracked by a measure of ‘greenness’, identified by vegetation indices, in ‘time x’ to sudden decreases or absences of ‘greenness’ in times x + 1, x + 2, and so on for the same location. However, in seasonally dry tropical ecosystems differentiating these changes can be challenging due to the confounding effect of seasonal fluctuations in ‘greenness’ associated with leaf abscission during the dry season.

Two common change detection algorithms are the Vegetation Change Tracker (VCT) (Huang et al., 2010), developed by NASA and the LandTrendr (Landsat-based Detection of Trends in Disturbance and Recovery) (Powell et al., 2010) developed by Oregon State University. These algorithms identify changes in land cover across large areas. However, these algorithms fail to capture intra-annual variability, an important characteristic in seasonal environments such as tropical dry forests, as they accept only one image per year. Therefore, even if all images are acquired at the same time of the year, inter annual variation in leaf phenology can bias estimates of land cover change in seasonal forests. Moreover, global estimates of forest cover loss such as that of Hansen et al., (2011) often rely on generic definitions of forest without accounting for differences in forest types and plantations, which can lead to systematic bias due to differences in structure and seasonal patterns. The Breaks for Additive Seasonal Trend (BFAST) algorithm, is a change detection algorithm able to process dense time series constructed with diverse vegetation indices using all available imagery within a year, thus enabling the accurate characterization of seasonal changes (Verbesselt et al., 2010). The algorithm fits a harmonic model with a trend and a seasonal component for each of the pixels within the images in the time series, and then flags the pixels whose estimated values deviate from the model predictions. This method shows great potential for producing highly accurate spatial estimations of forest loss, and thus also of forest age, in highly seasonal tropical areas where small-scale swidden agricultural practices are common (Smith et al., 2019).

The objectives of this research were twofold. First, we aimed to produce accurate estimations of the year of the last forest cover loss from 2000 to 2020 as a measure of stand age in young forest stands (<20 year old) in three tropical dry forest landscapes of the Yucatan Peninsula. Second, to estimate AGB in these landscapes based on stand age and chronosequence data (relating both variables) and to compare these estimations with those of previous remote sensing studies. We estimated land cover changes in different types of tropical dry forest with slightly different land-use histories using the BFAST algorithm (Verbesselt et al., 2010). Swidden agriculture is the predominant land use in the semi-deciduous and deciduous forests, whereas cattle ranches and selective logging are more common in the semi-evergreen forest. Therefore, we expected the timing and extension of young forest to differ across sites with a greater extension of young stands in the drier forest sites, due to the cyclic nature of swidden agriculture, which involves a relatively short (< 20 years) fallow period. We also test whether information on the spatial distribution of forest age could reduce the overestimation of AGB in young forest that has previously been found in different remote-sensing studies (Cartus et al., 2014; Rodríguez-Veiga et al., 2016; Hernandez-Stefanoni et al., 2020) by capturing forest recovery time. We expected a reduction in the overestimation of AGB in young forest stands (< 20 years old) based on BFAST-derived stand age, compared to direct estimates from satellite imagery in previous studies.

2.2. METHODS

2.2.1 STUDY AREA

Three 3,600 km^2 square areas were selected in the Yucatan Peninsula (Figure 1). The first area is located in ‘El Palmar’ (EP) State Reserve in the NW part of the peninsula in the State of Yucatán (NW -90.2532, 21.05901; SW -90.26236, 20.51653; NE -89.68876, 20.50651; SE -89.67691, 21.04886). This is the driest site with mean annual precipitation ranging from 500 to 700 mm per year. The predominant vegetation type is deciduous tropical dry forest (> 80% of trees shed their leaves during the dry season) characterized by small stature (8 -10 m) tree species (García et al., 2011; Flores Espejel 1994). The development of henequén (*Agave fourcroydes*) plantations in the area and their subsequent abandonment and the practice of traditional swidden agriculture has resulted in a mosaic of forest patches of different successional age (Wyman et al., 2007). The second site ‘KK’ is located in the middle portion of the Peninsula and it is named after a private reserve ‘Kaxil Kiuic Biocultural Reserve’ (-NW 89.84347, 20.16099; SW -89.84347, 19.61903; NE -89.27052, 20.16101; SE -89.27053,19.61904).

The dominant vegetation type is medium size (10 - 15 m) semi deciduous tropical dry forest (50 – 75% of trees shed their leaves during the dry season). Mean annual precipitation ranges from 900 to 1100 mm. The most common land use in this area is swidden agriculture. Precipitation at these two sites is highly seasonal with a long dry season typically from November to April and a wet season from May to October when most of the precipitation occurs. The third site is ‘FCP’ located in the middle portion of the state of Quintana Roo at (NW -88.60036, 19.53102; SW -88.60036, 18.98904; NE -88.02964, 19.53102; SE -88.02964, 18.98903). The dominant vegetation corresponds to semi-evergreen tropical forest, with taller trees (15 – 25 m) and a lower proportion (< 25%) of deciduous tree species. This area is also characterized by the presence of patches of low seasonally flooded forest. Mean annual precipitation ranges from 1100 to 1300 mm per year, making this the most humid of our field sites (Figure 2.1). Land use in this site includes selective extraction of commercially important woody species, pastures for cattle (Armenta-Montero et al., 2020), and small-scale swidden agriculture (Ellis et al., 2017b, Mascorro et al., 2016).

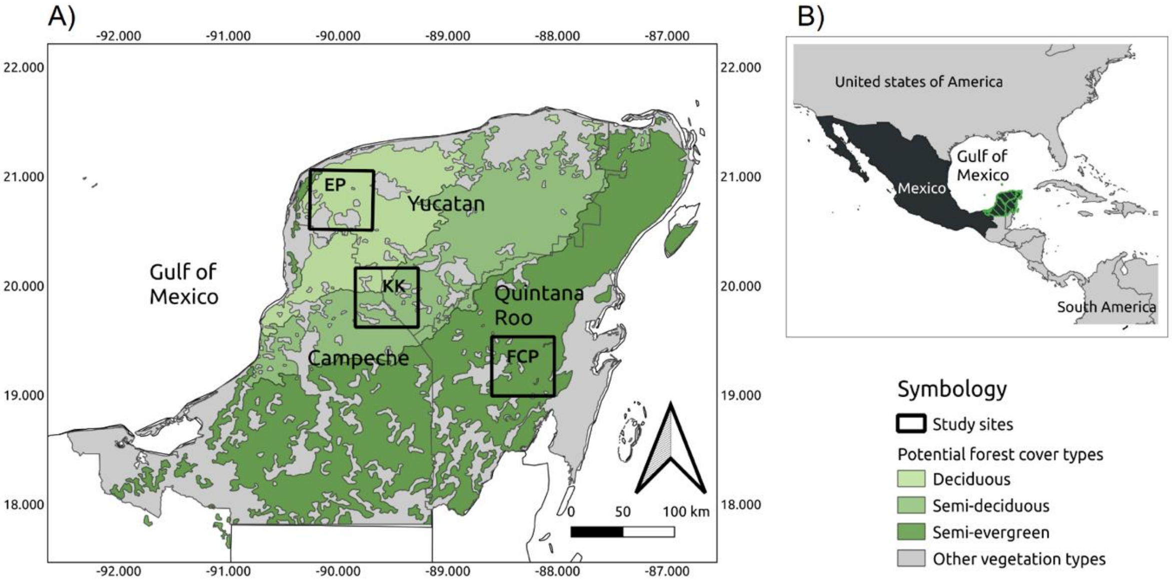

Figure 2.1. A) Location of three study sites in the Yucatan Peninsula: EP: El Palmar; KK: Kaxil Kiuic; FCP: Felipe Carrillo Puerto. Sites are located in the three most widespread forest cover types of the Yucatan Peninsula. B) Location of the Yucatan Peninsula.

2.2.2 SATELLITE IMAGERY ACQUISITION AND PREPROCESSING

Multispectral Landsat imagery from January 1985 to August 2020 in Landsat Collection 1, from sensors Landsat TM, ETM+ and OLI, were obtained using the NASA Earth Explorer search engine. The search was filtered for daytime images with less than 70% cloud cover. All surface reflectance bands, Normalized Difference Vegetation Index (NDVI), and ‘pixel qa’ (quality assessment) layers were selected. We download 552 images for the semi-deciduous and deciduous sites (path 20, row 46) and 654 for our semi-evergreen site (path 20, row 45).

Landsat scenes were cropped to the extent of our study area and preprocessed in R (package ‘bfastSpatial’) (Verbesselt et al., 2010; Verbesselt et al., 2012). Then, images were filtered using Landsat ‘pixel qa’ (pixel quality assessment) layer to produce images with cloud cover under 70% for our study areas. Finally, the filtered images were stacked using the ‘timestack’ function, which constructs a raster of stacked, filtered NDVI scenes organized by date. This stack is the main input for the ‘bfmSpatial’, the main function which performs the time-series analysis. For detailed code and other parameters see Supplementary material 1.

NDVI was used due to its ability to differentiate photosynthetically active vegetation from other elements in the landscape by identifying the presence of chlorophyll A. Therefore, this index, which is obtained from the ratio between the sum of and the difference between red and near infrared bands, is able to identify pixels with active vegetation. Other advantages of the NDVI are its efficiency in solving some limitations of using individual bands such as shadowing and topographic effects.

2.2.3. ALGORITHM IMPLEMENTATION: ITERATIVE MONITORING OF FOREST COVER LOSS

Breaks for Additive Seasonal Trends (BFAST) algorithm was applied using the ‘bfmSpatial’ function from ‘bfastSpatial’ package in R (Verbesselt et al., 2010; Verbesselt et al., 2012). The algorithm uses every pixel with cloud free observations throughout all scenes in a time series and fits a regression model with a seasonal and a trend component (Verbesselt et al., 2010). This feature enhances the robustness of the time series and reflects seasonal systems in a more accurate way (Verbesselt et al., 2010). A first order-harmonic model was used for a better reflection of the trajectory of a pixel throughout a time series in a highly seasonal system where changes in precipitation and phenology are a normal component of the system’s functionality (Devries et al., 2015).

An ordinary least squares (OLS) residual based moving sum (MOSUM) test, was selected to test whether the image pixels can be flagged for breakpoints. When the test indicated a significant deviation of observations from the model predictions ($p < 0:05$), the breakpoints were flagged, producing a layer with breakpoints, or pixels containing the date where the change occurred (Verbesselt et al., 2010). The algorithm was applied in an iterative way following Devries et al., (2015) by selecting a short monitoring period (1 year) using each year as the monitoring start year (start = 2000, 2001, and so on) and its subsequent year (end = 2001, 2002, and so on) as the end of the monitoring period. Due to restrictions in the availability of Landsat imagery in the early dates of Landsat archive this algorithm also used all historical imagery available from 1985 to the ‘start’ date to calibrate the model (history = “all”).

The ‘bfmSpatial’ function produces three to six layers of information from the timestack. For a detailed description, see Verbesselt et al., (2010). We used the first layer ‘breakpoints’ (which contains information from potential changes derived from all pixels flagged where the algorithm found significant deviations from the model fit within the monitoring period) and the second layer ‘magnitude’ (the intensity of change found relative to the MOSUM model fit) to produce a new layer containing the magnitudes in all the pixels where a breakpoint occurred. With this approach, we ensure that all data from previous years are used in order to track small-scale changes and that more than one breakpoint can be identified in any given pixel, so we were able to detect changes that took place in the same pixel in each year throughout the length of the time series.

2.2.4. MAGNITUDE THRESHOLD SELECTION

Negative magnitudes have been found to be related to a reduction in tree cover in previous analyses using BFAST (Verbesselt et al., 2012; Devries et al., 2015). We used binomial-logistic regression between deforested sites (1) and no deforestation sites (0) for selecting a forest cover loss threshold following Devries et al., (2015). We used 440 points placed systematically within confirmed forest cover loss and no change locations to obtain the magnitude value with a 50% probability to result from forest cover loss. A dataset with the selection of confirmed forest loss pixels was obtained using the locations where magnitudes < 0 were obtained from the BFAST algorithm, and confirmed deforestation was identified by visual interpretation in QGIS 3 and Google Earth Pro. This analysis was carried out by the ‘glm’ function (family = ‘binomial’) in R (R Development Core Team, 2019).

2.2.5. PRODUCTION OF FOREST-COVER LOSS MAP AND VALIDATION

For each year, a raster clumping analysis was used in order to filter single-pixel changes, which are likely to derive from noise in the time series (Devries et al., 2015; Verbesselt et al., 2012). We selected a minimum mapping unit of 0.5 ha as it is the smallest extension commonly used for swidden agriculture in the area (Mascorro et al., 2016; Garcia-Frapolli et al., 2007) for which images were clustered using ‘Rook’s case adjacency’ to join clusters of pixels with a minimum extension of 0.5 ha (‘areasieve’ in R).

All images were overlayed starting from the most recent year (2020) to the oldest year (2000) using ‘r.patch’ function in QGIS (GRASS GIS 7.2) to obtain a single raster containing all the years of possible deforestation. This method was selected to show the last forest-cover loss estimated in all pixels in our study area, which was assumed to be the year 0, when vegetation regrowth started. Forest age was calculated as the time since the last forest-cover loss event. Land use changes from forest to agriculture or urban areas were not considered in this study, since they imply more permanent changes that do not affect our estimates of stand age in young (< 20 year old) forests. These areas were masked using a land cover map available for each site (Hernandez-Stefanoni et al., 2020). Total area was calculated as the sum of the area occupied by pixels flagged as forest cover loss in all sites.

A limitation on the validation of cover-change maps is the low availability of reference imagery, an issue that is most accentuated in the tropics where cloud cover persists for large parts of the year (Asner et al., 2001). For this reason, two points in the time series were selected according to the availability of reference imagery. Reference datasets are comprised of GeoEye historical imagery (0.5 m resolution) for years 2008 through 2015; RapidEye imagery (5 m) available for the year 2012; and Landsat Tree Cover Product (30 m) (Sexton et al., 2016) for the years 2010 and 2015. Previous work has indicated that the BFAST algorithm identified 81% of the area of forest cover loss with a maximum difference of 18 months in tropical dry forests of the Yucatan peninsula (Smith et al., 2019). Therefore, in this study we considered 1.5 years as a maximum temporal lag between observed and estimated change.

In each validation year, the proportion of area of forest cover loss and no change classes was calculated. We selected 500 samples using Cochran's sample size formula (Cochran 1963) with a stratified sampling design (Olofsson et al., 2013; 2014). Samples were allocated designating a minimum of 100 samples for the smallest class size (forest cover loss) and 400 in the no change class. In this process, each validation unit (sample) corresponds to a Landsat pixel. Each pixel in the validation dataset was located in the reference data set and examined in the same year, before and after the suspected event. We considered a change event as confirmed wherever forest cover was present in the year before and absent during the estimated year of change. This event change is a result of removal of forest cover and the percentage of tree cover, derived from Landsat Tree Cover product, below < 10% as a deforestation threshold (FAO 2020), as opposed to no change when the categories remained the same or tree cover surpassed 10 %. Masks for the end of the monitoring period were derived from Landsat Tree Cover product using R.

In order to assess the accuracy of the changes identified by the BFAST algorithm we constructed a 'confusion matrix' (Congalton 1991) and calculated three measures of accuracy using proportions of areas of change vs. no change rather than pixel counts (Card, 1982) as suggested in Olofsson et al., 2013. Overall accuracy, which is derived from the ratio of the correctly identified forest cover loss area by the total area within the matrix. Producer's accuracy, the probability of a pixel being correctly classified, was estimated as the proportion of correctly classified area within a category divided by the total area in that category based on reference data. Finally, the User accuracy, the probability that a pixel within a class represents that category, was estimated as the total of correctly classified proportion in a category divided by the total area classified in that same category. The accuracies adjusted by area were calculated according to the formulas provided by Olofsson et al., (2014). Per year, variations in the number of validation sites are due to constraints in the availability of GeoEye 0.5 m resolution imagery for some regions, locations for validation points are shown in Supplementary material 2. Following Olofsson et al., (2013), adjusted areas of forest change and 95 % confidence intervals were calculated for each validation year.

2.2.6. ABOVEGROUND BIOMASS ESTIMATION AND COMPARISON WITH OTHER STUDIES

Chronosequence data for 276 plots in the semi-deciduous forest (Hernandez-Stefanoni et al., 2011) and 86 plots in the semi-evergreen forest (Miranda-Plaza et al., 2014) were used to estimate AGB of young forest in this study. These chronosequence data consist of plots of different ages located in the study area. The sampling design in both surveys was stratified to cover the whole range of forest ages over a period of 80 and 100 years in semi-deciduous and semi-evergreen forests correspondingly. In both vegetation types, the sampling units consisted of 200 m^2 circular plots, where all individuals were identified to species level, and height and DBH (diameter at breast height - 1.3 m) were recorded. Stand age for every plot was obtained by interviewing local old landowners. More details of sampling and plot designs are in Hernandez-Stefanoni et al., (2011) and Miranda-Plaza et al., (2014). We calculated AGB in both datasets by using the pan-tropical allometric equation of Chave et al., (2005) for trees whose DBH exceeded 10 cm. Meanwhile, for trees with DBH lesser than 10 cm we used two allometric equations, one developed in the semi-deciduous forest near the KK area and the other in the semi-evergreen forest near the FCP site by Ramirez et al., (2016) and Guyot et al., (2015) respectively. The three equations consider wood density values for the different species. These wood density values were obtained from Hernandez-Stefanoni et al, (2020).

Biomass is affected by tree growth, recruitment and mortality processes during succession. However, models to predict AGB changes over time can be obtained from chronosequence data (Chazdon et al 2006). Therefore, we fitted AGB vs stand age functions using regression analysis. We created two models, one for the semi-deciduous forests, (1) and the other for the semi-evergreen forests (2), the graphs are shown in Supplementary material 3.

$$logAGB_{semi-deciduous} = 2.7 + 0.61 * logAGE \quad (1)$$

$$logAGB_{semi-evergreen} = 2.4 + 0.78 * logAGE$$

(2)

Subsequently, these two models were used to estimate the spatial distribution of AGB of young forest (1 to 20 year old) in the study area using the forest age maps obtained previously. The first model was applied to the deciduous and semi deciduous forest, while the second model was applied in the semi-evergreen forest. The AGB map was produced by applying the AGB vs age functions obtained previously in R (Supplementary material 4).

Previous studies have indicated that BFAST algorithm is able to distinguish forest cover loss with a maximum difference of 18 months between actual and estimated time of change in tropical dry forests of the Yucatan peninsula (Smith et al., 2019). To account for errors derived from temporal lags between observed and estimated forest cover change, we produced forest AGB maps accounting for a temporal lag of 1.5 years, and calculated the differences between the original map and that with the temporal lag as a measure of error.

Finally, the mapped AGB values of young forest in this study were compared to previous maps of AGB in the same area (Cartus et al., 2014; Rodriguez-Veiga et al., 2016; Hernandez-Stefanoni et al., 2020) and reference field data (24 field plots with AGB < 50 Mg ha -1 from the National Forest Inventory of the young forest in the studied area). We compared the estimated biomass values using mean AGB values and 95% confidence intervals in R (R Development Core Team, 2015).

2.3. RESULTS

2.3.1. MAGNITUDE OF THRESHOLD FOR ESTIMATING FOREST COVER LOSS

Binomial-logistic regression between sites of confirmed forest loss (deforestation = 1) and forest permanence (no change = 0) sites showed that a pixel with a magnitude value of -0.061 had 50 % of probability to belong to an actual deforestation event (Figure 2.2).

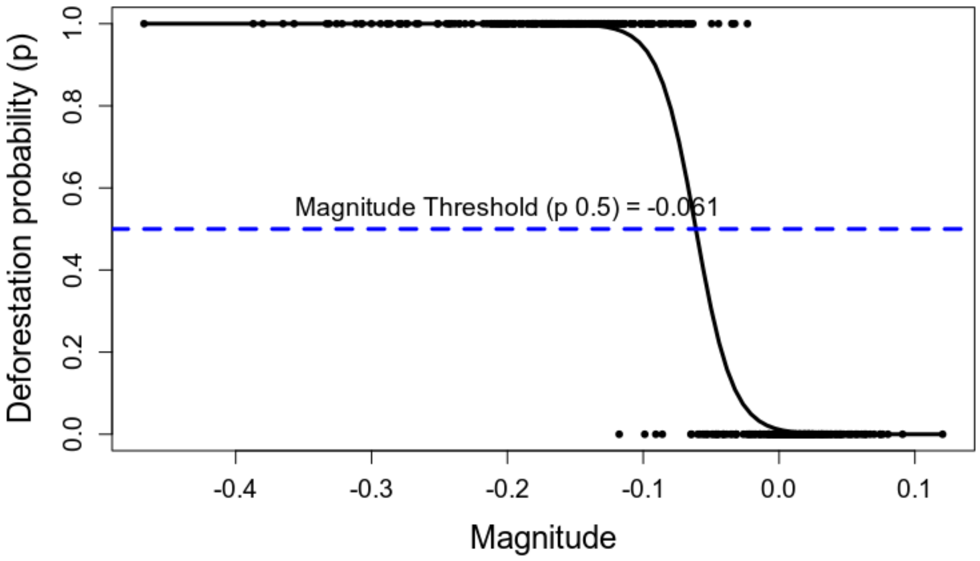

Figure 2.2. Binomial-logistic regression between magnitude and confirmed deforestation events. Although some magnitudes will overlap, the majority of negative magnitudes beyond our threshold belong to forest cover loss area derived from confirmed deforestation events.

2.3.2. SPATIAL DISTRIBUTION OF FOREST AGE

The spatial distribution of forest age is shown in Figure 2.3. Our results indicate that the greatest extents of young forests can be found in the semi-deciduous forest site, followed by the deciduous site and much smaller extents of young forests can be found in the semi evergreen site.

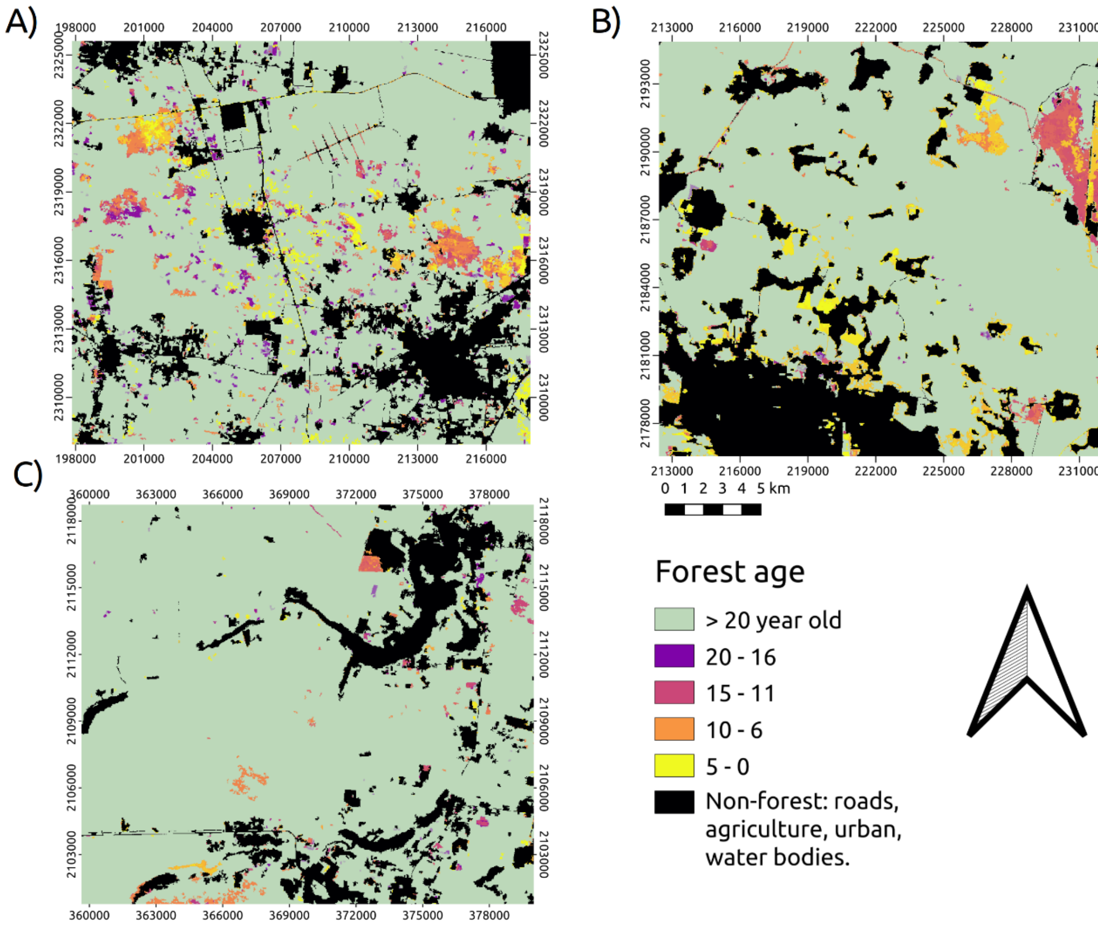

Figure 2.3. Spatial distribution of forest age grouped by categories of 5 years in a fraction of the 3600 km^2 for the three study sites (A) deciduous, (B) semi-deciduous and (C) semi-evergreen forests.

Temporal patterns of forest cover loss showed generally increasing trends over the study period (2000-2020) in deciduous and semi-deciduous forest, with the largest extent and highest variability corresponding to the semi-deciduous site (Figure 2.4). The semi-evergreen site showed a much smaller area of forest cover loss.

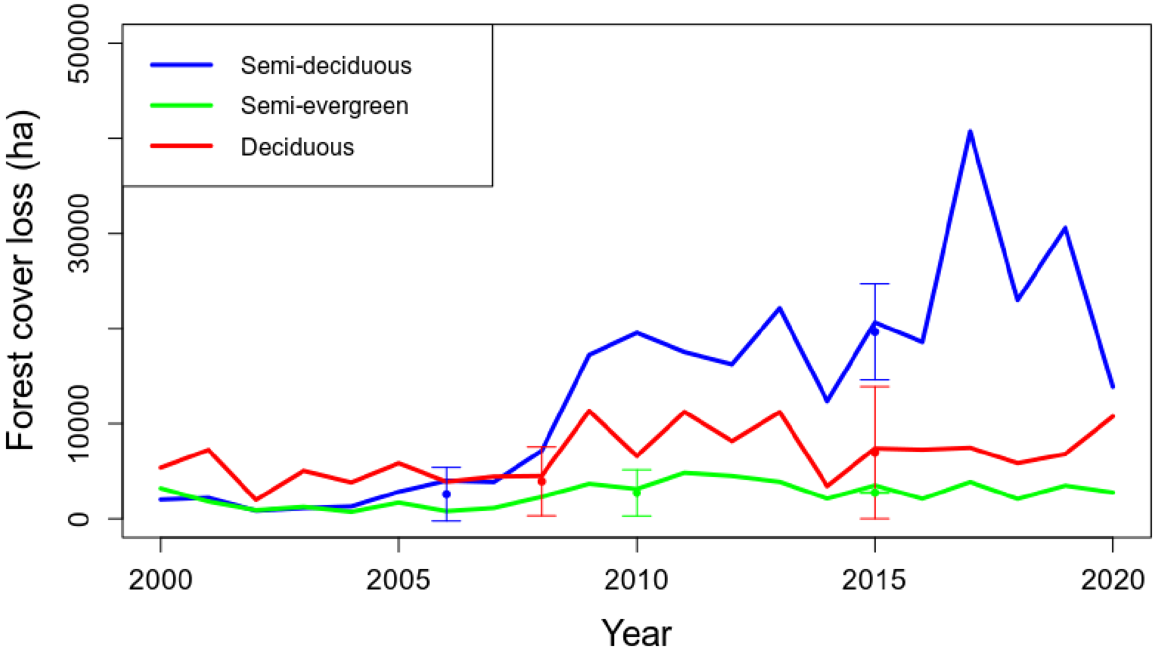

Figure 2.4. Total area of forest cover loss (ha) across time (Year) of change in our study sites. An overall increase in the extent of cover loss areas is observed in the semi-deciduous and deciduous sites compared to the semi-evergreen site.

2.3.3. VALIDATION OF FOREST COVER CHANGES DETECTED

Accuracy measures calculated differed between sites and years. Overall accuracy ranged from 95.7 to 99.9% and user's accuracy ranged from 87.3 to 98.5% (Table 2.1). Standard errors were low for the overall accuracy ranging from 0.01 to 0.98% as well as user accuracy, ranging from 0.02 to 3.2%. However, producer accuracy in the change class was considerably lower in deciduous forests (31.2 – 45.8%), and semi-deciduous forests (57.4 – 67.2%) sites compared to the semi-evergreen forests (66.8 – 99.9%). Producer accuracy showed a wide range of standard errors, ranging from 1.07 to 72.8% in the change class. Our lowest accuracy, in all three metrics, was found in the deciduous site (Table 2.1). Confusion matrices obtained from validation datasets are included in Supplementary material 2.4.

Table 2.1. Overall, user and producer accuracies ± standard errors in percent. Columns represent our map estimation and rows represent reference imagery.

Site	Year	Category	Producer's accuracy	User's accuracy	Overall accuracy
Deciduous	2008	Cover Loss	45.9 ± .72.8	87.3 ± 0.02	98.8 ± 0.51
		No change	99.9 ± 0.52	98.9 ± 1.7	
	2015	Cover Loss	31.2 ± 24.7	93.9 ± 2.1	95.7 ± 0.98
		No change	99.9 ± 1.04	95.8 ± 1.2	
Semi- deciduous	2006	Cover Loss	57.4 ± 29.1	92.6 ± 3.2	99.2 ± 0.39
		No change	99.2 ± 0.40	99.3 ± 1.2	
	2015	Cover Loss	67.2 ± 11.6	95.2 ± 1.8	96.9 ± 0.72
		No change	99.7 ± 0.78	97.04 ± 0.95	
Semi-evergreen	2010	Cover Loss	66.8 ± 24.4	97.9 ± 1.2	99.5 ± 0.34
		No change	99.9 ± 0.35	99.5 ± 0.71	
	2015	Cover Loss	99.9 ± 1.07	98.5 ± 1.1	99.9 ± 0.01
		No change	99.9 ± 0.01	99.9 ± 0.78	

The mapped area of forest cover loss, the adjusted area and 95 % confidence intervals are reported in Table 2.2. Our mapped area of forest cover loss was within the confidence intervals of the adjusted area of forest change in all three sites. Greater uncertainty was found in deciduous and semi-deciduous sites (Table 2.2).

Table 2.2. Estimated and adjusted area of forest cover loss and its uncertainty in hectares (ha) (95 % Confidence intervals) for each site and validation year.

Site	Year	Mapped area of forest loss (ha)	Adjusted area of forest loss (± 95% CI) (ha)
Deciduous	2008	4,501.7	3932.5 (± 3623.6)
	2015	7,397.8	6946.04 (± 6938.9)
Semi-deciduous	2006	4,004.4	3709.9 (± 2804.7)
	2015	20,650.3	19653.4 (± 5066.6)
Semi-evergreen	2010	3,128.9	3062.8 (± 2421.6)
	2015	3,499.7	3447.1 (72.7)

2.3.4. ABOVEGROUND BIOMASS ESTIMATED IN RECOVERING FORESTS

AGB estimations for < 20-year-old forests showed a mean of 66.1 (± 22.8) Mg ha $^{-1}$ for the deciduous site, 44.0 (± 23.2) Mg ha $^{-1}$ for the semi-deciduous site and 76.1 (± 31.3) Mg ha $^{-1}$ for the semi-evergreen site. A greater extent of young forest cover was found in the semi-deciduous site, followed by the deciduous site, and a smaller extent of young forest was found in the semi-evergreen (Figure 5).

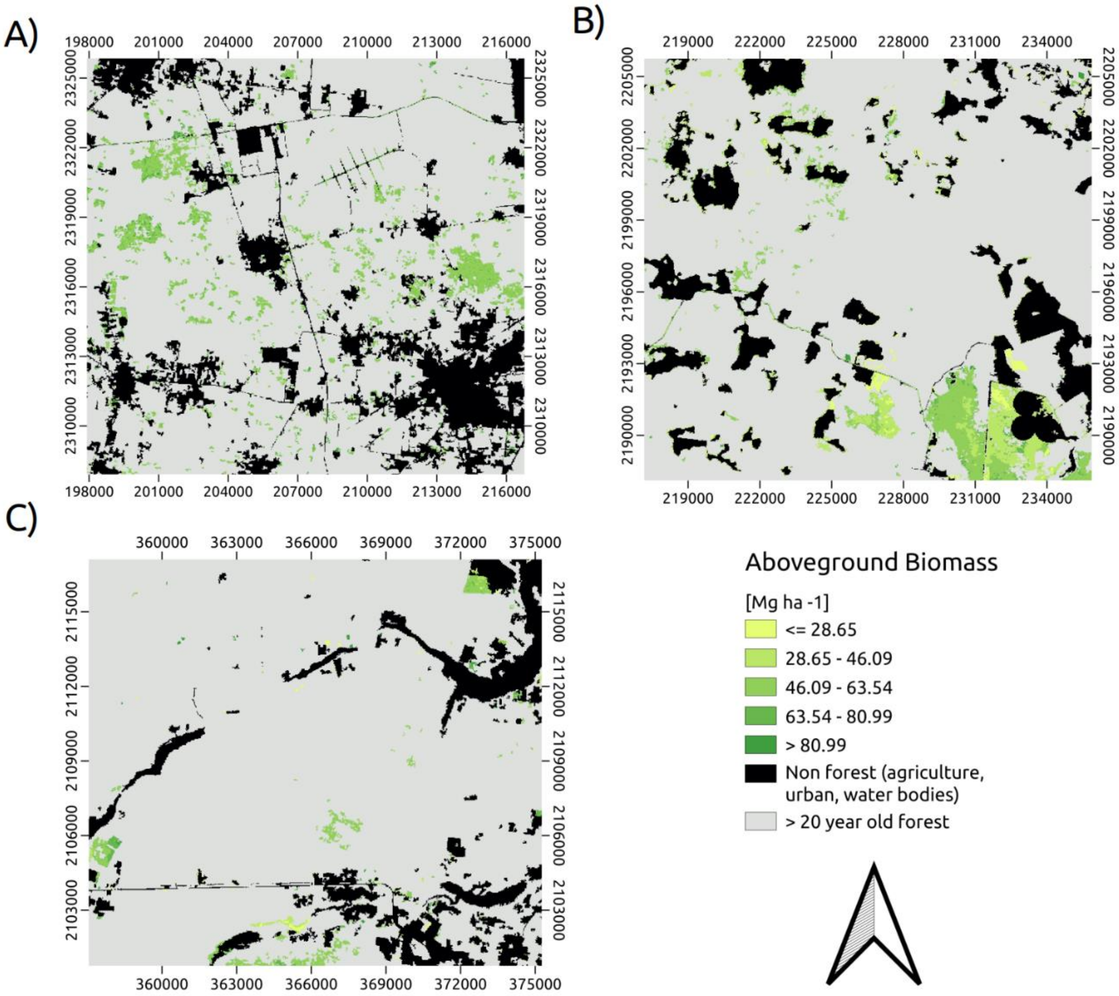

Figure 2.5. Spatial distribution of estimated aboveground biomass of young forest in a subset of the 3600 km^2 for the three study sites A) deciduous, B) semi-deciduous and C) semi-evergreen tropical forest.

Considering the possible error derived from temporal lags differences between observed and estimated forest cover change we calculated error maps and frequency histograms that are shown in Supplementary 6. Errors ranged from zero to 12 Mg ha^{-1} in our study sites. However, more frequent error are between 6 and 8 Mg ha^{-1}.

Our estimations of AGB of young forest were lower than those obtained by Cartus et al., (2014), Rodriguez-Veiga et al., (2016) and Hernandez-Stefanoni et al., (2020). They also were more similar to field estimates from the National Forest Inventory, although the estimated values of AGB from all studies (including this one) were significantly higher than the field reference data (Figure 2.6, Table 2.3).

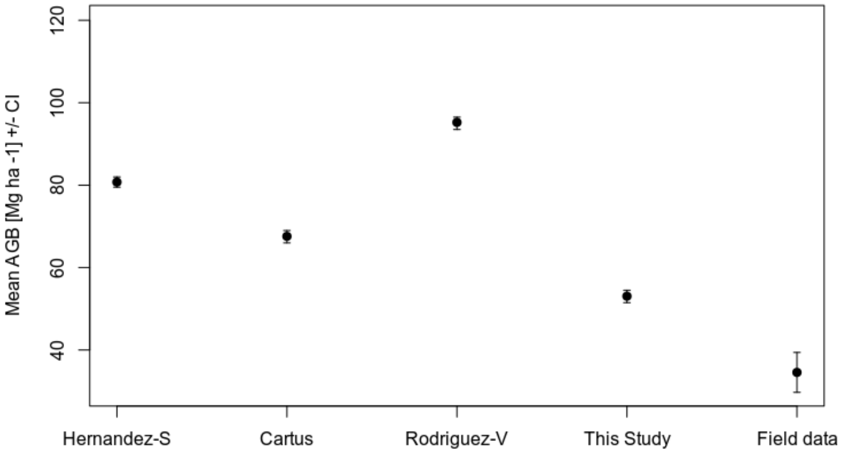

Figure 2.6. Mean aboveground biomass values and 95 % confidence intervals of young forests estimated from Hernandez-Stefanoni et al., (2020), Rodriguez-Veiga et al., (2016), Cartus et al., (2014), this study and National Forest Inventory Field data.

Table 2.3. Descriptive statistics (mean, standard deviation (± SD), 95% confidence intervals, and range) of estimated aboveground biomass in Mg ha -1 estimated in this study, Cartus et al., 2014, Rodriguez-Veiga et al., 2016, Hernandez–Stefanoni et al., 2020 and field reference data.

Estimation	Mean AGB (± SD)	CI 95%	Range
Hernández-Stefanoni et al., 2020	80.7 (± 33.2)	80.7 – 80.8	5.5– 226.5
Rodriguez-Veiga et al., 2016	95.2 (± 52.7)	95.2 – 95.3	2.08 – 197.9
Cartus et al., 2014	67.5 (± 34.6)	68.08 – 68.1	0.93 – 136.4
This study	53.06 (± 28.5)	53.04 – 53.08	11.2 – 98.4
Field reference data	37.5 (± 13.8)	26.4 – 48.6	12.9 – 48.9

2.4. DISCUSSION

The main objective of this research was to obtain spatially explicit estimations of forest age using the year of latest forest cover loss obtained from Landsat NDVI time-series. Then, we used this information to estimate AGB of young forest stands in three tropical dry forest sites in the Yucatan peninsula. Overall accuracy for the three stand age (latest forest-cover loss) maps ranged from 95 to 99%. These high values are comparable to those reported in other studies using BFAST to track loss of forest cover or 'deforestation' in tropical forests in Guanacaste, Costa Rica and Yucatan, Mexico (Smith et al., 2019); Bolivia (Dutrieux et al., 2015) and other forest types such as montane forests in Ethiopia (Devries et al.,2015) and in southeastern Australia (Verbesselt et al., 2010). This indicates that a big proportion of the cover change area in the map is located as land change in the field. However, the semi-deciduous and deciduous sites showed low producer accuracies, indicating high omission errors. Previous work has highlighted that higher omission errors in the same dataset are an indicator of underestimation of land changes in the class being evaluated (Smith et al., 2019). This error (calculated as 100 – producer's accuracy) is higher in the deciduous site, with the highest values in 2015 (68.7 %) and 2008 (54.1 %) in the cover loss class. This suggests an underestimation of the extent of young forests in the study area in general, and in the deciduous forest site in particular.

Total estimated area of forest loss and extent of young forest stands were larger in the semi-deciduous and deciduous forest compared with the semi-evergreen forest (Figure 3, Table 2). This result may reflect the combined effect of multiple factors both intrinsic to the analysis, such as the accuracy of the algorithm in the different sites and the vegetation index used, and extrinsic factors, such as climatic conditions of the site, proximity to urban settlements, land use and land tenure, which differ across sites. Variability in change detection has a direct impact on the estimation of the area of forest cover loss. The results of this research show that a greater number of change pixels were found in semi-deciduous and deciduous sites compared with the semi-evergreen site. Drier forests such as deciduous and semi-deciduous, tend to have a higher probability of cloud-free observations within the time series, and therefore, a greater probability to find significant change pixels within the time series (Smith et al., 2019).

Adjusted estimates of forest cover loss area also indicate greater uncertainties in the deciduous forest site (Table 2). The amplitude of the confidence interval suggests an underestimation of the forest cover loss area in the deciduous site, although all estimates fell within the estimated 95 % confidence interval. Underestimation of the area of forest cover loss in deciduous forests may be partly attributable to the properties of the vegetation index used. The sensitivity of greenness-based indices, such as NDVI, may be affected when rapid regrowth occurs after a clearing as red and near infra-red values saturate quickly (Grogan et al., 2016). Thus, if the timing of the imagery matches the regrowth period after a clearing event, a positive magnitude can be found in an area that was recently deforested. This area would be masked out of the analysis as we considered only negative change detection points as indicators of forest cover loss. This may be more accentuated in deciduous and semi-deciduous forest where swidden agriculture is more widespread than in semi-evergreen forest. Both medium scale and low impact swidden agriculture are practiced within the deciduous and semi-deciduous site, whereas the semi-evergreen site is dominated by selective logging in communally-owned areas and pastures for cattle although swidden agriculture is also practiced in the area. Land tenure has played a central role in shaping the patterns of loss of forest cover in central Yucatan where private and federal property showed significantly higher forest loss rates compared to communal property (Ellis et al., 2017). The low impact practices carried out in the semi-evergreen forests have been estimated to reduce disturbance and carbon emissions in the area, outperforming protection schemes carried out in protected areas (Ellis et al., 2019) and thus preserving mature forests within the area. This could help explain the higher producer accuracy estimates and smaller area of forest loss and young stands found in the semi-evergreen forest compared to the other two forest types.

It is important to consider that drivers of forest cover loss potentially differ in extent, frequency and magnitude among the three forest types assessed in this study. Repeated disturbances over the same area could be more extensive in semi-deciduous and deciduous forests where swidden and subsistence agricultural practices are common. Moreover, during the period of 2005 to 2010, twelve hurricanes impacted the Yucatan Peninsula (Mascorro et al., 2016). Although hurricanes strongly affect forest structure. Their effect on stand age is not only less clear and difficult to assess, due to the patchy nature of their impact but also, there is a confounding effect of prior land-use history. Many plant species have the capacity of resprout and regenerate (Uriarte et al., 2004; Bonilla-Moheno 2010; Heartsill et al., 2010; Mcgroddy et al., 2013) thereby affecting the probability of detecting negative changes in the NDVI time series. In addition, forest degradation, which is not explicitly considered in this study, is likely to have an impact on forest age and AGB estimation. In severely degraded forests increased mortality could signify forest cover loss below the 10% cover threshold (FAO 2020) and could also be considered as deforestation. Therefore, degradation could have an effect on the extension of younger forests and their differences in extent among the forest sites. On the other hand, forest degradation may also impact the AGB contained in the forest and not the forest cover, therefore estimations from passive sensors may overestimate AGB in degraded forest. Accurately characterizing forest degradation could improve mapping of forest age, however, there is much room for improvement in the assessment of the effect of degradation in the loss of forest cover. In particular, active sensors such as L-band ALOS-PALSAR and LiDAR show great potential for the monitoring of tropical forest change as they provide cloud free day observations of terrestrial ecosystems and have been used for the estimation of structural attributes of forests previously (Mitchard et al., 2009, Hernández-Stefanoni et al.,2020). However, ALOS-PALSAR data are unavailable prior to 2006 and the L-band saturates at >150 Mg ha $^{-1}$ (Mitchard et al., 2009) and LiDAR data are unavailable for large extensions therefore could not be used exclusively to track forest change. Data fusion from active and passive sensors could improve characterization of forest degradation. Considering the recent efforts in measuring forest degradation with active sensors have proven effective in tropical forests (Joshi et al., 2019), and in particular, with sufficient data availability, the fusion of LiDAR and SAR data could overcome limitations from previous estimations of forest loss in different vegetation types (Collins and Mitchard 2015).

An important goal of this study was to estimate the spatial distribution of AGB of young forests using the time since last forest cover loss as a proxy of stand age and chronosequence data to relate stand age to AGB. We also compared our AGB estimates to those from previous remote sensing studies such as Hernandez-Stefanoni et al., (2020), Rodriguez-Veiga et al., (2016), Cartus et al., (2014), and reference field data from the National Forest Inventory (CONAFOR). Even though our estimations were significantly higher than field estimated AGB, we obtained lower estimations compared to Hernandez-Stefanoni et al., (2020), Cartus et al., 2014 and Rodriguez-Veiga et al., 2016 in young forest stands. One factor which may have contributed to our overestimation is that we do not have chronosequence data from deciduous forest, instead we used the used the chronosequence from semideciduos forest to estimate AGB in both deciduous and semi-deciduous forest. Semi-deciduous forest has a relatively taller canopy (10-15 m) than deciduous forest (8 – 15 m) and also higher AGB. Therefore, lower AGB values from deciduous forest may not be captured by chronosequence data from the semi-deciduous forest.

Previous studies aimed at estimating AGB with remote sensing products have found that algorithms such as random forest tend to overestimate the AGB for younger stands (Zhao et al., 2016; Rodriguez-Veiga et al., 2018; Hernández-Stefanoni et al., 2020). A number of factors contribute to this overestimation such as the sensors sensitivity to changes in seasonality (Cartus et al., 2014), the algorithm used (Rodriguez-Veiga et al., 2016) and the sensor’s sensitivity to the presence of non-forest areas, canopy gaps and clearings (Hernández-Stefanoni et al., 2020). The comparison of AGB estimates from this study and previous ones, suggests that including information on the loss of forest cover as a proxy for stand age through time series of reflectance indices such as NDVI as used in this study might decrease this overestimation.

Current work has highlighted the importance of the sequestration potential of tropical dry forests (Chazdon et al., 2016), and particularly young forests (Cook-Patton et al., 2020). However, the comparison with previous AGB mapping efforts from Hernández-Stefanoni et al., (2020), Rodriguez-Veiga et al., (2016) and Cartus et al., (2014) shows that the carbon density in these areas might be currently overestimated. Here we estimate a lower forest biomass (~53.1 Mg ha^{-1}) in comparison to Hernández-Stefanoni et al., (~78.7 Mg ha^{-1}), Rodriguez-Veiga et al., (95.2 Mg ha^{-1}) and Cartus et al., (67.6 Mg ha^{-1}).

The semi-deciduous and deciduous forests of the Yucatan peninsula would contain a lower recovery potential (~44 Mg ha^{-1}) and (~66.9 Mg ha^{-1}) respectively, than the semi-evergreen forest (~76.1 Mg ha^{-1}). In addition, semi-deciduous and deciduous forests have larger areas in a stage of recovery compared to semi-evergreen forest. This would represent the lower carbon sequestration potential of these two vegetation types for the region. The Yucatan Peninsula is part of the REDD+ early actions program having high deforestation rates. Therefore, information on the carbon density of biomass of these forests, along with accurate spatial estimations of forest cover loss could be useful for implementing payments of ecosystem services, which could significantly contribute to the decrease of deforestation in the Yucatan, and for obtaining estimations of greenhouse gas emissions from deforestation for this area.

2.5. CONCLUSIONS

Estimations of the timing and extent of forest cover loss are important as they provide information on the spatial distribution of stand age. This is particularly challenging in seasonal forests, such as the tropical dry forests of the Yucatan, where the detection of forest loss from remote sensors can be confounded by seasonal and inter-annual variation in leaf phenology. BFast provided estimations of forest loss from significant changes in NDVI time series in tropical forests of the Yucatan Peninsula allowing to map forest cover loss with high overall and user's accuracy. Although producer's accuracy was considerably lower in semi-deciduous and deciduous forest indicating an underestimation of the forest loss area in these forest types, adjusted area of forest loss indicates that the area of change found in all three sites lies within the confidence intervals and the higher user's accuracy indicates that this area is likely to represent an event of forest cover loss.

Information on the timing and extent of forest cover loss can be used in conjunction with chronosequence data to estimate AGB and identify areas of young recovering forests where potential carbon sequestration is greater in tropical forests, and thus aid conservation efforts to protect the ecosystem services of young forests in tropical areas. Moreover, spatially explicit estimations of forest age, or the time since the latest forest cover loss event obtained from time series of satellite imagery show potential in reducing uncertainties associated to the overestimation of the AGB in young tropical forests from remotely sensed data.

2.6. ACKNOWLEDGMENTS

The authors would like to thank Erik Lindquist, and the USFS Silvacarbon for their guidance in the implementation of the BFAST algorithm. We also thank Fernando Tun-Dzul and Filogonio May Pat for their support during field work. The first author would like to thank CONACyT for the Ph D. scholarship awarded.

2.7. FUNDING

This research was financed by Ecometrica LTD and the United Kingdom Space Agency as part of the project Forests 2020.

The authors declare no conflict of interest.

CAPÍTULO III

3. USING SATELLITE ESTIMATES OF ABOVEGROUND BIOMASS TO ASSESS CARBON STOCKS IN A MIXED-MANAGEMENT, SEMI-DECIDUOUS TROPICAL FOREST IN THE YUCATAN PENINSULA

MANUSCRITO PUBLICADO EN GEOCARTO INTERNATIONAL
DOI:10.1080/10106049.2021.1980619

ABSTRACT

Restoration of tropical forests is widely seen as a key tool for mitigating climate change and fostering sustainable development and biodiversity conservation. However, there is a natural tension between forest management strategies prioritizing production and those highlighting other ecosystem services, such as carbon storage. Accurate estimations of the spatial distribution of forest aboveground biomass (AGB) and its uncertainty are important to evaluate the effectiveness of management and conservation policies which increase carbon sequestration in mixed management forest landscapes. However, in tropical forests, obtaining accurate estimations of AGB remains a challenging task due to the scarcity of field data and the lack of robust protocols to propagate uncertainty when upscaling these with remote sensing. We used a two-step upscaling process to map AGB at landscape scale across the Kiuic region of semi-deciduous tropical forest in the Yucatan peninsula. First, we calibrated a map of AGB using data from the GLiHT LiDAR campaign and from a field inventory, then calibrated a machine-learning model to upscale from the LiDAR survey across the wider landscape using backscatter and reflectance information from active (ALOS PALSAR) and passive (Sentinel 2) imagery respectively, as well as image texture. We propagated uncertainty using a Monte Carlo framework and explored the relative contributions of each sensor to explain variation in AGB. Finally, we used the upscaled biomass map to obtain the distribution of AGB in different management categories. In fitting the LiDAR-based map of AGB, a single sensor model using only Sentinel 2 data performed better (R^2 = 0.66) than one reliant solely on ALOS PALSAR backscatter (R^2= 0.50). Using both sensors led to the best performance (R^2 = 0.70). Incorporating the mean improved the precision of estimations of AGB using both sensors, although the effect was small. Comparing the upscaled map against the field inventory AGB estimates, the combined-sensor model explained 49% of the variation in AGB for plots within the LiDAR calibration area, and 17% outside this area. Importantly, 94% of observations outside LiDAR calibration area fell within our 95% confidence intervals, highlighting the robustness of our error prediction. Finally, the distribution of AGB under different management categories

showed differences between the protected areas. Protected areas had large areas of high AGB (>100 Mg ha $^{-1}$), whereas forested areas designated for production and restoration had large areas of low AGB (< 25 Mg ha $^{-1}$). This information is important for assessing the state of current carbon stocks and evaluating the effectiveness of different strategies for management, restoration and conservation of forest resources within the area.

3.1. INTRODUCTION

Tropical forests hold large stocks of carbon and play a key role in the global carbon cycle and its interactions with climate (Bonan et al., 2008; Pan et al., 2011; Mitchard, 2018). Carbon contained in aboveground biomass (AGB) is most susceptible to be emitted through deforestation and degradation, which are important sources of emissions in tropical forests (Houghton, 2005; Houghton et al., 2012, 2015). Accurate estimation of the spatial distribution of AGB and its uncertainty is an important part of the implementation of strategies aimed at reducing emissions through deforestation and degradation throughout the tropics, such as REDD +. However, previous research has underestimated the uncertainty due to inadequate methods for estimating and propagating errors throughout the estimation process (Yunai et al., 2020).

The Yucatan Peninsula, located in the south-eastern part of Mexico, holds one of the largest extents of continuous tropical dry forest in Latin America (Dupuy et al., 2015). Mexico is an active participant in the REDD+ initiative, and particularly, the Yucatan Peninsula is a part of the REDD+ early actions priority areas, due to increasing pressure of permanent conversion to urban areas and the expansion of agriculture (Ellis et al., 2017). Several protected areas targeting conservation of forest resources are located within the Yucatan Peninsula (CONANP, 2017) encompassing old-growth forests. However, the extensive use of traditional agricultural practices, such as slash-and-burn agriculture, as well as other land use such as agricultural areas and pastures for cattle ranching, shapes the landscape outside the protected areas into a mosaic of forest areas in diverse stages of natural regeneration, with biodiversity and forest biomass gradually recovering after abandonment (Dupuy et al., 2012). In line with global policy efforts to restore forests across the tropics, significant areas of the Yucatan Peninsula have been allocated for restoration (CONANP, 2017). Whether this restoration will lead to significant carbon sequestration, and thus help mitigate climate change, will depend on the balance between forest loss through deforestation and degradation (including the exploitation of forest resources) and forest gain from forest regrowth from conservation and natural regeneration of disturbed areas (Lewis et al., 2019; Chazdon et al., 2016; Houghton, 2013).

The balance between forest (re)growth and disturbance determines the distribution of AGB (Williams et al., 2013). Post-disturbance, forest ecosystems can aggrade, accumulating carbon until they reach a quasi-steady state, where gains through growth and recruitment become balanced by mortality losses. At steady state the distribution of AGB within the landscape tends towards a normal distribution (Williams et al., 2013). In disturbed forests, on the other hand, repeated removal of AGB results in a skewed distribution of AGB, resulting in a long tail of low AGB values. Therefore, information on the distribution of AGB can be used to assess the state of AGB stocks in areas under different management strategies.

Reliable estimates of the spatial distribution of forest AGB are essential for effective forest management, to detect areas of loss and assess the success of conservation efforts. To date, AGB across Mexico has been mapped in a number of National(Cartus et al., 2014b; Rodríguez-Veiga et al., 2016), Urbazev et al., 2018) and pan-tropical (Saatchi et al., 2011; Baccini et al., 2012., Avitabile et al., 2016) products. However, there are large and systematic uncertainties (Mitchard et al., 2013) with existing maps, which tend to underestimate the AGB in the Yucatan Peninsula (Rodriguez-Veiga et al., 2019; Hernández-Stefanoni et al., 2020), leading to potential underestimation of carbon emissions from deforestation and degradation.

Production of regional AGB maps typically relies on upscaling field estimates of AGB based on a relationship between a network of field inventory plots (Jerome Chave et al., 2004; Réjou-Méchain et al., 2014) (Chave et al., 2004; Réjou-Méchain et al., 2019) and remotely sensed data (Goetz et al., 2015). A number of passive sensors (e.g. multispectral optical imagery from Sentinel) 2) and active sensors (e.g. L-band Synthetic Aperture Radar (SAR) from Advanced Land Observation Satellite) (ALOS PALSAR; Shimada, 2010)(Shimada et al., 2014) are available that offer frequent coverage at global scales. Each sensor has its own limitations. Optical data are limited by cloud and smoke, both common in tropical forests (Asner et al., 2001); SAR penetrates clouds, and polarized backscatter has been shown to be sensitive to AGB (Mermoz et al., 2015; Thapa et al., 2015; Mitchard et al., 2009), however, optical and L-band saturate at ~150 Mg ha-1 (Lu et al., 2006; Mitchard et al., 2009; Joshi et al., 2017). Compared to tropical wet forests, old-growth tropical dry forest canopies are generally shorter and simpler, and AGB correspondingly lower (Murphy and Lugo 1986). Therefore, the AGB range occupied by tropical dry forests is potentially still within the sensitivity range of L-band systems. Multi-sensor approaches can leverage the strengths of these various data sources to improve AGB estimates (Bispo et al., 2020).

Generating maps of AGB based on satellite data requires calibration against estimations of AGB typically taken from field inventories (e.g. Rodriguez-Veiga et al., 2016; Saatchi et al., 2011; McNicol et al., 2018). High-resolution airborne LiDAR surveys offer the potential to bridge the scale gap between inventory plots and satellite data and enhance the range of training sites over which to calibrate models (Urbazaev et al., 2016; Wulder et al., 2012; Asner et al., 2018; Bispo et al., 2020). LiDAR is particularly powerful as it captures precise information on forest structure without signal saturation in dense tropical forests (Lefsky et al., 1999; Asner et al., 2014). However, the cost of obtaining airborne LiDAR data through on-demand surveys is high. Consequently, publicly available data are typically scarce over many tropical forests. The GEDI mission offers global open, spatially distributed waveform LiDAR (Dubayah et al., 2020), which will undoubtedly facilitate calibration of satellite-based biomass products (e.g. Qi and Dubayah, 2016). However, GEDI has a nominal mission lifetime of two years from its on-orbit checkout in April 2019, thus limiting its scope for future and past monitoring of change in tropical forests. Therefore, it is important to develop methods that utilize spatially limited airborne surveys inside upscaling frameworks and quantify their predictive uncertainty with robust error estimation (Zhao et al., 2020). In developing upscaling frameworks, particularly when working with spatially limited data, it is critical to account for spatial autocorrelation to avoid overfitting and thus greatly overstating the predictive power of upscaled models (Roberts et al., 2017; Ploton et al., 2020).

This research has two core aims: (i) to produce accurate spatially explicit estimations of AGB and its uncertainty in a semi-deciduous tropical dry forest of the Yucatan Peninsula; (ii) to quantify the effectiveness of active and passive sensors and their combination for achieving (i). We develop an upscaling framework that uses airborne LiDAR surveys as an intermediate step to link field inventory AGB estimates to Sentinel 2 and ALOS PALSAR data. First, we generate a LiDAR AGB model, AGBLiDAR, calibrated using field inventory data. Subsequently, we use a machine-learning framework to upscale these AGBLiDAR maps with satellite data from Sentinel 2 and ALOS PALSAR to generate a satellite-based model for AGB, AGBSAT. Previous studies suggest image texture metrics can improve estimates of AGB in dense forests (Castillo et al., 2005; Wood et al., 2012; Thapa et al., 2015; Hernández-Stefanoni et al., 2020). We therefore explore the potential for texture variables to improve the predictive power of our machine-learning models. We assess the effect of spatial resolution in the calibration of the LiDAR-to-satellite model and explore the improvement in performance of multi-sensor models over single-sensor models. We propagate uncertainty through the analysis using a Monte Carlo framework, including a spatially independent cross-validation strategy for robust estimates of errors arising during upscaling (e.g. Roberts et al., 2017). Finally, we use the AGBSAT map to gain insight into the impact of forest management (production vs. protection) on forest biomass, and thus the likely carbon sequestration potential for areas set aside for restoration in this region.

3.2. METHODS

3.2.1. STUDY AREA

The study area comprises 3600 km^2 of tropical dry forest in the centre of the Yucatan Peninsula, Mexico, located between 20° 09’ 39” and 19° 37’ 08” N latitude and 89° 16’ and 89° 50’ 36” W longitude (Figure 1). The vegetation at this site is predominately semi-deciduous tropical dry forest, sitting in the transition zone between deciduous tropical dry forest in the drier northern part of the Peninsula and semi-evergreen tropical forest in the south-west (Rzedowski 2006). Trees in this region are typically 8–15 m tall, and 50–75 % of trees drop their leaves during the dry season, which typically falls between November and April (Carnevali et al., 2003). The limestone terrain underlying this region is characterized by a mixture of low hills (elevation range: 16–216 m) and flat areas. Three protected natural reserves exist within the study area: Kaxil Kiuic Biocultural Reserve (Reserva Biocultural Kaxil Kiuic) (1,800 ha) a private reserve located inside a state protected area: del Puuc Biocultural reserve (Reserva Estatal Biocultural del Puuc) (135,849 ha), and a small fraction (~ 5,000 ha) of the Bala’an K’aax national protected area (128,390 ha) (CONANP 2017) (Figure 1). Several low impact subsistence activities occur in the adjacent forest surrounding the Kaxil Kiuic reserve (swidden agriculture, with some selective logging and cattle grazing) and agricultural fields. Unprotected forest areas are subdivided into areas suitable for production of forest species and areas suitable for forest restoration. These areas were designated according to structural characteristics such various degrees of degradation in the restoration forest and tree cover for production forest. For a detailed description refer to CONAFOR (2013).

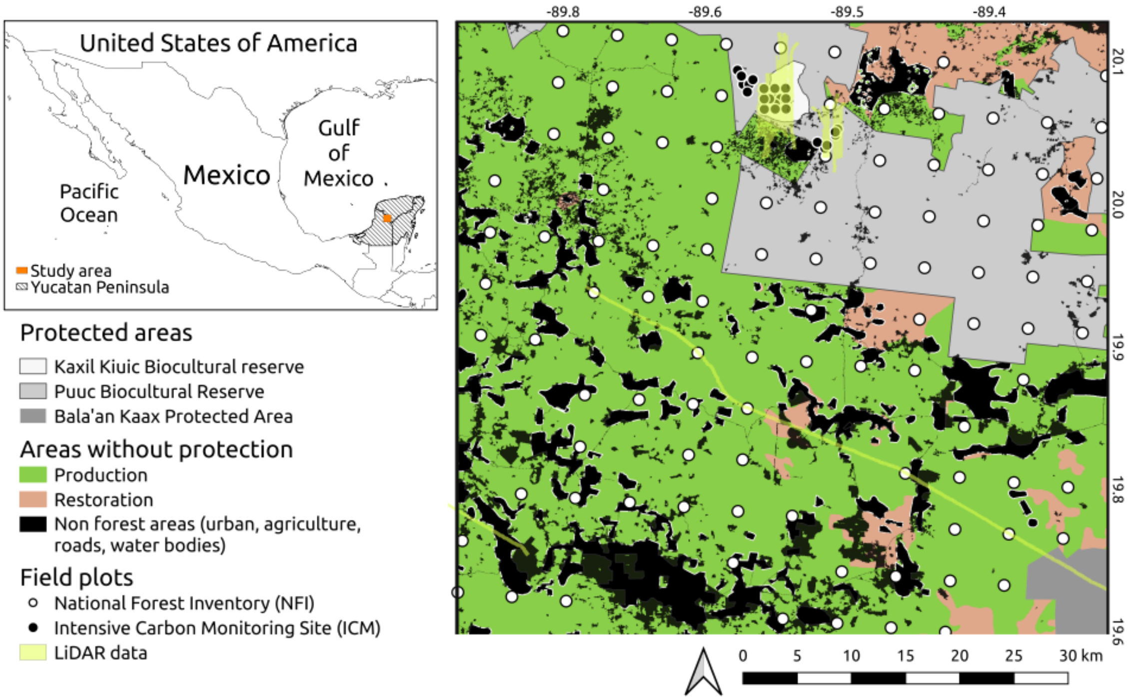

Figure 3.1. Location of study area in Mexico (upper-right box) and location of protected areas within study area, LiDAR and field data used in this study. National Protected Area (Bala'an K'aax), State Protected Area (del Puuc Biocultural Reserve) (CONANP 2017) and private protected area (Kaxil Kiuic Biocultural Reserve). Areas without protection are subdivided into areas suitable for production and those suitable for restoration (CONAFOR 2015).

3.3.2. FIELD INVENTORY DATA

Field data were taken from two surveys: (i) The Intensive Carbon Monitoring (ICM) site; (ii) a sparser, spatially more extensive dataset across the region, obtained from the Mexican National Forest Inventory (NFI). The majority of plots (20) from the ICM are located within the Kaxil Kiuic Biological Reserve, and 12 are placed outside the reserve boundary in a chronosequence in several ages of abandonment. (Figure 1). In both cases, clusters of four GPS-located circular subplots of 400 m^2 each were distributed systematically with one central plot surrounded by three peripheral plots at 90°, 120° and 240° azimuths within a 1 ha sampling area (CONAFOR 2013). Within each plot, height and Diameter at Breast Height (DBH Diameter at 1.30 m) were recorded for all woody plants with DBH > 7.5 cm and each individual was identified to species level. In addition, small stems (2.5 cm ≤ DBH < 7.5 cm) were also measured at the ICM plots, within a central subplot of 80 m^2 (Sosa et al., 2016). AGB was calculated for each tree using the allometric equation of Chave et al., (2005) for trees with DBH ≥ 10 cm, and that of Ramírez-Ramírez et al., (2017), for trees with DBH < 10 cm, based on DBH and height from the above-mentioned datasets. Wood densities were taken from Sanaphre-Villanueva et al., (2016) where species were present in the database, otherwise a mean value of wood density at the genus or the plot level were used. Plot AGB was estimated based as the sum of the AGB of all individual trees. In the ICM plots, the contribution of small stems averaged 24.4 ± 13.5 Mg ha $^{-1}$. This contribution was added to the NFI plots to standardize the two datasets. In total, 33 plots (132 subplots) fell within the LiDAR survey. A further 435 fell outside the survey, providing independent validation of the final upscaled map outside the LiDAR survey.

The workflow of methods applied in this research is displayed in supplementary material 1 and described in more details in the following section.

3.3.3. LIDAR DATA

We obtained LiDAR data from NASA's Goddard's LiDAR, Hyperspectral and Thermal (G-LiHT) airborne imager (Cook et al., 2013) available for the study area (Figure 3.1). The LiDAR point cloud was pre-processed using the USFS FUSION software (McGaughey, 2012) resulting in two 1-m resolution raster representing the top of canopy elevation and the underlying topography. The difference in elevation between these surfaces provides a direct estimate of canopy height.

3.3.4. ALOS PALSAR AND SENTINEL-2 DATA PROCESSING

Two scenes of Advanced Land Observation Satellite Phased Array L-Band Synthetic Aperture Radar (ALOS PALSAR) yearly mosaics at 25 m spatial resolution for the year 2015 were merged to cover the extent of the study area. The images, obtained in digital numbers, were converted to backscatter coefficient by means of the formula provided by (Shimada & Ohtaki, 2010). Afterward, they were pre-processed to obtain gridded, topographically corrected backscatter amplitudes for HH and HV polarizations (Mitchard et al., 2009). The ALOS PALSAR backscatter was processed to remove "speckle" (Woodhouse, 2017) using the standard enhanced Lee filter (Lee 1980), as implemented in the GIS software package ENVI 5.0 (Hernández-Stefanoni et al., 2020).

Two Sentinel 2A scenes corresponding to April 2017 were mosaicked using linear normalization in order to produce a seamless mosaic of the study area. We used the following bands: blue (492.4 nm, hereafter named as Band 1), green (559.8 nm, Band 2), red (664.6 nm, Band 3) and near infrared (832.8 nm, NIR, Band 4) with a spatial resolution (pixel size) of 10 m. Also, we calculated the Normalized difference vegetation index (NDVI).

We also used image texture metrics such as Gray Level Co-occurrence Matrix (GLCM) (Haralick, 1979) since they are able to capture the spatial variability in the spectral response of different elements in the landscape and have been related by previous work to variability in forest structure (Gallardo-Cruz et al., 2012, Wood et al., 2012). These statistics can be categorized into homogeneity and heterogeneity metrics. Higher values in metrics such as contrast and dissimilarity indicate a higher variability in the elements in an area, whereas metrics such as homogeneity, second moment and correlation, indicate similarity within an area. The mean and variance of the surface reflectance of bands in addition to the aforementioned GLCM measures (hereby texture measures) were calculated at the spatial resolution of the LiDAR-satellite upscaling step for all individual bands and for NDVI using scikit-image, a collection of algorithms for image processing in python 3.6 (van der Walt et al., 2014).

3.3.5. UPSCALING FIELD INVENTORY TO REGIONAL AGB

In order to estimate the spatial distribution of AGB we carried out a two-step process: (1) creation of the LiDAR AGB map, AGB_{LiDAR} at 20 m resolution, corresponding to the resolution of the individual 0.04 ha inventory plots (AGB_{field}); (2) upscaling AGB_{LIDAR} across the study area using machine learning models based on data from Sentinel 2 and/or ALOS PALSAR to produce AGB_{SAT}.

3.3.6. SPATIAL MAPPING OF AGB WITH LIDAR

The first step in upscaling the field inventory AGB estimates (AGB_{Field}) was to extrapolate these across the LiDAR survey extent. To do this we fitted a power law relationship between the AGB of the 0.04 ha inventory plots and the mean top of canopy height (TCH) measured by the LiDAR sensor within the footprint of each 0.04 plot (Figure 2). This follows from the allometric expectation of power law scaling of AGB with tree height, and therefore stand height (e.g. Asner & Mascaro, 2014). To reduce the risk of bias in canopy height estimates from areas of low point density (Roussel et al., 2017), we filtered out areas of the survey with less than 6 pts m^2. We also investigated alternative variants and canopy metrics, including gap fraction (e.g. Jucker et al., 2017), but these did not lead to significant overall improvement in the model under leave-one-out (LOO) cross validation.

To model the power law relationship, we fitted a linear mixed effects model in log-transformed space to account for the hierarchical structure of the inventory data (i.e. four 0.04 ha plots within each plot cluster):

$$[ln(AGB_{LiDAR})]_{i,j} = \alpha + \beta^{*}[ln(TCH)]_{i,j} + u_i + \varepsilon_{i,j},$$

where *i* represents the plot cluster, *j* represents the plot within the cluster, α is the intercept term, β is the fixed effect for $ln(TCH)$, $u_i$represents a random effect associated with the plot cluster *i*, and $\varepsilon_{i,j}$ represents the residuals for each plot. Finally, after back-transformation of the final estimates, we applied the necessary correction factor (Baskerville, 1972):

$$CF = exp\ \left(\frac{\sigma^2}{2}\right).$$

where σ^2 is the RMSE of the model fit in log-space. The RMSE under Leave-One-Out (LOO) cross validation (Supplementary 1) was 46.14 Mg ha^{-1} and the R^2 was 0.40, for a spatial resolution of 0.04 ha. Relatively high RMSE values are in line with expectations for small plot sizes (e.g. Mascaro et al., 2011b), but relative errors should drop considerably when aggregating across larger regions (Gonzalez et al., 2010).

3.3.7. UPSCALING AGB WITH SATELLITE DATA

In order to produce spatially explicit estimations of AGB in the Kiuic landscape we upscaled the AGB$_{LiDAR}$ map with the satellite data using random forest regression (Breiman, 2001), with a bootstrap bias correction (Hooker & Mentch, 2018; Xu et al., 2016). Random forest regression is a flexible, non-parametric machine learning algorithm that has previously been employed to fuse LiDAR and satellite data and produce maps of AGB and other structural parameters (e.g. Luther et al., 2019; Mascaro et al., 2014; Urbazaev et al., 2018; Wulder et al., 2012). Random forest models were fitted using the implementation of scikit-learn in Python (Pedregosa et al., 2011). To optimize the random forest regression models, we employed a Bayesian hyperparameter search seeded with 100 random trials, followed by a further 350 iterations (Bergstra et al., 2013). To determine the best spatial resolution at which to undertake the LiDAR-satellite upscaling, we tested the effect of aggregating to three different spatial resolutions (20 m, 50 m and 100 m). The relative importance of the sensors and textures to explain the variation in AGB in the fitted models was explored based on the drop in R^2 following permutation of each variable (permutation importance e.g. Strobl et al., 2007). Given the strong collinearities between texture metrics for different bands, we permuted all variables associated with (i) each sensor, and (ii) each texture index, to capture their contributions more concisely. Finally, we compared the performance of the combined Sentinel 2/ALOS PALSAR model against single-sensor models to investigate the improvement in predictive power provided by the complementary attributes of these sensors.

3.3.8. ERROR PROPAGATION

Robust characterization of uncertainty is critical to understanding the utility and limitations of remotely sensed maps of AGB (Ploton et al., 2020). Uncertainty arises from a multitude of factors. Uncertainties in the field AGB estimates (Chave et al., 2004), combined with spatial registration errors (Hernández-Stefanoni et al., 2018), crown overlap at plot boundaries (Mascaro et al., 2011); and temporal lags (Babcock et al., 2016; Clark and Kellner, 2012) lead to uncertainties in AGB_{LiDAR}. These uncertainties are compounded by unexplained variance in the subsequent LiDAR-satellite upscaling model. In addition, geospatial data are frequently spatially autocorrelated. In scenarios like this one, the clustered geometry of the available LiDAR data survey precludes the robust inclusion of a spatial effect into the random forest models through additional spatial covariates (e.g. Mascaro et al., 2014). Spatial autocorrelation, if not accounted for, can lead to overfitting resulting in significant underestimation in predictive error during cross-validation and misleading diagnostic analyses regarding feature importance (Ploton et al., 2020; Roberts et al., 2017).

In order to propagate uncertainty in the upscaling process we employed Monte-Carlo simulations to propagate errors across every step of the upscaling framework (Hernánde-Stefanoni et al., 2020). Uncertainty in AGB_{field} was estimated based on estimates of uncertainty in the biomass of individual trees, assumed to be 47% of tree AGB (see Chave et al., 2004). Uncertainties between trees were assumed to be independent and thus they were aggregated at the plot-level by adding in quadrature (the square root of the sum of squares), a standard procedure for combining uncorrelated errors (Yanai et al., 2020). Relative errors at the plot level were therefore significantly lower and tended to be dominated by the largest trees. To characterize the uncertainty in AGB_{LiDAR}, we fitted the mixed effects model 100 times. In each iteration we resampled the biomass of AGB_{field} assuming normally distributed uncertainties. We accounted for spatial registration errors by shifting the plot location randomly assuming a standard deviation of 5 m in the plot coordinates. Corresponding uncertainties in TCH were strongly non-normal in some cases, particularly close to forest edges. We did not attempt to account for canopy overlap, or temporal lags. Fitting the model 100 times produced 100 candidate AGB_{LiDAR} maps for upscaling with the satellite data.

To propagate uncertainty across the LiDAR-satellite step, the 100 AGB_{LiDAR} maps were used as the target for an ensemble of 100 random forest models. To account for predictive uncertainty of these models, we also fitted a model to predict the median AGB_{LiDAR} using a 16-fold buffered, blocked cross validation procedure, whereby the training data were split into square blocks (block width 1 km), and randomly allocated to one of the folds. In each iteration, we buffered the validation set by a distance of 500 m to reduce the impact of spatial autocorrelation and therefore minimize overfitting (Note that in the optimization and feature importance calculations, only five folds were used to reduce processing time). This spatial cross-validation was undertaken for the three tested upscaling resolutions (20 m, 50 m and 100 m) to determine the best option for upscaling (Figure 4). Errors in predicted AGB resulting from fitted spatial correlations were modelled by resampling from the residuals from the results of this cross-validation (using median AGB_{LiDAR}). As the residuals were not uniformly distributed along the range of predicted AGB ($AGB_{upscaled}$), residuals were resampled from a 20 Mg ha^{-1} window around the AGB estimate for each pixel. Thus, the 100 x 100 iterations of the upscaling procedure capture both uncertainty in AGB_{LiDAR} propagated through the random forest models, and the predictive uncertainty associated with fitting models with spatially autocorrelated data. We present the median and 95% confidence intervals as our best estimates and uncertainty in the upscaled AGB maps ($AGB_{upscaled}$).

The AGB map obtained in this study was compared with previous AGB maps generated by Santoro et al., (2018), Rodriguez-Veiga et al., (2016) and Cartus et al., (2014). We performed a validation between field AGB data used in this study for validation and estimated AGB values from our AGB map and the previously mentioned maps. We also calculated the root mean square error (RMSE) and the relative root mean square error (%RMSE) obtained as the RMSE divided by mean AGB observed values for comparisons.

3.3.9. RELATIVE CONTRIBUTIONS BY SENSOR

In order to obtain the relative contributions by sensor, we partitioned the information provided by (a) Sentinel 2 reflectance and texture; (b), ALOS PALSAR backscatter and texture; and (c) shared variation, which is the variance in AGB that can be explained by either sensor. Total variation explained by the full model using information from both sensors can be summarized as: $Y = (a + b + c) + \varepsilon$, where ε is variation that cannot be accounted for by the predictor variables. The relative contribution of the two sensors and the shared variation can then be partitioned by comparison against the variance explained by single sensor models using only Sentinel-2 (a + c) and only ALOS PALSAR (b + c).

3.4. RESULTS

3.4.1. CALIBRATING LIDAR BIOMASS ESTIMATES AT THE PLOT SCALE

Validation of the AGB TCH model had an R^2= of 0.40, RMSE of 46.14 Mg ha^{-1} between AGB measured by Top of Canopy Height (TCH) and our field calculated AGB (in 400 m^2 plots). Due to spatial uncertainty, heterogeneous canopies can result in large uncertainties in plot TCH, particularly where plots are located at or close to sharp transitions between short, secondary vegetation and old-growth forest. In this case, three field plots showed large residuals in the validation of the AGB TCH model (Figure 3.2). This derives from the presence of very large trees inside these plots which increase the field calculated biomass considerably, without a corresponding increase in height or TCH. Nevertheless, at 20 m resolution, estimations of AGB using LiDAR TCH show a good fit with the power law relationship (Figures 3.2, Supplementary 1).

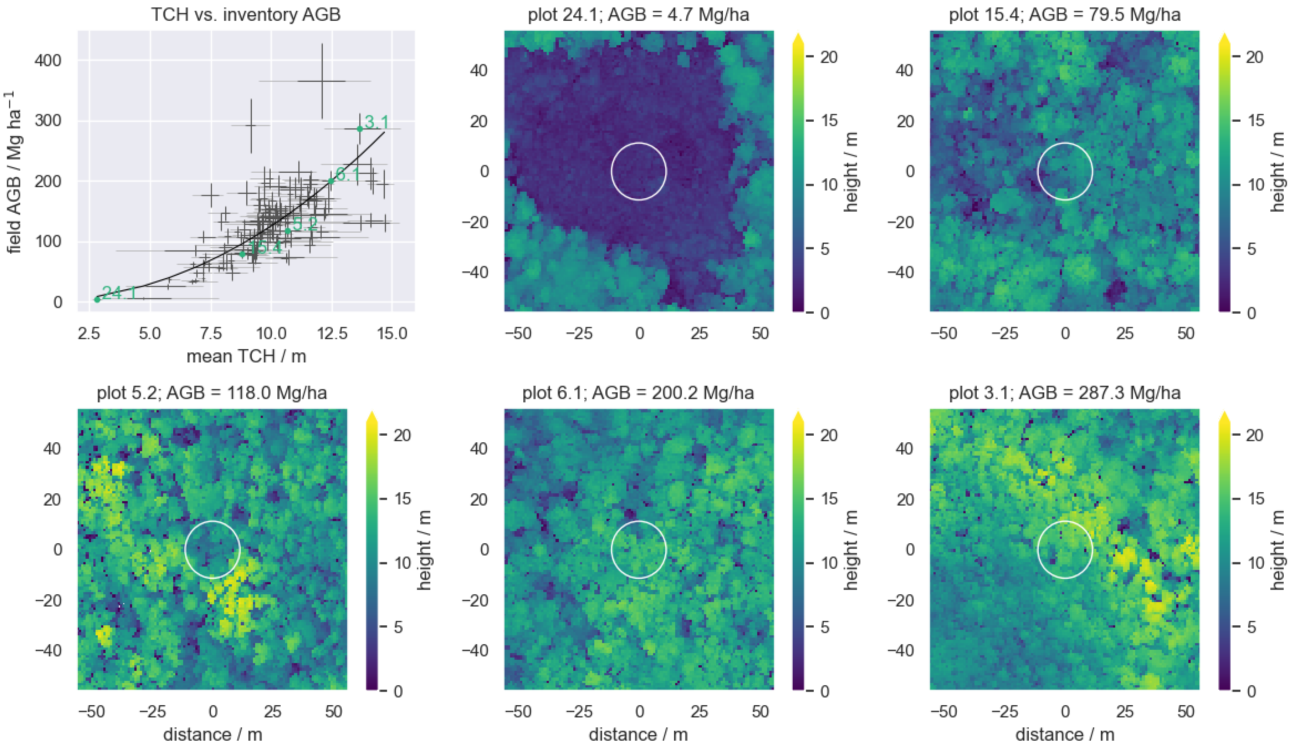

Figure 3.2. Comparison of field inventory AGB and LiDAR TCH for the 0.04 ha

inventory plots, shown with a series of example plots (numbers in blue) highlighting variations in TCH across the range of AGB spanned by the plot network. In the first panel, the line is the fitted relationship between field AGB and plot TCH. Error bars (horizontal and vertical lines) represent the uncertainty in plot field AGB (points), and the uncertainty (both 50% CI and 95% CI shown) in plot TCH, modelled by randomly sampling the TCH with positional uncertainty.

3.4.2. UPSCALING AGB USING SINGLE SENSOR AND COMBINED MODELS

Models upscaled at 100 m resolution provided greater explanatory power (R^2 = 0.70, RMSE = 27.9%) than either models upscaled at 50 m (R^2 = 0.67, RMSE = 29.8%) or 20 m resolution (R^2 = 0.62, RMSE = 31.8%), after aggregation post-upscaling to the same resolution grid (i.e. 100 m). This highlights that the reduction in noise by averaging spatially prior to upscaling led to a more robust upscaling model. Therefore, we only consider the 100 m resolution models from now onwards.

The upscaled models were clearly able of distinguishing forest from non-forest cover (Figure 3.3). However, sensitivity to AGB variations within the forest area was limited, especially for models reliant only on ALOS PALSAR, which had very little explanatory power regarding AGB variations above 100 Mg ha^{-1} (Figure 3.3). The best upscaling model combined both Sentinel 2 and ALOS PALSAR (R^2 = 0.70; RMSE = 27.8%). In comparison, the Sentinel 2-only model had slightly lower predictive power (R^2 = 0.66; RMSE = 29.5%), while the model solely reliant on ALOS PALSAR performed worst (R^2 = 0.50; RMSE = 36.2%). Sentinel 2 explained a greater amount of variation of AGB (20%) solely compared to ALOS PALSAR (4 %). The majority of the explained variation (46% of the total variance) was shared between both sensors. Uncertainties in the combined model and in the Sentinel 2 model were highest in the mid-range of AGB < 100 Mg ha^{-1}. Conversely, ALOS PALSAR showed higher uncertainty above 100 Mg ha^{-1}, as its sensitivity saturated (Figure 3.3).

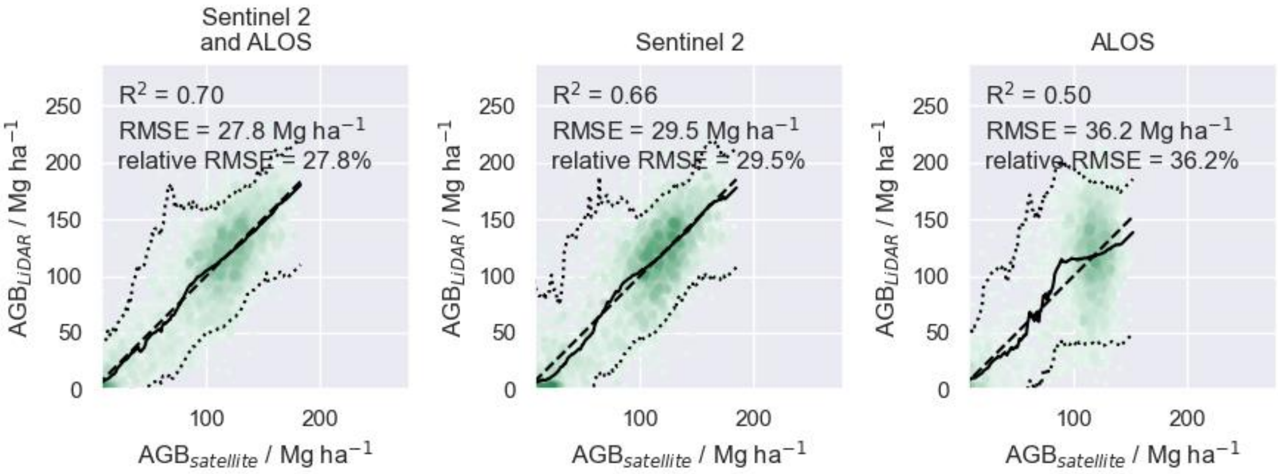

Figure 3.3. Regression lines, R2, RMSE and relative %RMSE based on a five-fold buffered-blocked cross-validation between LiDAR estimated AGB (AGB_{lidar}) and upscaled AGB ($AGB_{satellite}$) for models using both sensors a), Sentinel 2 reflectance and textures b), and ALOS PALSAR and textures c). The dashed line represents the 1:1 relationship, the solid and dotted lines represent the median estimate and 95% confidence interval for a 20 Mg ha-1 moving window across the predicted AGB range ($AGB_{satellite}$).

3.4.3. RELATIVE CONTRIBUTIONS BY SENSOR AND VARIABLE IMPORTANCE

Sentinel 2 explained a greater amount of variation of AGB (20 %) by itself, compared to ALOS PALSAR (4 %), although a considerable amount of variation was shared between both sensors (46%). Sentinel 2 on its own was able to provide reasonable estimations of AGB in the study area, explaining 66 % in the single sensor model, whereas ALOS PALSAR proved to be less effective explaining 50%, while the combination of sensors provided the best fit (70 %).

The results of the permutation importance under spatial cross-validation highlighted the relative importance of Sentinel 2 reflectance and texture measures over ALOS PALSAR in the random forest model (Figure 3.4). Moreover, of the texture metrics, only the mean of AGB showed a high importance in the model. Variables relating to heterogeneity (variance, contrast, dissimilarity) had marginal importance. Variables relating to homogeneity (correlation, angular second moment 'ASM') were not important indicated by the low values in permutation importance (Figure 3.4).

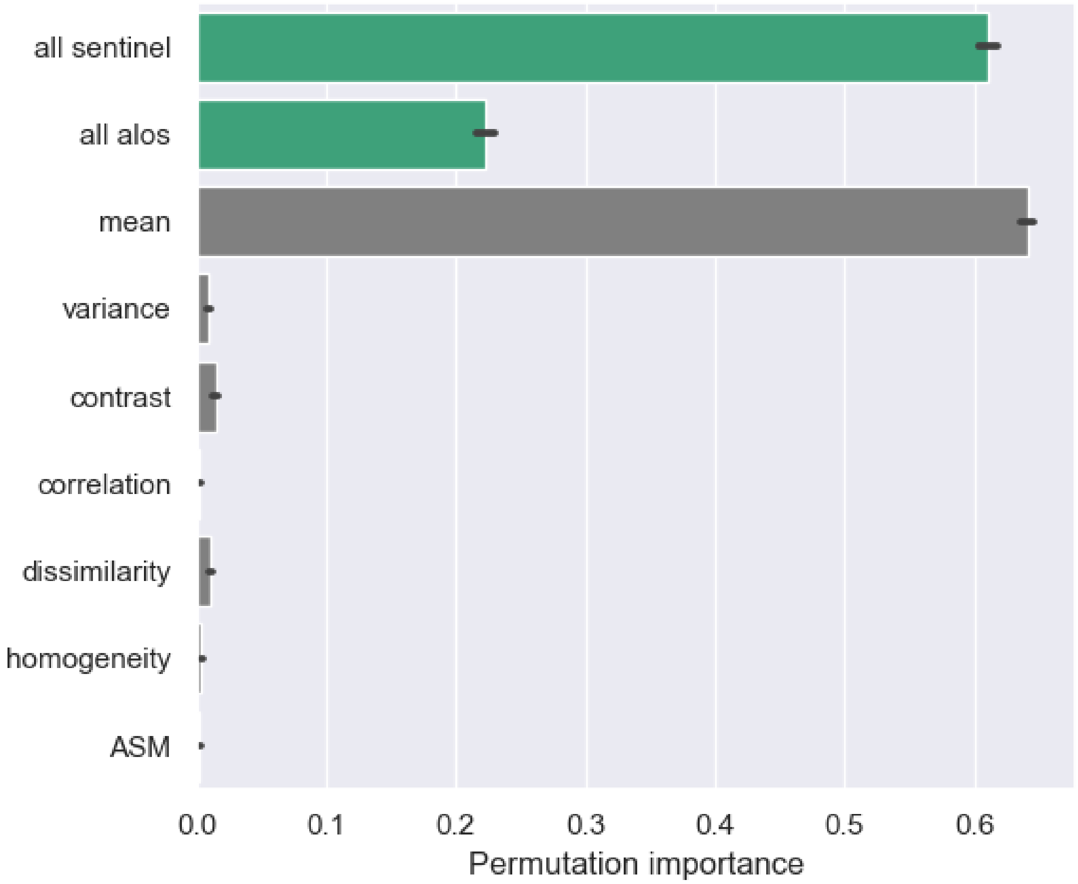

Figure 3.4. Permutation importance based on permutation of different aggregated input variables corresponding to specific sensors (green) and texture measures (grey).

3.4.4. VALIDATION OF THE AGB RANDOM FOREST MODEL INSIDE VS. OUTSIDE THE LIDAR SURVEY AREA

AGB showed a much higher fit (R^2 = 0.49) and a much lower error (relative RMSE = 24.6%) inside the LiDAR survey extent compared to outside the LiDAR survey area (R^2 = 0.17 and relative RMSE = 39.3%) (Figure 3.5). Importantly, the uncertainty estimates appear to be robust as estimates for all plots inside the LiDAR survey area and 94% of plots outside of the LiDAR survey fell under the 95% confidence intervals for AGB_{Field} and $AGB_{satellite}$. Outside the LiDAR survey extent there is one plot with unusually large trees and exceptionally high AGB_{field} (>300 Mg ha^{-1}), considerably higher than any of the other plots in the inventory (Figure 3.5).

Excluding this plot leads to a significant improvement in the fit outside of the LiDAR area (R^2 = 0.22, relative RMSE = 36%).

The validation analysis to compare the AGB maps with previous studies revealed that the RMSE and %RMSE obtained in this study were the lowest compared to the other maps (RMSE= 42.5 Mg ha-1 and %RMSE = 35.0 in this study, RMSE= 51.2 Mg ha-1 and %RMSE = 42.0 for Santoro et al (2018), RMSE= 57.5 Mg ha-1 and %RMSE = 47.0 for Cartus et al., (2016) and RMSE= 90.59 Mg ha-1 and %RMSE = 90 in that of Rodriguez-Veiga et al (2014)) (Figure 3.6).

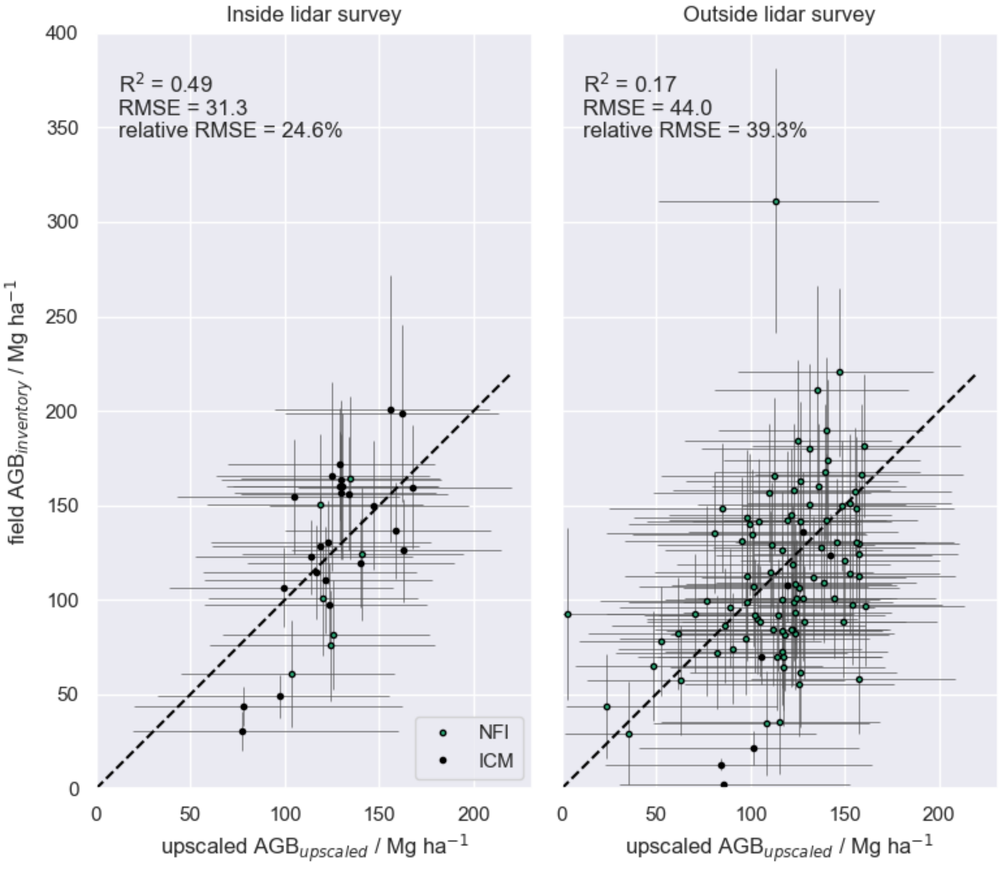

Figure 3.5. Regression lines of the validation of the upscaled AGB against field inventory data inside and outside the LiDAR survey area. Points represent an aggregate of four 400 m^2 plots (1600 m^2), uncertainty is shown as vertical and horizontal lines.

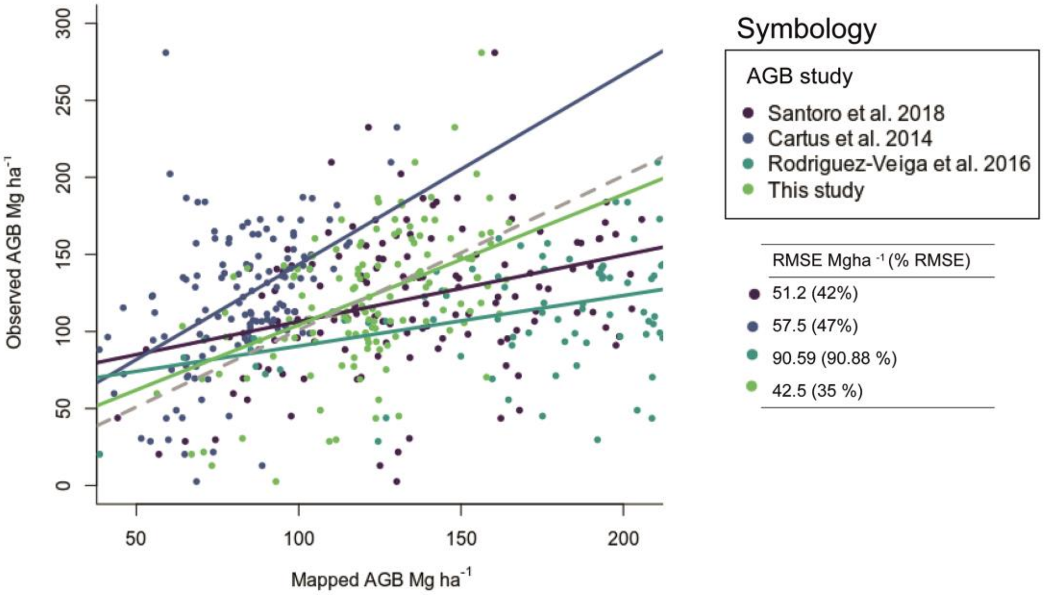

Figure 3.6. Comparison of observed AGB (obtained with field data used for validation)) and predicted AGB values (mapped AGB of different studies). The predicted values were obtained from Santoro et al., (2018), Rodriguez-Veiga et al., (2016), and Cartus et al., (2014). Solid lines indicate the regression between observed and predicted AGB, while dashed gray line shows a 1:1 relationship.

3.4.5. SPATIAL DISTRIBUTION OF AGB AND ITS UNCERTAINTY IN THE STUDY AREA

The spatial distribution of AGB (Figure 3.7) indicates that the higher biomass areas are located in the north-east portion of the window, coinciding with the distribution of the state reserve Reserva Estatal Biocultural del Puuc. Lower biomass areas are distributed around non-forest urban or agricultural areas, where forests are likely to be more degraded. The largest uncertainties are associated to areas with intermediate ranges (50 – 75 Mg ha^{-1}) of AGB.

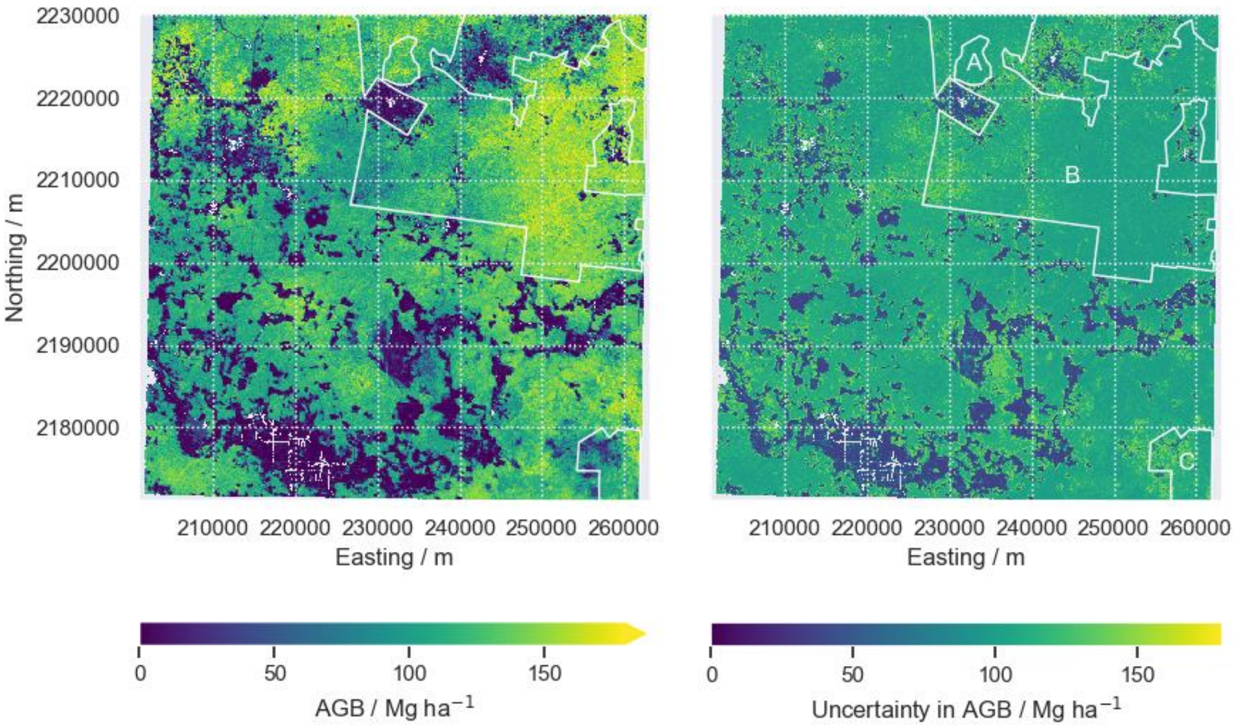

Figure 3.7. Spatial distribution of AGB (left pane) and its uncertainty (right pane) in the study area. Grid lines are spaced 10 km. Letters correspond to the location of protected areas within the study landscape: A) Reserva Biocultural Kaxil Kiuic, B) Reserva Estatal Biocultural del Puuc C) National protected area Bala'an K'aax.

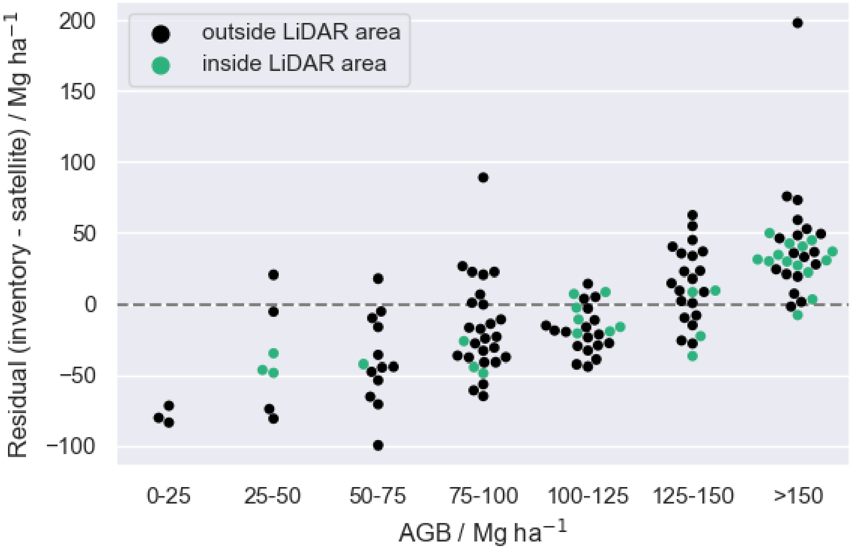

Figure 3.8. Residuals from field calculated AGB (inventory) - upscaled AGB (satellite) in Mg ha –1 distributed by categories of AGB.

Land management appears to have a significant effect on forest AGB stocks (Table 3.1, Table 3.2). The highest AGB densities by management class were located in the protected reserves of Kaxil Kiuic and Reserva Biocultural Del Puuc. Conversely, the small portion of the Bala’an Kaax reserve contained within our study area showed similar AGB to unprotected forest.

Table 3.1. Mean AGB and confidence intervals (CI) [Mg ha -1] for protected areas and areas without protection in the Kiuic area.

Management condition	Site	AGB	CI
Protected	Kaxil Kiuic	129.14	125 - 134
	Reserva Estatal Biocultural del Puuc	126.13	122 - 132
	Bala'an Kaax	100.64	97 - 104
Without protection	Restoration	106.63	103 - 110
	Production	99.23	96 - 103

Moreover, we found greater areas of high biomass and smaller areas of low AGB in protected areas. Forest areas suitable for production and restoration showed large areas of both low and high AGB.

Table 3.2. Summary of the area occupied by different AGB classes for different management conditions, with 95 confidence intervals provided in parentheses. Area in size classes is expressed as percentage relative to total area (last column).

AGB class (Mg ha^{-1})	Area by AGB Class (%) 0-25	25-50	50-75	75-100	100-125	125-150	>150	Total Area (km^2)
Kaxil Kiuic (protected)	0.2 (0.0/0.3)	1.0 (0.5/1.6)	4.5 (3.2/5.8)	11.8 (9.5/14.0)	26.5 (23.1/29.7)	30.3 (27.8/32.6)	25.7 (20.8/32.3)	18.5
Reserva Estatal Biocultural Del Puuc (protected)	2.3 (2.0/2.6)	3.1 (2.6/3.5)	5.3 (4.5/6.0)	10.6 (9.2/11.9)	22.1 (19.1/24.7)	27.4 (25.1/28.9)	28.7 (23.8/35.7)	697.0
Bala'an kaax (protected)	7.2 (5.9/8.3)	9.4 (8.3/10.4)	10.5 (9.3/11.7)	15.2 (12.7/16.7)	25.0 (23.3/26.9)	20.0 (18.5/21.8)	12.1 (9.9/14.9)	53.3
Production forest	10.2 (9.6/10.7)	6.6 (6.1/7.1)	8.0 (7.1/8.8)	13.5 (12.1/14.5)	24.2 (22.5/25.5)	21.3 (20.1/22.9)	13.2 (11.0/16.5)	2154.2
Restoration forest	7.6 (6.8/8.2)	6.9 (6.2/7.5)	8.1 (7.2/8.8)	12.8 (11.4/14.0)	23.1 (21.0/24.9)	22.4 (21.3/23.7)	17.6 (14.7/21.7)	216.8

Comparing the distributions of the median AGB estimates from the Monte Carlo upscaling process there are marked differences between the protected and unprotected areas (Figure 3.9). Kaxil Kiuic and Reserva Estatal Biocultural del Puuc have higher AGB, with very low frequencies with AGB < 100 Mg ha^{-1}. These distributions contrast with the potential production and restoration areas, which both show much lower frequencies in the upper end of the AGB distributions, and a long tail of AGB < 100 Mg ha^{-1}. This is consistent with these areas of forest being subject to high levels of disturbance (Williams et al., 2013). The portion of the Reserva Bala'an Kaax within the study area has a similar distribution of AGB to forest production and restoration areas, suggesting this area of the reserve may have been subjected to similar degradation pressures.

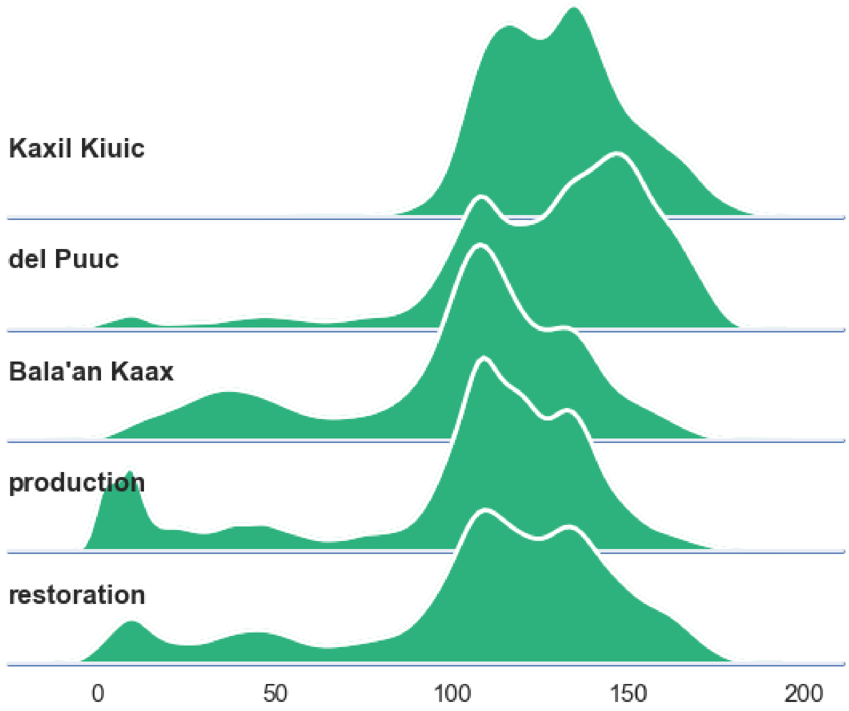

Figure 3.9. Kernel-Density Estimation (KDE) plots showing the frequency distribution of AGB [Mg ha -1] in protected areas (Kaxil Kiuic, Reserva Estatal Biocultual del Puuc 'del Puuc', Bala'an Kaax) vs unprotected areas (areas designated for restoration and production), based on the median AGB per-pixel from the Monte Carlo upscaling process.

3.5. DISCUSSION

This study provides a spatially explicit estimation of AGB and its uncertainty in a semi-deciduous tropical dry forest of Yucatan using LiDAR data and a combination of information from passive and active sensors. As a first step, LiDAR data was used to estimate AGB using field plot information. The effectiveness of using LiDAR-derived AGB for upscaling plot-based estimations to continuous landscape level estimations has been demonstrated in various forests worldwide (Mascaro et al., 2011, Wulder et al., 2012, Asner et al., 2018). Random Forest models using information from a combination of Sentinel 2 and ALOS PALSAR were able to upscale AGB estimates based on a locally calibrated map of AGB based on LiDAR top-of-canopy height. Several studies have shown that tropical forest AGB can be estimated using ALOS PALSAR backscatter (Mitchard et al., 2013; Hernández-Stefanoni et al., 2020) and Sentinel 2 reflectance (Pandit et al., 2019), however, the combination of both sensors has been little explored (but see Vafaei et al., 2018). To assess the improvement on the precision of estimates by combining active and passive sensors we tested each sensor individually then produced a combined model using information from both sensors. Our results suggest that the estimation of AGB in the semi deciduous tropical forest of Yucatan can be improved through a combination of ALOS PALSAR backscatter information and Sentinel 2 reflectance and texture variables, increasing the variance explained by the best single sensor model from 66% to 70% and reducing the RMSE from 29.5% to 27.8%. This improvement in AGB estimation is similar to the results found in Vafaei et al., (2018) in a subtropical forest in Iran also combining ALOS PALSAR backscatter and Sentinel 2. Furthermore, we tested the contribution of each sensor to explain AGB and found that Sentinel 2 on its own explained a greater amount of variation of AGB, compared to ALOS PALSAR, although the majority of the explained variation was shared between both sensors. One of the main caveats in the sensor combination approach is the difference in spatial resolution between the ALOS PALSAR backscatter (25 m) and Sentinel 2 (10 m). It is possible that this difference has an impact on the amount of variability that can be captured by each sensor at the plot level. Given its higher spatial resolution, Sentinel 2 could capture a greater range of variability of AGB within the plots than ALOS PALSAR. Coarser resolutions may not reflect the variability of structure as they contain averaged information from varying heights and may include reflectance from non-forest areas or canopy gaps within the same pixel (Lu, 2006).

We tested the use texture information as a way to quantify the variability of reflectance and backscatter within the plots and related this to LiDAR-estimated AGB. In this case, the upscaled models were principally reliant on the mean with limited additional contributions to the predictive power added by texture information. Other studies that have used texture information from ALOS PALSAR backscatter (Thapa et al., 2015; Hernández-Stefanoni et al., 2020) and Sentinel 2 reflectance (Pandit et al., 2019) have found large improvements in estimations of AGB by capturing the spatial variability and minimizing sensor saturation. To test the effect of spatial resolution in the upscaling process we compared models with different resolutions and found that an upscaling resolution of 100 m increased the fit of the best model by 8% and decreased the errors by 3.9%, compared to upscaling at 20 m resolution (Supplement 2). This suggests that the aggregation of information prior to upscaling might improve models and reduce the overall errors. However, as there is a trade-off between the information lost and the reduction of error when aggregating information (Carmel, 2004), we chose not to aggregate further than 100 m, as this would reduce the spatial information gained from Sentinel’s 10 m resolution. The comparison with the work of Santoro et al., (2018), Rodriguez-Veiga et al., (2016), and Cartus et al., 2014 suggests that by performing a bias-corrected upscaling procedure we were able to reduce the error, thus, improving upon previous AGB mapping efforts in the dry forests of Yucatan. Such procedures can be used to produce AGB maps to inform regional and national strategies for reducing greenhouse gas emissions such as REDD+.

By propagating errors through each step of the upscaling process and applying a spatially independent validation procedure, we were able to produce a robust estimation of errors (94% of field AGB estimates for aggregated plot clusters overlap within the estimated 95% confidence interval outside of the LiDAR survey area). While the error propagation estimates appear to be robust, it is evident from the distribution of residuals (Figure 3.8) that there remains a trend in the residuals highlighting a tendency to underpredict the AGB of higher biomass field plots and overpredict the AGB at low biomass field plots. This suggests that the bootstrap bias correction was not sufficient to fully remove the bias in the random forest models, possibly a consequence of spatial correlations. Given that degradation and deforestation act to lower AGB, this outstanding source bias will likely lead to conservative estimates of the AGB differences between protected and unprotected forests, and therefore conservative estimates of restoration potential. This result suggests an improvement of previous efforts to estimate AGB in semi-deciduous dry forests of the Yucatan Peninsula using active sensors such as ALOS PALSAR (Hernéndez-Stefanoni et al., 2020) and national scale efforts (Cartus et al., 2014; Rodríguez-Veiga et al., 2016). Previous attempts to map AGB across Mexico have found a wide range of AGB values in the Yucatan Peninsula reaching 150 Mg ha^{-1} (Hernández-Stefanoni et al., 2020; Rodríguez-Veiga et a., 2016; Cartus et al., 2014) and greatest uncertainties in the lower end of the AGB distribution (Rodríguez-Veiga et al., 2016). The spatial distribution of uncertainty showed that the largest uncertainties were associated to the middle range of AGB distribution (Figure 3.7 and 3.8) and it is derived from the underrepresentation of areas with this range of AGB values ranging between 25 and 75 Mg ha^{-1} in the calibration data (Figure 3.8). However, in accordance with Hernández-Stefanoni et al., (2020), estimates were also found to be constrained by the range of AGB variation captured by LiDAR data available across the calibration landscape. In particular, the predictability of the upper bounds of the biomass ranges was severely affected by the lack of LiDAR coverage in the very high biomass forest (> 200 Mg ha $^{-1}$). Therefore, areas with high biomass, located in the north-east of the window area, in the protected area of “Reserva Estatal Biocultural del Puuc”, are underrepresented in the LiDAR survey with only a portion of the area, corresponding to the location of “Reserva Biocultural Kaxil Kiuic”, represented by both field and LiDAR data (Figure 3.1). To estimate AGB in tropical forests where forest protection areas and areas where disturbances such as slash-and-burn agriculture shape the spatial variability of forest AGB, the accuracy of estimates will depend on the distribution of LiDAR and field data available across all the possible ranges of AGB. As it has been previously cautioned, the range of variability in AGB captured by both the LiDAR data and the forest inventory constrained the next stages of the analysis (Hernández-Stefanoni et al., 2020), limiting the predictability in the lower and upper ranges of our estimated AGB. In order to reduce the uncertainty in AGB mapping, future upscaling efforts could aim for a more thoroughly distributed airborne sampling campaign that better characterizes the full range of AGB values in the landscape. Moreover, uncertainty in the upper and lower ranges of AGB was reduced when combining information from both sensors, suggesting that the combination of these sensors is an effective way to improve AGB mapping.

Within the study region, larger areas with high biomass were found in the protected areas of “Reserva Estatal Biocultural del Puuc” and “Reserva Biocultural Kaxil Kiuic”, which were created for the conservation of forests and their environmental services (Table 3.2). In particular, the Kaxil Kiuic protected area shows a more symmetric distribution with the highest mean AGB (Figure 3.9; Table 3.2) indicating a large proportion of this area may be approaching a steady state condition (Williams et al., 2013). However, several other low impact activities such as extraction of woody species for fuel, and agricultural and pastures for cattle ranching take place inside Reserva Estatal Biocultural del Puuc. This is reflected in the tail of low AGB values in this area, although significantly less prevalent than outside the forest reserves. The study region has a long history of land use, mainly for slash-and-burn agriculture, also practiced presently in the area (Ellis et al., 2017). The effect of the more recent repeated disturbance is reflected in the AGB distributions of the production forest, which have skewed AGB distributions with a long tail of low AGB (Figure 3.0). Critically, regions allocated for restoration have large areas with low AGB (Table 3.2) and similar AGB distributions to existing production forest (Figure 3.9). Therefore, while there is potential for substantial gains in aboveground carbon stocks through restoration, whether these gains are realized is likely to be dependent on these restored forests being protected and allowed to develop into high biomass old-growth systems (Lewis et al., 2019; Chazdon et al., 2016).

3.6. CONCLUSIONS

LiDAR data proved a useful upscaling tool for calibrating and validating satellite models of AGB, however, the reliability of these estimates is constrained by the degree to which the sampled areas represent the range of AGB values found in the whole landscape, to avoid potential biases when upscaling outside the training area. The sensitivity to within-forest variation in AGB was more limited particularly in the upper end of the AGB range, thus limiting our ability to predict AGB in high biomass forest areas.

We found that the information from active (ALOS PALSAR backscatter) and passive (Sentinel-2 reflectance) sensors can be combined to improve spatially explicit estimations of AGB in semi-deciduous tropical forest. However, Sentinel-2 explained a higher proportion of the variance in the combined model and performs better than ALOS PALSAR when considered separately. We believe the methods described in this study can be used to improve estimations of AGB and its uncertainty in tropical forests. Using a combination of LiDAR and satellite data, we upscaled LiDAR estimates of AGB across a landscape of semi-deciduous forest in the Yucatan peninsula to gain insights on the distribution of AGB in different categories of forest protection. The frequency distributions of AGB obtained from our maps highlighted the benefits of protected areas for maintaining forest carbon stocks. On the other hand, a significantly greater portion of the areas designated for restoration currently have low AGB, comparable to the distribution of AGB in existing production forest. The similarity in the distributions of these categories suggests areas of restoration should be effectively protected for carbon sequestration, biodiversity conservation and for other important ecosystem services, which can take several decades to reach old-growth forest values.

We believe the information obtained can provide insights on the state of the AGB stock in different management or protection categories in the region and thus aid conservation, restoration, and sustainable management policies in the semi-deciduous forests of the Yucatan Peninsula.

Availability of data and materials

The ALOS PALSAR data used in this study was downloaded from (https://www.eorc.jaxa.jp/ALOS/en/top/obs_top.htm). The LiDAR data can be accessed at (https://gliht.gsfc.nasa.gov/). Data from national forest inventory in Mexico can be obtained by request to CONAFOR (Comisión Nacional Forestal, https://www.gob.mx/conafor).

CAPÍTULO IV

4. DISCUSIÓN, CONCLUSIONES GENERALES Y PERSPECTIVAS

4.1. DISCUSIÓN

El objetivo general de este trabajo fue evaluar la aportación del uso de información espacialmente explícita de la edad de sucesión y obtener estimaciones espacialmente explícitas de la biomasa aérea de bosques tropicales secos mediante dos estrategias que permitieron reducir los errores de estimación y la incertidumbre en las estimaciones de biomasa aérea de bosques tropicales secos de la Península de Yucatán. La primera estrategia consiste en estimar la biomasa aérea a partir de la relación entre la biomasa y la edad de sucesión, mediante estimaciones espacialmente explícitas del año de la última pérdida de cobertura forestal.

Las estimaciones previas de la biomasa aérea de los bosques de la Península de Yucatán tienden a sobreestimar la biomasa de árboles pequeños (Hernández-Stefanoni et al., 2020), lo cual tiene un impacto en las estimaciones de biomasa en bosques con edades de sucesión tempranas. A partir de la información espacial del tiempo de pérdida de cobertura forestal y la relación entre biomasa y la edad obtenida de cronosecuencias, fue posible reducir la sobreestimación de la biomasa de bosques en edades tempranas. Es posible estimar la edad de los bosques tropicales secos de la península de Yucatán a partir del último disturbio por medio de las series de tiempo de imágenes Landsat cuando estos disturbios antrópicos causan la pérdida de cobertura forestal, dado que se encuentran sujetos a grandes presiones antrópicas que moldean el paisaje (Ellis et al., 2017). Sin embargo, la precisión del modelo harmónico utilizado en este trabajo se ve afectada por la variabilidad de la dinámica intra-anual de la vegetación, ocasionada por la intensidad y duración de la estación de sequía. En este sentido, el modelo harmónico de BFast permitió estimar la pérdida de vegetación de manera más precisa en la selva mediana subperennifolia donde la estabilidad del clima es mayor, y encontramos una subestimación del área de pérdida de cobertura para las selvas más secas (bosque tropical caducifolio y subcaducifolio) registrada en los valores bajos de la precisión del productor para estos bosques mediante series de tiempo de NDVI (Cuadro 2.1). Por otra parte, al calcular el área corregida de pérdida (Card 1982) se encontró que las estimaciones de pérdida de cobertura forestal se encuentran dentro de los límites de confianza (Cuadro 2.3).

Estudios previos que han estimado la deforestación en los bosques de la Península de Yucatán han encontrado igualmente una mayor cantidad de pérdida de cobertura forestal en las selvas medianas y bajas del norte y centro de la Península de Yucatán (Ellis et al., 2017). Asimismo, la subestimación del área de cambio de “bosque” a “no bosque” por medio del análisis de series de tiempo es común (Oloffsson et al., 2013; 2014) y puede provenir de una combinación de factores, tales como el índice utilizado, la cantidad de observaciones válidas (pixeles sin nubes), así como de características propias del sitio como la tasa de crecimiento después de un disturbio, la cual tiende a ser menor en bosques tropicales más secos que en los húmedos (Smith et al., 2019; DeVries et al., 2015). Esto podría explicar las diferencias en la precisión entre sitios con diferentes condiciones y usos de suelo.

Por otra parte, la comparación de la biomasa estimada considerando la edad del bosque como variable explicativa con estimaciones de otros trabajos de percepción remota que no incorporan una medida espacialmente explícita de la edad (Hernández-Stefanoni et al., 2020, Rodríguez-Veiga et al., 2018, Cartus et al., 2014), y datos de referencia de campo, mostró que las estimaciones por medio de la edad son más bajas, y más cercanas a los valores de biomasa obtenidos de los datos de campo (Cuadro 2.3, Figura 2.6). Este resultado sugiere que el incorporar información de la edad potencialmente podría reducir la sobreestimación de biomasa aérea comúnmente observada para bosques tropicales jóvenes (Hernández-Stefanoni et al., 2020, Rodríguez-Veiga et al., 2018, Cartus et al., 2014) al incorporar la medida en la cual los bosques recuperan biomasa a lo largo del tiempo. La reducción de la sobreestimación de la biomasa de estos bosques es importante debido a que en bosques secundarios jóvenes se encuentra el mayor potencial de secuestro de carbono (Cook-Patton et al., 2020), sin embargo, debido al incremento en la pérdida de cobertura forestal, esta mitigación potencial puede verse reducida de manera importante.

En el caso particular de los bosques de Yucatán, encontramos que los bosques más secos del centro y noreste de la Península también presentan una mayor extensión de terrenos dedicados a agricultura de roza tumba y quema, mientras que en el sureste, una gran extensión de los bosques es manejada comunitariamente (Ellis et al., 2017). Consecuentemente, encontramos la menor extensión de pérdida de bosque, y una mayor extensión de bosque mayor a 20 años, en los bosques subperennifolios que crecen en el sureste, mientras que en los bosques caducifolio y subcaducifolio (centro y noreste), encontramos mayores extensiones de bosques menores a 20 años. Este resultado concuerda con trabajos previos que indican que la extracción selectiva y el manejo comunitario ayudan a conservar los almacenes de carbono en los bosques tropicales (Porter-Bolland et al., 2012), contribuyendo a conservar los almacenes de carbono en la biomasa de las selvas subperennifolias. Por otra parte, en la selva baja caducifolia y la selva mediana subcaducifolia, la regeneración natural de los bosques jóvenes podría representar un potencial de secuestro de carbono cuando el período de recuperación de la vegetación o barbecho es lo suficientemente extenso para permitir la recuperación adecuada de los suelos, así como la estructura y funciones ecosistémicas del bosque (Chazdon 2014).

Por otra parte, en un bosque tropical subcaducifolio, la combinación de ALOS Palsar (sensor activo) y Sentinel 2A (sensor pasivo) produjo estimaciones precisas de biomasa aérea por medio del escalamiento de datos LiDAR en un modelo de Random Forest. Este resultado sugiere que la información de estos sensores es hasta cierto punto complementaria. Estudios previos que han estimado la distribución espacial de la biomasa aérea de bosques por medio de sensores pasivos (Pandit et al., 2015; Lu et al., 2005) y otros por medio de sensores activos (Mermoz et al., 2015; Thapa et al., 2015; Mitchard et al., 2009) han resaltado las limitaciones individuales del uso de cada tipo de sensor por separado.

Por una parte, los sensores pasivos son afectados por condiciones ambientales como la presencia de nubes y humo, lo cual es común en los trópicos (Asner et al., 2001) y únicamente proporcionan información de la parte superior del dosel, por lo que se saturan en bosques con estructuras más complejas (Joshi et al., 2015). Por su parte, los sensores activos como ALOS PALSAR, son afectados por la topografía, el contenido de agua en la vegetación y se satura en bosques con grandes cantidades de biomasa. La combinación de sensores activos y pasivos permite superar estas limitaciones individuales y aprovechar las ventajas del aumento del tamaño de muestra mediante el escalamiento de LiDAR. Esta combinación ha sido menos explorada, sin embargo, produce estimaciones más precisas y con menor error consistentemente (Bispo et al., 2020; Vafaei et al., 2017).

Ortiz-Reyes et al., (2021) realizaron el escalamiento datos LiDAR a una combinación de índices e información espectral obtenidas de Landsat y variables climáticas en selvas medianas subcaducifolias y subperennifolias de la Península de Yucatán, y encontraron que la información espectral de Landsat en conjunto con información de precipitación puede producir estimaciones precisas de biomasa aérea para estos bosques. De igual manera, es importante señalar que el límite superior de las estimaciones de biomasa aérea en bosques secos usando sensores remotos concuerda con otros trabajos que han producido estimaciones espacialmente explícitas para bosques secos (Hernández-Stefanoni et al., 2020; Rodríguez-Veiga et al., 2016; Cartus et al., 2014) (Figura 3.3).

Es importante tomar en cuenta que las estimaciones de biomasa aérea a nivel regional por medio del escalamiento inicial de datos de campo a áreas censadas con LiDAR y posteriormente a escala regional por medio de múltiples sensores, requieren de protocolos robustos para la propagación del error debido a que los datos LiDAR con frecuencia no se encuentran disponibles de manera continua en todo el paisaje (Ploton et al., 2020). Este estudio plantea una metodología para realizar la propagación del error de manera consistente y robusta a través de las diferentes etapas del escalamiento. En este sentido, el error se propagó a partir de los árboles individuales, hasta llegar a la escala regional. Los resultados apuntan a una mayor incertidumbre en las categorías de biomasa aérea donde se encuentra la menor cantidad de datos de referencia, de manera particular en las categorías de biomasa intermedias y bajas (Figura 3.7). De igual manera, el límite superior de la estimación se ve severamente afectado por la ausencia de datos de entrenamiento en zonas con biomasa superior a 150 Mg ha $^{-1}$ en la calibración (Figura 3.7). Posteriormente, se realizó una validación con datos de campo dentro y fuera del área de LiDAR con el fin de contar con una validación completamente independiente del área de calibración, en la cual las estimaciones del 94% de las parcelas de validación cayeron dentro de los límites de confianza.

De manera conjunta, los resultados de este trabajo sugieren que, al incluir información de la edad de sucesión, e incluir información de sensores pasivos y activos es posible superar las limitaciones discutidas en trabajos anteriores que estiman la biomasa aérea de bosques tropicales, tales como la subestimación del aporte de la biomasa aérea de individuos de tallas pequeñas, y a reducir y realizar una propagación efectiva del error de las estimaciones de biomasa en bosques tropicales secos de la península de Yucatán (Hernández-Stefanoni et al., 2020; Rodríguez-Veiga et al., 2016; Cartus et al., 2014). Sin embargo, es importante mencionar que existe información complementaria que podría reducir la incertidumbre de las estimaciones de biomasa aérea al incluir la variabilidad explicada por factores ecológicos que afecten el crecimiento de los bosques como el déficit climático de agua (Hernández-Stefanoni et al., 2020), la precipitación (Ortiz-Reyes et al., 2021), la variación en la topografía (Asner et al., 2018; Mascaro et al., 2014), propiedades del suelo como tipo y textura (Mascaro et al., 2011), e incluso el contexto espacial o posición geográfica (Mascaro et al., 2014). Asimismo, la representación de las diferentes categorías de biomasa que existen en el paisaje en la muestra de LiDAR y en los datos de campo tienen un gran impacto en la precisión de las estimaciones de biomasa aérea de estos bosques (Hernández-Stefanoni et al., 2021).

A partir de las estimaciones obtenidas, se hicieron comparaciones entre la distribución de frecuencias de los valores de biomasa aérea entre diferentes categorías de protección (áreas dedicadas a la conservación, y áreas aptas para la producción o para la restauración) para evaluar el estado de los almacenes de biomasa aérea entre diferentes estrategias de conservación y manejo. Se obtuvo que existen indicios de eventos de pérdida de cobertura forestal dentro de áreas protegidas, como demuestra la presencia de altas frecuencias en los valores de categorías bajas de la Reserva Estatal Biocultural del Puuc, que permite el uso y presenta varias formas de tenencia de la tierra. Por su parte la distribución de frecuencias del área protegida Reserva Biocultural Kaxil Kiuic, una reserva privada de menor tamaño con vocación exclusiva para la investigación y la conservación muestra que la conservación efectiva de las áreas de bosque puede ayudar a conservar los almacenes de biomasa aérea (Figura 3.9). Las distribuciones de frecuencias de las categorías de áreas con aptitud para la producción forestal y zonas aptas para la restauración (Figura 3.9) y el área estimada que ocupan de acuerdo con categorías de tamaño (Cuadro 3.2), sugieren que estas zonas presentan potencial para la mitigación de las emisiones por deforestación si son conservadas efectivamente. En particular, las áreas designadas como potenciales (o con vocación) para la restauración forestal y áreas de producción fueron designadas en la Zonificación Forestal del Sistema Nacional de Información y Gestión Forestal (SNIGF) donde se agrupan y ordenan los terrenos forestales de acuerdo con sus funciones ecosistémicas, socioeconómicas y restauradoras para contribuir al desarrollo forestal sustentable y como parte de una estrategia para el adecuado manejo del paisaje. Para áreas de producción se incluyen zonas con condiciones de vegetación y suelo apropiadas para la producción maderable y no maderable determinadas por medio de la Carta de uso de Suelo y Vegetación Serie IV escala 1:250,000, y datos del INFyS (DOF, 2011). En estas se incluyen áreas de producción alta, media y baja, terrenos con vegetación forestal en zonas áridas, terrenos adecuados para realizar forestaciones (donde las condiciones topográficas y edafológicas son adecuadas para el establecimiento de vegetación forestal) y terrenos preferentemente forestales (donde se incluyen terrenos de baja o degradación nula). Igual que las áreas de producción, las áreas de restauración incluyen terrenos forestales con diversos niveles de degradación y terrenos sometidos a tratamientos de recuperación forestal. Estas categorías implican diferencias en el contenido de biomasa y/o carbono en las áreas, lo cual se ve reflejado en la distribución de los valores de biomasa aérea presentada en la Figura 3.9.

Se ha estimado previamente que la regeneración natural de los bosques tropicales secundarios jóvenes representa un gran potencial para la captura de carbono (Cook-Patton et al., 2020; Lewis et al., 2019). Los resultados de este trabajo demuestran que la Península de Yucatán posee áreas con un gran potencial para la captura de carbono al presentar grandes extensiones de bosques tropicales caducifolios y subcaducifolios menores a 20 años, como lo sugieren los resultados del capítulo 2 de este trabajo, y por medio de la conservación de los bosques dentro de áreas protegidas, de acuerdo con los resultados del capítulo 3. Asimismo, también se encontró una gran extensión de bosques con edades mayores a 20 años, los cuales son de gran importancia para la conservación de los almacenes de carbono almacenado en la biomasa aérea. De manera importante, se resalta que el potencial de mitigación de emisiones de CO_2 por deforestación de los bosques secos de la Península de Yucatán podrá ser aprovechado si las áreas con bosques jóvenes que se encuentran dentro de las áreas designadas para la restauración son conservadas efectivamente, permitiendo su regeneración.

4.2. CONCLUSIONES GENERALES

En este trabajo se demuestra el incremento en la precisión y la disminución de la sobreestimación de estimaciones espacialmente explícitas de la biomasa aérea de los bosques tropicales secos mediante dos estrategias diferentes: a partir de la estimación de la edad sucesional del bosque y mediante la combinación de sensores pasivos y activos de percepción remota. De acuerdo con los resultados obtenidos de este trabajo, se pueden hacer consideraciones sobre el uso de estas herramientas para la estimación de la biomasa aérea en bosques tropicales y adicionalmente, se pueden derivar consideraciones importantes para la conservación y el manejo adecuado de los bosques tropicales secos de la Península de Yucatán.

La estacionalidad y el uso de suelo tienen un impacto en la diferencia de precisión de las estimaciones de la edad de sucesión mediante el análisis de series de tiempo. En este sentido, fue posible detectar la pérdida de cobertura forestal con una mayor precisión en el sitio de bosque subperennifolio donde hay una mayor precipitación, menor estacionalidad y prácticas de manejo comunitario de bajo impacto. Por el contrario, en los bosques más secos, de mayor estacionalidad, grandes proporciones de cambios no fueron detectadas, por lo que se subestimó la magnitud de la deforestación. Adicionalmente, nuestras estimaciones demuestran mayores áreas de pérdida y una clara tendencia de incremento en la pérdida de cobertura forestal en los bosques más secos, lo cual indica que potencialmente pueden estar más amenazados por el cambio de uso de suelo, pero a la vez también representan el mayor potencial para reducir las emisiones por deforestación en la Península, si se permite o fomenta su regeneración.

Mediante la información de la relación entre la edad de sucesión y la biomasa aérea, es posible estimar la biomasa aérea de los bosques menores a 20 años y potencialmente reducir la sobreestimación de las estimaciones de biomasa aérea por medio de percepción remota, que informen estrategias de mitigación y reducción de las emisiones de carbono por deforestación y degradación.

Al realizar la combinación de sensores pasivos y activos, es posible mejorar la precisión de las estimaciones de biomasa aérea por medio del escalamiento de datos LiDAR, sin embargo, la importancia de los datos de campo que representen todo el rango de variabilidad es fundamental para reducir la incertidumbre en las estimaciones.

Existen grandes áreas designadas para la restauración en la Península de Yucatán, estas áreas presentan potencial para la regeneración del bosque, y por lo tanto para aumentar el secuestro de carbono, sin embargo, para incrementar y mantener los almacenes de carbono en la biomasa aérea en los bosques secos es necesario establecer y vigilar áreas protegidas dedicadas exclusivamente a la conservación. Esta información puede ser utilizada para derivar estrategias y evaluar la efectividad de programas actuales de conservación y manejo en bosques tropicales secos.

4.3. PERSPECTIVAS

Aunque los resultados de este trabajo representan un avance en la reducción de la incertidumbre y la propagación del error en las estimaciones de biomasa aérea en bosques tropicales secos mediante métodos de modelación y datos de percepción remota, prevalece la necesidad de incorporar variables ecológicas relacionadas con el clima, los suelos o con la distribución de nutrientes, en escalas apropiadas para las zonas de estudio que permitan captar los aspectos de los factores de los que depende la distribución espacial de la biomasa aérea en los bosques secos.

De igual manera, se resalta la importancia de la calidad de los datos de referencia obtenidos en campo, por ejemplo, la estimación de biomasa por medio de datos de campo podría mejorar al obtener ecuaciones alométricas específicas y desarrolladas con parámetros locales. Es importante señalar que existen pocos estudios que monitoreen la dinámica de la vegetación en diferentes tipos de bosques, y/o bajo diferentes historias de uso de suelo previo y que los estudios de la dinámica de carbono necesitan ser validados con datos obtenidos de inventarios de campo para proveer medidas de la precisión y el alcance de sus resultados.

Los bosques tropicales secos de la Península de Yucatán se encuentran severamente amenazados tanto por presiones antrópicas como naturales, y es importante la estimación de atributos relativos a los almacenes de carbono que se encuentran en ellos, como la biomasa aérea en el presente. Sin embargo, son necesarios estudios que permitan proyectar las estimaciones de los almacenes de biomasa en los bosques secos hacia el futuro en diferentes escenarios y que reflejen las posibles vías que puede tomar el cambio global.

BIBLIOGRAFÍA

Adhikari, H., Heiskanen, J., Siljander, M., Maeda, E., Heikinheimo, V., & K. E. Pellikka, P. (2017). Determinants of Aboveground Biomass across an Afromontane Landscape Mosaic in Kenya. *Remote Sensing*, *9*(8), 827. https://doi.org/10.3390/rs9080827

Allen, K., Dupuy, J. M., Gei, M. G., Hulshof, C., Medvigy, D., Pizano, C., Salgado-Negret, B., Smith, C. M., Trierweiler, A., Van Bloem, S. J., Waring, B. G., Xu, X., & Powers, J. S. (2017). Will seasonally dry tropical forests be sensitive or resistant to future changes in rainfall regimes? *Environmental Research Letters*, *12*(2), 023001. https://doi.org/10.1088/1748-9326/aa5968

Armenta-Montero, S., Ellis, E. A., Ellis, P. W., Manson, R. H., Lopez-Binnqüist, C., & Villaseñor Pérez, J. A. (2020). Carbon emissions from selective logging in the southern Yucatan Peninsula, Mexico. *Madera y Bosques*, *26*(1). https://doi.org/10.21829/myb.2020.2611891

Asner, G.P. (2001). Cloud cover in Landsat observations of the Brazilian Amazon. *International Journal of Remote Sensing*, *22*(18), 3855–3862.

Asner, G.P., & Mascaro, J. (2014). Mapping tropical forest carbon: Calibrating plot estimates to a simple LiDAR metric. *Remote Sens. Environ*, *140*, 614-624 10 1016 2013 09 023.

Asner, Gregory P., Brodrick, P. G., Philipson, C., Vaughn, N. R., Martin, R. E., Knapp, D. E., Heckler, J., Evans, L. J., Jucker, T., Goossens, B., Stark, D. J., Reynolds, G., Ong, R., Renneboog, N., Kugan, F., & Coomes, D. A. (2018). Mapped aboveground carbon stocks to advance forest conservation and recovery in Malaysian Borneo. *Biological Conservation*, *217*, 289–310. https://doi.org/10.1016/j.biocon.2017.10.020

Avitabile, V., Herold, M., Heuvelink, G. B. M., Lewis, S. L., Phillips, O. L., Asner, G. P., Armston, J., Ashton, P. S., Banin, L., Bayol, N., Berry, N. J., Boeckx, P., de Jong, B. H. J., DeVries, B., Girardin, C. A. J., Kearsley, E., Lindsell, J. A., Lopez-Gonzalez, G., Lucas, R., … Willcock, S. (2016). An integrated pan-tropical biomass map using multiple reference datasets. *Global Change Biology*, *22*(4), 1406–1420. https://doi.org/10.1111/gcb.13139

Baccini, A., Goetz, S. J., Walker, W. S., Laporte, N. T., Sun, M., Sulla-Menashe, D., Hackler, J., Beck, P. S. A., Dubayah, R., Friedl, M. A., Samanta, S., & Houghton, R. A. (2012). Estimated carbon dioxide emissions from tropical deforestation improved by carbon-density maps. *Nature Climate Change*, *2*(3), 182–185. https://doi.org/10.1038/nclimate1354

Baccini, A., Walker, W., Carvalho, L., Farina, M., Sulla-Menashe, D., & Houghton, R. A. (2017). Tropical forests are a net carbon source based on aboveground measurements of gain and loss. *Science*, *358*(6360), 230–234. https://doi.org/10.1126/science.aam5962

Baccini, Alessandro, & Asner, G. P. (2013). Improving pantropical forest carbon maps with airborne LiDAR sampling. *Carbon Management*, *4*(6), 591–600. https://doi.org/10.4155/cmt.13.66

Baskerville, G. L. (1972). Use of Logarithmic Regression in the Estimation of Plant Biomass. *Canadian Journal of Forest Research*, *2*, 49–53. https://doi.org/10.1139/x72-009

Bastin, J.-F., Finegold, Y., Garcia, C., Gellie, N., Lowe, A., Mollicone, D., Rezende, M., Routh, D., Sacande, M., Sparrow, B., Zohner, C. M., & Crowther, T. W. (2019). Response to Comments on “The global tree restoration potential.” *Science*, *366*(6463), eaay8108. https://doi.org/10.1126/science.aay8108

Becknell, J. M., & Powers, J. S. (2014a). Stand age and soils as drivers of plant functional traits and aboveground biomass in secondary tropical dry forest. *Canadian Journal of Forest Research*, *44*(6), 604–613. https://doi.org/10.1139/cjfr-2013-0331

Becknell, J. M., & Powers, J. S. (2014b). Stand age and soils as drivers of plant functional traits and aboveground biomass in secondary tropical dry forest. *Canadian Journal of Forest Research*, *44*(6), 604–613. https://doi.org/10.1139/cjfr-2013-0331

Bergstra, J., Yamins, D., & Cox, D. (2013). *Hyperopt: A Python Library for Optimizing the Hyperparameters of Machine Learning Algorithms*. 13–19. https://doi.org/10.25080/Majora-8b375195-003

Bhaskar, R. A., Mora, F., Martinez-Yrizar, F., Martinez-Ramos, A., M., & Balvanera, P. (2018). Response diversity and resilience to extreme events in tropical dry secondary forests. *Forest Ecology and Management*, *426*, 61–71.

Bispo, P. da C., Rodríguez-Veiga, P., Zimbres, B., do Couto de Miranda, S., Henrique Giusti Cezare, C., Fleming, S., Baldacchino, F., Louis, V., Rains, D., Garcia, M., Del Bon Espírito-Santo, F., Roitman, I., Pacheco-Pascagaza, A. M., Gou, Y., Roberts, J., Barrett, K., Ferreira, L. G., Shimbo, J. Z., Alencar, A., … Balzter, H. (2020). Woody Aboveground Biomass Mapping of the Brazilian Savanna with a Multi-Sensor and Machine Learning Approach. *Remote Sensing*, *12*(17), 2685. https://doi.org/10.3390/rs12172685

Bonan, G. B. (2008). Forests and Climate Change: Forcings, Feedbacks, and the Climate Benefits of Forests. *Science*, *320*(5882), 1444–1449. https://doi.org/10.1126/science.1155121

Bonilla-Moheno, M., Redo, D. J., Aide, T. M., Clark, M. L., & Grau, H. R. (2013). Vegetation change and land tenure in Mexico: A country-wide analysis. Land Use Policy, 30(1), 355–364. https://doi.org/10.1016/j.landusepol.2012.04.002

Breiman, L. (2001). Random Forests. Machine Learning, 45(1), 5–32.

Büntgen, U., Krusic, P. J., Piermattei, A., Coomes, D. A., Esper, J., Myglan, V. S., Kirdyanov, A. V., Camarero, J. J., Crivellaro, A., & Körner, C. (2019). Limited capacity of tree growth to mitigate the global greenhouse effect under predicted warming. Nature Communications, 10(1), 2171. https://doi.org/10.1038/s41467-019-10174-4

Caamal-Sosa, J. P., Dupuy, J. M., Torres, J.L.A., Luis, J., Stefafoni, H., Ruíz, A.H.H., Chim, M.T., Wayson, C., Álvarez, M.O., Merlín, D.L. and Montero, V.M., (2016) Estudio de caso del sitio de monitoreo intensivo del carbono, Kaxil Kiuic, Yucatán Programa Mexicano del Carbono.

Carmel, Y. (2004). Controlling Data Uncertainty via Aggregation in Remotely Sensed Data. IEEE Geoscience and Remote Sensing Letters, 1(2), 39–41. https://doi.org/10.1109/LGRS.2004.823453

Cartus, O., Kellndorfer, J., Walker, W., Franco, C., Bishop, J., Santos, L., & Fuentes, J. (2014). A National, Detailed Map of Forest Aboveground Carbon Stocks in Mexico. *Remote Sensing*, *6*(6), 5559–5588. https://doi.org/10.3390/rs6065559

Chave, J., Andalo, C., Brown, S., Cairns, M. A., Chambers, J. Q., Eamus, D., Fölster, H., Fromard, F., Higuchi, N., Kira, T., Lescure, J.-P., Nelson, B. W., Ogawa, H., Puig, H., Riéra, B., & Yamakura, T. (2005). Tree allometry and improved estimation of carbon stocks and balance in tropical forests. *Oecologia*, *145*(1), 87–99. https://doi.org/10.1007/s00442-005-0100-x

Chave, Jerome, Condit, R., Aguilar, S., Hernandez, A., Lao, S., & Perez, R. (2004). Error propagation and scaling for tropical forest biomass estimates. *Philosophical Transactions of the Royal Society of London. Series B: Biological Sciences*, *359*(1443), 409–420. https://doi.org/10.1098/rstb.2003.1425

Chazdon, R. (2008). Chance and determinism in tropical forest succession. In *Tropical forest community ecology*. Wiley-Blackwell Pub.

Chazdon, R. L. (2017). Landscape Restoration, Natural Regeneration, and the Forests of the Future. *Annals of the Missouri Botanical Garden*, *102*(2), 251–257. https://doi.org/10.3417/2016035

Chazdon, R. L., Broadbent, E. N., Rozendaal, D. M. A., Bongers, F., Zambrano, A. M. A., Aide, T. M., Balvanera, P., Becknell, J. M., Boukili, V., Brancalion, P. H. S., Craven, D., Almeida-

Cortez, J. S., Cabral, G. A. L., de Jong, B., Denslow, J. S., Dent, D. H., DeWalt, S. J., Dupuy, J. M., Durán, S. M., … Poorter, L. (2016). Carbon sequestration potential of second-growth forest regeneration in the Latin American tropics. Science Advances, 2(5), e1501639. https://doi.org/10.1126/sciadv.1501639

Chazdon, R. L., E. N. Broadbent, D. M. A. Rozendaal, F. Bongers, A. M. A. Zambrano, T. M. Aide, P. Balvanera, J. M. Becknell, V. Boukili, P. H. S. Brancalion, D. Craven, J. S. Almeida-Cortez, G. A. L. Cabral, B. de Jong, J. S. Denslow, D. H. Dent, S. J. DeWalt, J. M. Dupuy, S. M. Durán, M. M. Espírito-Santo, M. C. Fandino, R. G. César, J. S. Hall, J. Luis Hernández-Stefanoni, C. C. Jakovac, A. B. Junqueira, D. Kennard, S. G. Letcher, M. Lohbeck, M. Martínez-Ramos, P. Massoca, J. A. Meave, R. Mesquita, F. Mora, R. Muñoz, R. Muscarella, Y. R. F. Nunes, S. Ochoa-Gaona, E. Orihuela-Belmonte, M. Peña-Claros, E. A. Pérez-García, D. Piotto, J. S. Powers, J. Rodríguez-Velazquez, I. E. Romero-Pérez, J. Ruíz, J. G. Saldarriaga, A. Sanchez-Azofeifa, N. B. Schwartz, M. K. Steininger, N. G. Swenson, M. Uriarte, M. van Breugel, H. van der Wal, M. D. M. Veloso, H. Vester, I. C. G. Vieira, T. Vizcarra Bentos, G. Bruce Williamson & L. Poorter. (2016) Carbon sequestration potential of second-growth forest regeneration in the Latin American tropics. Science Advances 2: e1501639.

Chen, G., Yang, Y., & Robinson, D. (2013). Allocation of gross primary production in forest ecosystems: Allometric constraints and environmental responses. *New Phytologist*, *200*(4), 1176–1186. https://doi.org/10.1111/nph.12426

Chen, H. Y. H., Luo, Y., Reich, P. B., Searle, E. B., & Biswas, S. R. (2016). Climate change-associated trends in net biomass change are age dependent in western boreal forests of Canada. *Ecology Letters*, *19*(9), 1150–1158. https://doi.org/10.1111/ele.12653

Clark, D. A., Brown, S., Kicklighter, D. W., Chambers, J. Q., Thomlinson, J. R., Ni, J., & Holland, E. A. (2001). NET PRIMARY PRODUCTION IN TROPICAL FORESTS: AN EVALUATION AND SYNTHESIS OF EXISTING FIELD DATA. *Ecological Applications*, *11*(2), 371–384. https://doi.org/10.1890/1051-0761(2001)011[0371:NPPITF]2.0.CO;2

Cochran, W. (1963). G. 1963. Sampling techniques. Nueva York, John Wiley Sons.

Collins, M. B., & Mitchard, E. T. A. (2015). Integrated radar and lidar analysis reveals extensive loss of remaining intact forest on Sumatra 2007–2010. Biogeosciences, 12(22), 6637-6653.

Congalton, R. G. (1991). A review of assessing the accuracy of classifications of remotely sensed data. *Remote Sensing of Environment*, *37*(1), 35–46. https://doi.org/10.1016/0034-4257(91)90048-B

Cook, B. D., Nelson, R. F., Middleton, E. M., Morton, D. C., McCorkel, J. T., Masek, J. G., J., R. K., & Montesano, P. M. (2013). NASA Goddard's LiDAR, hyperspectral and thermal (G-LiHT) airborne imager. *Remote Sensing*, *5*(8), 4045–4066.

Cook-Patton, S. C., Leavitt, S. M., Gibbs, D., Harris, N. L., Lister, K., Anderson-Teixeira, K. J., Briggs, R. D., Chazdon, R. L., Crowther, T. W., Ellis, P. W., Griscom, H. P., Herrmann, V., Holl, K. D., Houghton, R. A., Larrosa, C., Lomax, G., Lucas, R., Madsen, P., Malhi, Y., … Griscom, B. W. (2020). Mapping carbon accumulation potential from global natural forest regrowth. *Nature*, *585*(7826), 545–550. https://doi.org/10.1038/s41586-020-2686-x

Corona-Núñez, R. O., Campo, J., & Williams, M. (2018). Aboveground carbon storage in tropical dry forest plots in Oaxaca, Mexico. *Forest Ecology and Management*, *409*, 202–214. https://doi.org/10.1016/j.foreco.2017.11.014

Coursolle, C., Margolis, H. A., Giasson, M.-A., Bernier, P.-Y., Amiro, B. D., Arain, M. A., Barr, A. G., Black, T. A., Goulden, M. L., McCaughey, J. H., Chen, J. M., Dunn, A. L., Grant, R. F., & Lafleur, P. M. (2012a). Influence of stand age on the magnitude and seasonality of carbon fluxes in Canadian forests. *Agricultural and Forest Meteorology*, *165*, 136–148. https://doi.org/10.1016/j.agrformet.2012.06.011

Coursolle, C., Margolis, H. A., Giasson, M.-A., Bernier, P.-Y., Amiro, B. D., Arain, M. A., Barr, A. G., Black, T. A., Goulden, M. L., McCaughey, J. H., Chen, J. M., Dunn, A. L., Grant, R. F., & Lafleur, P. M. (2012b). Influence of stand age on the magnitude and seasonality of carbon fluxes in Canadian forests. *Agricultural and Forest Meteorology*, *165*, 136–148. https://doi.org/10.1016/j.agrformet.2012.06.011

Crowther, T. W., Glick, H. B., Covey, K. R., Bettigole, C., Maynard, D. S., Thomas, S. M., Smith, J. R., Hintler, G., Duguid, M. C., Amatulli, G., Tuanmu, M.-N., Jetz, W., Salas, C., Stam, C., Piotto, D., Tavani, R., Green, S., Bruce, G., Williams, S. J., … Bradford, M. A. (2015). Mapping tree density at a global scale. *Nature*, *525*(7568), 201–205. https://doi.org/10.1038/nature14967

Duncanson, L., Armston, J., Disney, M., Avitabile, V., Barbier, N., Calders, K., Carter, S., Chave, J., Herold, M., Crowther, T. W., Falkowski, M., Kellner, J. R., Labrière, N., Lucas, R., MacBean, N., McRoberts, R. E., Meyer, V., Næsset, E., Nickeson, J. E., … Williams, M. (2019). The Importance of Consistent Global Forest Aboveground Biomass Product

Validation. *Surveys in Geophysics*, *40*(4), 979–999. https://doi.org/10.1007/s10712-019-09538-8

Diario Oficial de la Federación (2011). Acuerdo por el que se integra y organiza la Zonificación Forestal. 30 de noviembre 2011 (Segunda Sección).

Dupuy, J. M., Hernández-Stefanoni, J. L., Hernández-Juárez, R. A., Tetetla-Rangel, E., López-Martínez, J. O., Leyequién-Abarca, E., Tun-Dzul, F. J., & May-Pat, F. (2012). Patterns and Correlates of Tropical Dry Forest Structure and Composition in a Highly Replicated Chronosequence in Yucatan, Mexico: Tropical Dry Forest Structure and Composition. *Biotropica*, *44*(2), 151–162. https://doi.org/10.1111/j.1744-7429.2011.00783.x

Dupuy, J.M., Durán-García R., García-Contreras, G., Acosta-Lugo, E., Méndez-González, M.E., Andrade-Hernández, M. (2015). Conservation and Use, en: Biodiversity and Conservation of the Yucatán Peninsula. Islebe G., A., Calmé S., León-Cortés J., Schmook, B. (Eds). Springer 10.1007/978-3-319-06529-8

Ellis, E. A., Hernandez Gomez, U., & Romero-Montero, J. A. (2017). Los procesos y causas del cambio en la cobertura forestal de la Península Yucatán, México. *Ecosistemas*, *26*(1), 101–111. https://doi.org/10.7818/ECOS.2017.26-1.16

Ellis, E. A., Montero, S. A., Hernández Gómez, I. U., Romero Montero, J. A., Ellis, P. W., Rodríguez-Ward, D., Blanco Reyes, P., & Putz, F. E. (2019). Reduced-impact logging practices reduce forest disturbance and carbon emissions in community managed forests on the Yucatán Peninsula, Mexico. *Forest Ecology and Management*, *437*, 396–410. https://doi.org/10.1016/j.foreco.2019.01.040

Ellis, E. A., Romero Montero, J. A., Hernández Gómez, I. U., Porter-Bolland, L., & Ellis, P. W. (2017). Private property and Mennonites are major drivers of forest cover loss in central Yucatan Peninsula, Mexico. *Land Use Policy*, *69*, 474–484. https://doi.org/10.1016/j.landusepol.2017.09.048

FAO (Ed.). (2016). *Forests and agriculture: Land-use challenges and opportunities*. FAO.

Field, C. B., & Raupach, M. R. (Eds.). (2004). *The global carbon cycle: Integrating humans, climate, and the natural world*. Island Press.

Gao, S. Z., Zhao, T., Wu, X., Li, D., Wu, Z., H., & Luo, H. (2016). Age and climate contribution to observed forest carbon sinks in East Asia. *Environmental Research Letters*, *11*(3), 034021.

García-Frapolli, E., Ayala-Orozco, B., Bonilla-Moheno, M., Espadas-Manrique, C., & Ramos-Fernández, G. (2007). Biodiversity conservation, traditional agriculture and ecotourism: Land cover/land use change projections for a natural protected area in the northeastern

Yucatan Peninsula, Mexico. *Landscape and Urban Planning*, *83*(2–3), 137–153. https://doi.org/10.1016/j.landurbplan.2007.03.007

Goetz, S. J., Hansen, M., Houghton, R. A., Walker, W., Laporte, N., & Busch, J. (2015). Measurement and monitoring needs, capabilities and potential for addressing reduced emissions from deforestation and forest degradation under REDD+. *Environmental Research Letters*, *10*(12), 123001. https://doi.org/10.1088/1748-9326/10/12/123001

Gonzalez, P., Asner, G. P., Battles, J. J., Lefsky, M. A., Waring, K. M., & Palace, M. (2010). Forest carbon densities and uncertainties from Lidar, QuickBird, and field measurements in California. *Remote Sensing of Environment*, *114*, 1561–1575. https://doi.org/10.1016/j.rse.2010.02.011

Goodman, R., & Herold, M. (2014). Why Maintaining Tropical Forests is Essential and Urgent for a Stable Climate. *SSRN Electronic Journal*. https://doi.org/10.2139/ssrn.2622758

Griscom, H. P., & Ashton, M. S. (2011). Restoration of dry tropical forests in Central America: A review of pattern and process. *Forest Ecology and Management*, *261*(10), 1564–1579. https://doi.org/10.1016/j.foreco.2010.08.027

Guariguata, M. R., & Ostertag, R. (2001). Neotropical secondary forest succession: Changes in structural and functional characteristics. *Forest Ecology and Management*, *148*(1–3), 185–206. https://doi.org/10.1016/S0378-1127(00)00535-1

Hansen, M. C., Potapov, P. V., Moore, R., Hancher, M., Turubanova, S. A., Tyukavina, A., Thau, D., Stehman, S. V., Goetz, S. J., Loveland, T. R., Kommareddy, A., Egorov, A., Chini, L., Justice, C. O., & Townshend, J. R. G. (2013). High-Resolution Global Maps of 21st-Century Forest Cover Change. *Science*, *342*(6160), 850–853. https://doi.org/10.1126/science.1244693

Haralick, R. M. (1979). Statistical and structural approaches to texture. *Proceedings of the IEEE*, *67*(5), 786–804.

Hermosilla, T., Wulder, M. A., White, J. C., Coops, N. C., & Hobart, G. W. (2015). An integrated Landsat time series protocol for change detection and generation of annual gap-free surface reflectance composites. *Remote Sensing of Environment*, *158*, 220–234. https://doi.org/10.1016/j.rse.2014.11.005

Hernández-Stefanoni, J., Dupuy, J., Johnson, K., Birdsey, R., Tun-Dzul, F., Peduzzi, A., Caamal-Sosa, J., Sánchez-Santos, G., & López-Merlín, D. (2014). Improving Species Diversity and Biomass Estimates of Tropical Dry Forests Using Airborne LiDAR. *Remote Sensing*, *6*(6), 4741–4763. https://doi.org/10.3390/rs6064741

Hernández-Stefanoni, J. L., Castillo-Santiago, M. Á., Mas, J. F., Wheeler, C. E., Andres-Mauricio, J., Tun-Dzul, F., George-Chacón, S. P., Reyes-Palomeque, G., Castellanos-Basto, B., Vaca, R., & Dupuy, J. M. (2020). Improving aboveground biomass maps of tropical dry forests by integrating LiDAR, ALOS PALSAR, climate and field data. *Carbon Balance and Management*, *15*(1), 15. https://doi.org/10.1186/s13021-020-00151-6

Hernández-Stefanoni, J. L., Dupuy, J. M., Tun-Dzul, F., & May-Pat, F. (2011). Influence of landscape structure and stand age on species density and biomass of a tropical dry forest across spatial scales. *Landscape Ecology*, *26*(3), 355–370. https://doi.org/10.1007/s10980-010-9561-3

Hooker, G., & Mentch, L. (2018). *Bootstrap bias corrections for ensemble methods Statistics and Computing* (Vol. 28).

Houghton, R. A. (2005). Aboveground Forest Biomass and the Global Carbon Balance. *Global Change Biology*, *11*(6), 945–958. https://doi.org/10.1111/j.1365-2486.2005.00955.x

Houghton, R. A., Byers, B., & Nassikas, A. A. (2015). A role for tropical forests in stabilizing atmospheric CO2. *Nature Climate Change*, *5*(12), 1022–1023. https://doi.org/10.1038/nclimate2869

Houghton, R. A., Hall, F., & Goetz, S. J. (2009). Importance of biomass in the global carbon cycle: BIOMASS IN THE GLOBAL CARBON CYCLE. *Journal of Geophysical Research: Biogeosciences*, *114*(G2), n/a-n/a. https://doi.org/10.1029/2009JG000935

Houghton, R. A., House, J. I., Pongratz, J., van der Werf, G. R., DeFries, R. S., Hansen, M. C., Le Quéré, C., & Ramankutty, N. (2012). Carbon emissions from land use and land-cover change. *Biogeosciences*, *9*(12), 5125–5142. https://doi.org/10.5194/bg-9-5125-2012

Houghton, Richard A. (2013). The emissions of carbon from deforestation and degradation in the tropics: Past trends and future potential. *Carbon Management*, *4*(5), 539–546. https://doi.org/10.4155/cmt.13.41

Huang, C., Goward, S. N., Masek, J. G., Thomas, N., Zhu, Z., & Vogelmann, J. E. (2010). An automated approach for reconstructing recent forest disturbance history using dense Landsat time series stacks. *Remote Sensing of Environment*, *114*(1), 183–198. https://doi.org/10.1016/j.rse.2009.08.017

International Panel on Climate Change IPCC (2006). Climate Change 2006: Informe de Síntesis. Contribución de los Grupos de trabajo I, II y III al Cuarto Informe de evaluación del Grupo Intergubernamental de Expertos sobre el Cambio Climático. Equipo de redacción principal: Pachauri, R.K. y Reisinger, A. (directores de la publicación, IPCC, Ginebra, Suiza. Pp. 104.

International Panel on Climate Change IPCC (2014). Climate Change 2014: Mitigation of Climate Change. Equipo de redacción principal: Pachauri, R.K. y Reisinger, A. (directores de la publicación, IPCC, Ginebra, Suiza. Pp. 104.

International Panel on Climate Change IPCC (2021) Summary for Policymakers. In: Climate Change 2021: The Physical Science Basis. Contribution of Working Group I to the Sixth Assessment Report of the Intergovernmental Panel on Climate Change [Masson-Delmotte, V., P. Zhai, A. Pirani, S. L. Connors, C. Péan, S. Berger, N. Caud, Y. Chen, L. Goldfarb, M. I. Gomis, M. Huang, K. Leitzell, E. Lonnoy, J.B.R. Matthews, T. K. Maycock, T. Waterfield, O. Yelekçi, R. Yu and B. Zhou (eds.)]. Cambridge University Press. In Press.

Joshi. (2016). Understanding ‘saturation’ of radar signals over forests. https://doi.org/10.1038/s41598-017-03469-3

Jucker, T., Caspersen, J., Chave, J., Antin, C., Barbier, N., Bongers, F., Dalponte, M., van Ewijk, K. Y., Forrester, D. I., Haeni, M., Higgins, S. I., Holdaway, R. J., Iida, Y., Lorimer, C., Marshall, P. L., Momo, S., Moncrieff, G. R., Ploton, P., Poorter, L., … Coomes, D. A. (2017). Allometric equations for integrating remote sensing imagery into forest monitoring programmes. *Global Change Biology*, *23*(1), 177–190. https://doi.org/10.1111/gcb.13388

Keenan, R. J. R., Achard, G. A., Freitas, F., Grainger, J. V., A., & Lindquist, E. (2015). Dynamics of global forest area: Results from the FAO Global Forest Resources Assessment 2015. *Forest Ecology and Management*, *352*, 9–20.

Keith, H., Mackey, B. G., & Lindenmayer, D. B. (2009). Re-evaluation of forest biomass carbon stocks and lessons from the world’s most carbon-dense forests. *Proceedings of the National Academy of Sciences*, *106*(28), 11635–11640. https://doi.org/10.1073/pnas.0901970106

Le Quéré, C., Andrew, R. M., Canadell, J. G., Sitch, S., Korsbakken, J. I., Peters, G. P., Manning, A. C., Boden, T. A., Tans, P. P., Houghton, R. A., Keeling, R. F., Alin, S., Andrews, O. D., Anthoni, P., Barbero, L., Bopp, L., Chevallier, F., Chini, L. P., Ciais, P., … Zaehle, S. (2016). Global Carbon Budget 2016. *Earth System Science Data*, *8*(2), 605–649. https://doi.org/10.5194/essd-8-605-2016

Le Quéré, C., Andrew, R. M., Friedlingstein, P., Sitch, S., Hauck, J., Pongratz, J., Pickers, P. A., Korsbakken, J. I., Peters, G. P., Canadell, J. G., Arneth, A., Arora, V. K., Barbero, L., Bastos, A., Bopp, L., Chevallier, F., Chini, L. P., Ciais, P., Doney, S. C., … Zheng, B. (2018). Global Carbon Budget 2018. *Earth System Science Data*, *10*(4), 2141–2194. https://doi.org/10.5194/essd-10-2141-2018

Lebrija-Trejos, E., Pérez-García, E. A., Meave, J. A., Poorter, L., & Bongers, F. (2011). Environmental changes during secondary succession in a tropical dry forest in Mexico. *Journal of Tropical Ecology*, *27*(5), 477–489. https://doi.org/10.1017/S0266467411000253

Letcher, S. G., & Chazdon, R. L. (2009). Rapid recovery of biomass, species richness, and species composition in a forest chronosequence in northeastern Costa Rica. *Biotropica*, *41*(5), 608-617.

Lewis, S. L., Wheeler, C. E., Mitchard, E. T. A., & Koch, A. (2019). Restoring natural forests is the best way to remove atmospheric carbon. *Nature*, *568*, 25-28,. https://doi.org/10.1038/d41586-019-01026-8.

Lohbeck, M., Poorter, L., Lebrija-Trejos, E., Martínez-Ramos, M., Meave, J. A., Paz, H., Pérez-García, E. A., Romero-Pérez, I. E., Tauro, A., & Bongers, F. (2013). Successional changes in functional composition contrast for dry and wet tropical forest. *Ecology*, *94*(6), 1211–1216. https://doi.org/10.1890/12-1850.1

Lu, D. (2006). The potential and challenge of remote sensing-based biomass estimation. *International Journal of Remote Sensing*, *27*(7), 1297–1328. https://doi.org/10.1080/01431160500486732

Lu, D., Chen, Q., Wang, G., Moran, E., Batistella, M., Zhang, M., Vaglio Laurin, G., & Saah, D. (2012). Aboveground Forest Biomass Estimation with Landsat and LiDAR Data and Uncertainty Analysis of the Estimates. *International Journal of Forestry Research*, *2012*, 1–16. https://doi.org/10.1155/2012/436537

Luther, J. E., Fournier, R. A., Lier, O. R., & Bujold, M. (2019). Extending ALS-Based Mapping of Forest Attributes with Medium Resolution Satellite and Environmental Data. *Remote Sensing*, *11*. https://doi.org/10.3390/rs11091092

Williams, M., Hill, T. C., & Ryan, C. M. (2013). Using biomass distributions to determine probability and intensity of tropical forest disturbance. *Plant Ecology & Diversity*, *6*(1), 87–99.

Malhi, Y. (2012). The productivity, metabolism and carbon cycle of tropical forest vegetation: Carbon cycle of tropical forests. *Journal of Ecology*, *100*(1), 65–75. https://doi.org/10.1111/j.1365-2745.2011.01916.x

Malhi, Y. R., Betts, J. T., Killeen, R. A., Li, T. J., W., & Nobre, C. A. (2008). Climate change, deforestation, and the fate of the Amazon. *Science*, *319*(5860), 169–172.

Markesteijn, L., Poorter, L., Bongers, F., Paz, H., & Sack, L. (2011). Hydraulics and life history of tropical dry forest tree species: Coordination of species' drought and shade tolerance. *New Phytologist*, *191*(2), 480–495. https://doi.org/10.1111/j.1469-8137.2011.03708.x

Markesteijn, L., Poorter, L., Paz, H., Sack, L., & Bongers, F. (2011). Ecological differentiation in xylem cavitation resistance is associated with stem and leaf structural traits: Vulnerability to cavitation of tropical dry forest tree species. *Plant, Cell & Environment*, *34*(1), 137–148. https://doi.org/10.1111/j.1365-3040.2010.02231.x

Martin, A. R., & Thomas, S. C. (2011). A Reassessment of Carbon Content in Tropical Trees. *PLoS ONE*, *6*(8), e23533. https://doi.org/10.1371/journal.pone.0023533

Mascaro, J., Asner, G. P., Knapp, D. E., Kennedy-Bowdoin, T., Martin, R. E., Anderson, C., Higgins, M., & Chadwick, K. D. (2014). A Tale of Two "Forests": Random Forest Machine Learning Aids Tropical Forest Carbon Mapping. *PLoS ONE*, *9*(1), e85993. https://doi.org/10.1371/journal.pone.0085993

Mascaro, J., Detto, M., Asner, G. P., & Muller-Landau, H. C. (2011). Evaluating uncertainty in mapping forest carbon with airborne LiDAR. *Remote Sensing of Environment*, *115*(12), 3770–3774. https://doi.org/10.1016/j.rse.2011.07.019

Mascorro, V. S. C., Kurz, N. C., A., W., & Olguín, M. (2016). Attributing changes in land cover using independent disturbance datasets: A case study of the Yucatan Peninsula, Mexico. *Regional Environmental Change*, *16*(1), 213–228.

Mascorro, V. S., Coops, N. C., Kurz, W. A., & Olguín, M. (2016). Attributing changes in land cover using independent disturbance datasets: A case study of the Yucatan Peninsula, Mexico. *Regional Environmental Change*, *16*(1), 213–228. https://doi.org/10.1007/s10113-014-0739-0

Matasci, G., Hermosilla, T., Wulder, M. A., White, J. C., Coops, N. C., Hobart, G. W., & Zald, H. S. J. (2018a). Large-area mapping of Canadian boreal forest cover, height, biomass and other structural attributes using Landsat composites and lidar plots. *Remote Sensing of Environment*, *209*, 90–106. https://doi.org/10.1016/j.rse.2017.12.020

Matasci, G., Hermosilla, T., Wulder, M. A., White, J. C., Coops, N. C., Hobart, G. W., & Zald, H. S. J. (2018b). Large-area mapping of Canadian boreal forest cover, height, biomass and other structural attributes using Landsat composites and lidar plots. *Remote Sensing of Environment*, *209*, 90–106. https://doi.org/10.1016/j.rse.2017.12.020

McGaughey, R. J. (2012). FUSION/LDV: Software for LIDAR data analysis and visualization. United States Department of Agriculture, Forest Service. *Pacific Northwest Research Station*, 154.

Mermoz, S., Réjou-Méchain, M., Villard, L., Le Toan, T., Rossi, V., & Gourlet-Fleury, S. (2015). Decrease of L-band SAR backscatter with biomass of dense forests. *Remote Sensing of Environment*, *159*, 307–317.

Mitchard, E. T. A., Saatchi, S. S., Woodhouse, I. H., Nangendo, G., Ribeiro, N. S., Williams, M., Ryan, C. M., Lewis, S. L., Feldpausch, T. R., & Meir, P. (2009). Using satellite radar backscatter to predict above-ground woody biomass: A consistent relationship across four different African landscapes. *Geophysical Research Letters*, *36*(23), L23401. https://doi.org/10.1029/2009GL040692

Mitchard, Edward T. A. (2018). The tropical forest carbon cycle and climate change. *Nature*, *559*(7715), 527–534. https://doi.org/10.1038/s41586-018-0300-2

Murphy, P. G., & Lugo, A. E. (1986). Ecology of Tropical Dry Forest. *Annual Review of Ecology and Systematics*, *17*(1), 67–88. https://doi.org/10.1146/annurev.es.17.110186.000435

Norden, N. C., Chao, R. L., Jiang, A., H., Y., & Vílchez-Alvarado, B. (2009). Resilience of tropical rain forests: Tree community reassembly in secondary forests. *Ecology Letters*, *12*(5), 385–394.

Olofsson, P., Foody, G. M., Herold, M., Stehman, S. V., Woodcock, C. E., & Wulder, M. A. (2014). Good practices for estimating area and assessing accuracy of land change. *Remote Sensing of Environment*, *148*, 42–57. https://doi.org/10.1016/j.rse.2014.02.015

Olofsson, P., Foody, G. M., Stehman, S. V., & Woodcock, C. E. (2013). Making better use of accuracy data in land change studies: Estimating accuracy and area and quantifying uncertainty using stratified estimation. *Remote Sensing of Environment*, *129*, 122–131. https://doi.org/10.1016/j.rse.2012.10.031

Pan, Y., Birdsey, R. A., Fang, J., Houghton, R., Kauppi, P. E., Kurz, W. A., Phillips, O. L., Shvidenko, A., Lewis, S. L., Canadell, J. G., Ciais, P., Jackson, R. B., Pacala, S. W., McGuire, A. D., Piao, S., Rautiainen, A., Sitch, S., & Hayes, D. (2011). A Large and Persistent Carbon Sink in the World’s Forests. *Science*, *333*(6045), 988–993. https://doi.org/10.1126/science.1201609

Pandit, S., Tsuyuki, S., & Dube, T. (2019). Exploring the inclusion of Sentinel-2 MSI texture metrics in above-ground biomass estimation in the community forest of Nepal. *Geocarto International*, 1–18.

Picard, N., Saint-André, L., & Henry, M. (2012). Manual de construcción de ecuaciones alométricas para estimar el volumen y la biomasa de los árboles: del trabajo de campo a la predicción.

Pedregosa, F., Varoquaux, G., Gramfort, A., Michel, V., Thirion, B., Grisel, O., Blondel, M., Prettenhofer, P., Weiss, R., Dubourg, V., Vanderplas, J., Passos, A., Cournapeau, D., Brucher, M., M, P., & Duchesnay, É. (2011). Scikit-learn. *Machine Learning in Python Journal of Machine Learning Research*, *12*, 2825 2830.

Pennington, R. T., Lavin, M., & Oliveira-Filho, A. (2009). Woody Plant Diversity, Evolution, and Ecology in the Tropics: Perspectives from Seasonally Dry Tropical Forests. *Annual Review of Ecology, Evolution, and Systematics*, *40*(1), 437–457. https://doi.org/10.1146/annurev.ecolsys.110308.120327

Pflugmacher, D., Cohen, W. B., Kennedy, R. E., & Yang, Z. (2014). Using Landsat-derived disturbance and recovery history and lidar to map forest biomass dynamics. *Remote Sensing of Environment*, *151*, 124–137. https://doi.org/10.1016/j.rse.2013.05.033

Philipson, C. D., Cutler, M. E. J., Brodrick, P. G., Asner, G. P., Boyd, D. S., Moura Costa, P., Fiddes, J., Foody, G. M., van der Heijden, G. M. F., Ledo, A., Lincoln, P. R., Margrove, J. A., Martin, R. E., Milne, S., Pinard, M. A., Reynolds, G., Snoep, M., Tangki, H., Sau Wai, Y., … Burslem, D. F. R. P. (2020). Active restoration accelerates the carbon recovery of human-modified tropical forests. *Science*, *369*(6505), 838–841. https://doi.org/10.1126/science.aay4490

Ploton, P., Mortier, F., Réjou-Méchain, M., Barbier, N., Picard, N., Rossi, V., Dormann, C., Cornu, G., Viennois, G., Bayol, N., Lyapustin, A., Gourlet-Fleury, S., & Pélissier, R. (2020). Spatial validation reveals poor predictive performance of large-scale ecological mapping models. *Nature Communications*, *11*(1). https://doi.org/10.1038/s41467-020-18321-y

Poorter, H., & Nagel, O. (2000). The role of biomass allocation in the growth response of plants to different levels of light, CO2, nutrients and water: A quantitative review. *Functional Plant Biology*, *27*(12), 1191. https://doi.org/10.1071/PP99173_CO

Poorter, L. (2009). Leaf traits show different relationships with shade tolerance in moist versus dry tropical forests. *New Phytologist*, *181*(4), 890–900. https://doi.org/10.1111/j.1469-8137.2008.02715.x

Poorter, L., Bongers, F., Aide, T. M., Almeyda Zambrano, A. M., Balvanera, P., Becknell, J. M., Boukili, V., Brancalion, P. H. S., Broadbent, E. N., Chazdon, R. L., Craven, D., de Almeida-Cortez, J. S., Cabral, G. A. L., de Jong, B. H. J., Denslow, J. S., Dent, D. H., DeWalt, S. J., Dupuy, J. M., Durán, S. M., … Rozendaal, D. M. A. (2016). Biomass resilience of Neotropical secondary forests. *Nature*, *530*(7589), 211–214. https://doi.org/10.1038/nature16512

Poorter, L., Rozendaal, D. M. A., Bongers, F., de Almeida-Cortez, J. S., Almeyda Zambrano, A. M., Álvarez, F. S., Andrade, J. L., Villa, L. F. A., Balvanera, P., Becknell, J. M., Bentos, T. V., Bhaskar, R., Boukili, V., Brancalion, P. H. S., Broadbent, E. N., César, R. G., Chave, J., Chazdon, R. L., Colletta, G. D., … Westoby, M. (2019). Wet and dry tropical forests show opposite successional pathways in wood density but converge over time. *Nature Ecology & Evolution*, *3*(6), 928–934. https://doi.org/10.1038/s41559-019-0882-6

Porter-Bolland, L., Ellis, E. A., Guariguata, M. R., Ruiz-Mallén, I., Negrete-Yankelevich, S., & Reyes-García, V. (2012). Community managed forests and forest protected areas: An assessment of their conservation effectiveness across the tropics. *Forest Ecology and Management*, *268*, 6–17. https://doi.org/10.1016/j.foreco.2011.05.034

Portillo-Quintero, C. A., & Sánchez-Azofeifa, G. A. (2010). Extent and conservation of tropical dry forests in the Americas. *Biological Conservation*, *143*(1), 144–155. https://doi.org/10.1016/j.biocon.2009.09.020

Portillo-Quintero, C., Sanchez-Azofeifa, A., Calvo-Alvarado, J., Quesada, M., & do Espirito Santo, M. M. (2015). The role of tropical dry forests for biodiversity, carbon and water conservation in the neotropics: Lessons learned and opportunities for its sustainable management. *Regional Environmental Change*, *15*(6), 1039–1049. https://doi.org/10.1007/s10113-014-0689-6

Powell, S. L., Cohen, W. B., Healey, S. P., Kennedy, R. E., Moisen, G. G., Pierce, K. B., & Ohmann, J. L. (2010). Quantification of live aboveground forest biomass dynamics with Landsat time-series and field inventory data: A comparison of empirical modeling approaches. *Remote Sensing of Environment*, *114*(5), 1053–1068. https://doi.org/10.1016/j.rse.2009.12.018

Quesada, C. A., Phillips, O. L., Schwarz, M., Czimczik, C. I., Baker, T. R., Patiño, S., Fyllas, N. M., Hodnett, M. G., Herrera, R., Almeida, S., Alvarez Dávila, E., Arneth, A., Arroyo, L., Chao, K. J., Dezzeo, N., Erwin, T., di Fiore, A., Higuchi, N., Honorio Coronado, E., … Lloyd, J. (2012). Basin-wide variations in Amazon forest structure and function are mediated by both soils and climate. *Biogeosciences*, *9*(6), 2203–2246. https://doi.org/10.5194/bg-9-2203-2012

Read, L., & Lawrence, D. (2003). Litter Nutrient Dynamics During Succession in Dry Tropical Forests of the Yucatan: Regional and Seasonal Effects. *Ecosystems*, *6*(8), 747–761. https://doi.org/10.1007/s10021-003-0177-1

Reich, P. B., Luo, Y., Bradford, J. B., Poorter, H., Perry, C. H., & Oleksyn, J. (2014). Temperature drives global patterns in forest biomass distribution in leaves, stems, and roots.

Proceedings of the National Academy of Sciences, *111*(38), 13721–13726. https://doi.org/10.1073/pnas.1216053111

Réjou-Méchain, M., Muller-Landau, H. C., Detto, M., Thomas, S. C., Le Toan, T., Saatchi, S. S., Barreto-Silva, J. S., Bourg, N. A., Bunyavejchewin, S., Butt, N., Brockelman, W. Y., Cao, M., Cárdenas, D., Chiang, J.-M., Chuyong, G. B., Clay, K., Condit, R., Dattaraja, H. S., Davies, S. J., … Chave, J. (2014). Local spatial structure of forest biomass and its consequences for remote sensing of carbon stocks. *Biogeosciences*, *11*(23), 6827–6840. https://doi.org/10.5194/bg-11-6827-2014

Roberts, D. R., Bahn, V., Ciuti, S., Boyce, M. S., Elith, J., Guillera-Arroita, G., Hauenstein, S., Lahoz-Monfort, J. J., Schröder, B., Thuiller, W., Warton, D. I., Wintle, B. A., Hartig, F., & Dormann, C. F. (2017). Cross-validation strategies for data with temporal, spatial, hierarchical, or phylogenetic structure. *Ecography*, *40*(8), 913–929. https://doi.org/10.1111/ecog.02881

Rodríguez-Veiga, P., Saatchi, S., Tansey, K., & Balzter, H. (2016). Magnitude, spatial distribution and uncertainty of forest biomass stocks in Mexico. *Remote Sensing of Environment*, *183*, 265–281. https://doi.org/10.1016/j.rse.2016.06.004

Rodríguez-Veiga, P., Quegan, S., Carreiras, J., Persson, H. J., Fransson, J. E., Hoscilo, A., ... & Berninger, A. (2019). Forest biomass retrieval approaches from earth observation in different biomes. International Journal of Applied Earth Observation and Geoinformation, 77, 53-68.

Roussel, J.-R., Caspersen, J., Béland, M., Thomas, S., & Achim, A. (2017). Removing bias from LiDAR-based estimates of canopy height: Accounting for the effects of pulse density and footprint size. *Remote Sensing of Environment*, *198*, 1–16. https://doi.org/10.1016/j.rse.2017.05.032

Rozendaal, D., Chazdon, R., Arreola-Villa, F., Balvanera, P., Bentos, T., Dupuy, J. M., Hernandez-Stefanoni, J. L., Jakovac, C., Lebrija-Trejos, E., Lohbeck, M., Martinez-Ramos, M., Massoca, P., Meave, J., Mesquita, R., Mora, F., Pérez-García, E., Romero, I. E., Saenz-Pedroza, I., Breugel, M., & Bongers, F. (2017). Demographic Drivers of Aboveground Biomass Dynamics During Secondary Succession in Neotropical Dry and Wet Forests. *Ecosystems*, *20*, 340-353 10 1007 10021-016-0029–4.

Ruiz, J., Fandino, M. C., & Chazdon, R. L. (2005). Vegetation Structure, Composition, and Species Richness Across a 56-year Chronosequence of Dry Tropical Forest on Providencia Island, Colombia1. *Biotropica*, *37*(4), 520–530. https://doi.org/10.1111/j.1744-7429.2005.00070.x

Saatchi, S. S., Harris, N. L., Brown, S., Lefsky, M., Mitchard, E. T. A., Salas, W., Zutta, B. R., Buermann, W., Lewis, S. L., Hagen, S., Petrova, S., White, L., Silman, M., & Morel, A. (2011). Benchmark map of forest carbon stocks in tropical regions across three continents. *Proceedings of the National Academy of Sciences*, *108*(24), 9899–9904. https://doi.org/10.1073/pnas.1019576108

Saini, R., & Ghosh, S. K. (2018). EXPLORING CAPABILITIES OF SENTINEL-2 FOR VEGETATION MAPPING USING RANDOM FOREST. *ISPRS - International Archives of the Photogrammetry, Remote Sensing and Spatial Information Sciences*, *XLII–3*, 1499–1502. https://doi.org/10.5194/isprs-archives-XLII-3-1499-2018

Sanaphre-Villanueva, L., Dupuy, J., Andrade, J., Reyes-García, C., Paz, H., & Jackson, P. (2016). Functional Diversity of Small and Large Trees along Secondary Succession in a Tropical Dry Forest. *Forests*, *7*(12), 163. https://doi.org/10.3390/f7080163

Sanchez-Azofeifa, A., Powers, J. S., Fernandes, G. W., & Quesada, M. (Eds.). (2013). Tropical Dry Forest Ecological Succession in Mexico: Synthesis of a Long-Term Study. In *Tropical Dry Forests in the Americas* (0 ed., pp. 35–52). CRC Press. https://doi.org/10.1201/b15417-5

Santoro, M., Cartus, O., Mermoz, S., Bouvet, A., Le Toan, T., Carvalhais, N., Rozendaal, D., Herold, M., Avitabile, V., Quegan, S., Carreiras, J., Rauste, Y., Balzter, H., Schmullius, C., Seifert, F.M., (2018), GlobBiomass global above-ground biomass and growing stock volume datasets, available on-line at http://globbiomass.org/products/global-mapping

Sexton, J. O., Song, X.-P., Feng, M., Noojipady, P., Anand, A., Huang, C., Kim, D.-H., Collins, K. M., Channan, S., DiMiceli, C., & Townshend, J. R. (2013). Global, 30-m resolution continuous fields of tree cover: Landsat-based rescaling of MODIS vegetation continuous fields with lidar-based estimates of error. *International Journal of Digital Earth*, *6*(5), 427–448. https://doi.org/10.1080/17538947.2013.786146

Shimada, M., & Ohtaki, T. (2010). Generating large-scale high-quality sar mosaic datasets: Application to PALSAR data for global monitoring. *IEEE J. Sel. Top. Appl. Earth Obs. Remote Sens*, *3*(4), 637–656.

Shimada, Masanobu, Itoh, T., Motooka, T., Watanabe, M., Shiraishi, T., Thapa, R., & Lucas, R. (2014). New global forest/non-forest maps from ALOS PALSAR data (2007–2010). *Remote Sensing of Environment*, *155*, 13–31. https://doi.org/10.1016/j.rse.2014.04.014

Slik, J. W. F., Aiba, S.-I., Brearley, F. Q., Cannon, C. H., Forshed, O., Kitayama, K., Nagamasu, H., Nilus, R., Payne, J., Paoli, G., Poulsen, A. D., Raes, N., Sheil, D., Sidiyasa, K., Suzuki, E., & van Valkenburg, J. L. C. H. (2010). Environmental correlates of tree biomass, basal area, wood specific gravity and stem density gradients in Borneo's tropical forests: Forest carbon and structure gradients. *Global Ecology and Biogeography*, *19*(1), 50–60. https://doi.org/10.1111/j.1466-8238.2009.00489.x

Smith, V., Portillo-Quintero, C., Sánches-Azofeifa, A., Hernández-Stefanoni, J.L. (2019). Assessing the accuracy of detected breaks in Landsat time series as predictors of small-scale deforestation in tropical dry forests of Mexico and Costa Rica. *Remote Sensing of Environment*, *221*, 707–721.

Soriano-Luna, M., Ángeles-Pérez, G., Guevara, M., Birdsey, R., Pan, Y., Vaquera-Huerta, H., Valdez-Lazalde, J., Johnson, K., & Vargas, R. (2018). Determinants of Above-Ground Biomass and Its Spatial Variability in a Temperate Forest Managed for Timber Production. *Forests*, *9*(8), 490. https://doi.org/10.3390/f9080490

Sosa, J. P. C., Rada, J. M. D., Torres, J. L. A., Luis, J., Stefafoni, H., Ruíz, A. H. H., Chim, M. T., Wayson, C., Álvarez, M. O., Merlín, D. L., Montero, V. M., & Martínez, L. M. V. (n.d.). *Estudio de caso del sitio de monitoreo intensivo del carbono, Kaxil Kiuic, Yucatán*. 89.

Stegen, J. C., Swenson, N. G., Enquist, B. J., White, E. P., Phillips, O. L., Jørgensen, P. M., Weiser, M. D., Monteagudo Mendoza, A., & Núñez Vargas, P. (2011). Variation in above-ground forest biomass across broad climatic gradients: Forest biomass and climate. *Global Ecology and Biogeography*, *20*(5), 744–754. https://doi.org/10.1111/j.1466-8238.2010.00645.x

Strobl, C., Boulesteix, A.-L., Zeileis, A., & Hothorn, T. (2007). Bias in random forest variable importance measures: Illustrations, sources and a solution. *BMC Bioinformatics*, *8*, 25. https://doi.org/10.1186/1471-2105-8-25

Svob, S., Arroyo-Mora, J. P., & Kalacska, M. (2014). A wood density and aboveground biomass variability assessment using pre-felling inventory data in Costa Rica. *Carbon Balance and Management*, *9*(1), 9. https://doi.org/10.1186/s13021-014-0009-y

Swenson, N. G., & Zambrano, J. (2017). Why wood density varies across communities. Journal of Vegetation Science, 28(1), 4–6. https://doi.org/10.1111/jvs.12510

Swinfield, T., Both, S., Riutta, T., Bongalov, B., Elias, D., Majalap-Lee, N., Ostle, N., Svátek, M., Kvasnica, J., Milodowski, D., Jucker, T., Ewers, R.M., Zhang, Y., Johnson, D., Teh, Y.A., Burslem, D.F.R.P., Malhi, Y., Coomes, D. (2020). Imaging spectroscopy reveals the effects of topography and logging on the leaf chemistry of tropical forest canopy trees. Global Change Biology 26, 989–1002. https://doi.org/10.1111/gcb.14903

R Development Core Team (2018). A Language and Environment for Statistical Computing. In R Foundation for Statistical Computing. http://www.Rproject.org.

Thapa, R. B., Watanabe, M., Motohka, T., & Shimada, M. (2015). Potential of high-resolution ALOS–PALSAR mosaic texture for aboveground forest carbon tracking in tropical region. *Remote Sensing of Environment*, *160*, 122–133. https://doi.org/10.1016/j.rse.2015.01.007

Thompson, I. M., McNulty, B., S., & Mosseler, A. (2009). Forest resilience, biodiversity, and climate change. *Secretariat of the Convention on Biological Diversity, Montreal. Technical Series*, *43*(43), 1–67.

Turner, M. G. (2010). Disturbance and landscape dynamics in a changing world. *Ecology*, *91*(10), 2833–2849. https://doi.org/10.1890/10-0097.1

United Nations Framework Convention of Climate Change (UNFCC): Issues relating to reducing emissions from deforestation in developing countries and recommendations on any further process. Submissions from parties. (2006). Available at: http://unfccc.int/resource/docs/2006/sbsta/eng/misc05.pdf

Urbazaev, M., Thiel, C., Cremer, F., Dubayah, R., Migliavacca, M., M, R., & Schmullius, C. (2018). Estimation of forest aboveground biomass and uncertainties by integration of field measurements. In *Airborne LiDAR, and SAR and optical satellite data in Mexico Carbon Balance and Management: Vol. 13 5*.

U.S. Geological Survey, 2016, Landsat—Earth observation satellites (ver. 1.1, August 2016): U.S. Geological Survey Fact Sheet 2015–3081, 4 p., http://dx.doi.org/10.3133/fs20153081.

Vafaei, S., Soosani, J., Adeli, K., Fadaei, H., Naghavi, H., Pham, T., & Tien Bui, D. (2018). Improving Accuracy Estimation of Forest Aboveground Biomass Based on Incorporation of ALOS-2 PALSAR-2 and Sentinel-2A Imagery and Machine Learning: A Case Study of the Hyrcanian Forest Area (Iran). *Remote Sensing*, *10*(2), 172. https://doi.org/10.3390/rs10020172

van der Walt, S., Schönberger, J. L., Nunez-Iglesias, J., Boulogne, F., Warner, J. D., Yager, N., Gouillart, E., Yu, T., & contributors, the scikit-image. (2014). scikit-image: Image processing in Python. *PeerJ*, *2*, e453. https://doi.org/10.7717/peerj.453

Verbesselt, J., Hyndman, R., Zeileis, A., & Culvenor, D. (2010). Phenological change detection while accounting for abrupt and gradual trends in satellite image time series. *Remote Sensing of Environment*, *114*(12), 2970–2980. https://doi.org/10.1016/j.rse.2010.08.003

Verbesselt, J., Zeileis, A., & Herold, M. (2012). Near real-time disturbance detection using satellite image time series. *Remote Sensing of Environment*, *123*, 98–108. https://doi.org/10.1016/j.rse.2012.02.022

Vieira, D. L. M., & Scariot, A. (2006). Principles of Natural Regeneration of Tropical Dry Forests for Restoration. *Restoration Ecology*, *14*(1), 11–20. https://doi.org/10.1111/j.1526-100X.2006.00100.x

Woodhouse, I. H. (2017). *Introduction to Microwave Remote Sensing*. https://www.taylorfrancis.com/books/9781315272573.

Wulder, M. A., White, J. C., Nelson, R. F., Næsset, E., Ørka, H. O., Coops, N. C., Hilker, T., Bater, C. W., & Gobakken, T. (2012). Lidar sampling for large-area forest characterization: A review. *Remote Sensing of Environment*, *121*, 196–209. https://doi.org/10.1016/j.rse.2012.02.001

Xu, L., Saatchi, S. S., Yang, Y., Yu, Y., & White, L. (2016). Performance of non-parametric algorithms for spatial mapping of tropical forest structure. *Carbon Balance and Management*, *11*(1), 18. https://doi.org/10.1186/s13021-016-0062-9

Yanai, R., Wayson, C., Lee, D., Espejo, A., Campbell, J. L., Green, M. B., Zukswert, J. M., Yoffe, S., Aukema, J., Lister, A., Kirchner, J. W., & G P Gamarra, J. (2020). Improving uncertainty in forest carbon accounting for REDD+ mitigation efforts. *Environmental Research Letters*. https://doi.org/10.1088/1748-9326/abb96f

Zhao, P., Lu, D., Wang, G., Liu, L., Li, D., Zhu, J., & Yu, S. (2016). Forest aboveground biomass estimation in Zhejiang Province using the integration of Landsat TM and ALOS PALSAR data. *Int J Appl Earth Obs Geoinf*, *53*, 1–15.

Zhu, K., Zhang, J., Niu, S., Chu, C., & Luo, Y. (2018). Limits to growth of forest biomass carbon sink under climate change. *Nature Communications*, *9*(1), 2709. https://doi.org/10.1038/s41467-018-05132-5

ANEXO I

Material suplementario Capítulo 2

Implementación del algoritmo de detección de cambios BFAST en R.

```
# Change detection : BFast implementation
# Stephanie P. George stephanie.p.george@gmail.com 31/08/2018
# Edited 27/04/2920
# This code is based on Smith et al.,(2019) and Devries et al., (2015)


# Install necessary packages (uncomment section 'ctrl + shift + c' and run)

# install.packages("snow") # for multicore processing only
# install.packages("devtools")
# ref = 'develop' # install developers version of BFast spatial
# devtools::install_github('loicdtx/bfastSpatial', ref = 'develop')



# For windows
# set working directory
# setwd("E:/ESPA/BFast/KIUIC/")

# Set directory path. This is the path where all landsat data is stored and where the following
directories have to be created
# 1) C:/ESPA/BFast/data/datastep/
# 2) C:/ESPA/BFast/data/out
# 3) C:/ESPA/BFast/data/datastep/landsat
# 4)C:/ESPA/BFast/data/datastep/ndvi

# for UNIX  change all working directories to adjust folder architecture
# setwd('/Volumes/ADATA\ HD710/')
setwd('/media/stevie/HD710 PRO/ESPA/BFast/KIUIC/')

# make sure all directories have been created in the correct order
# set working directory to the directory where "data" is stored
# set path for reading and saving files
path <- getwd()

# load bfastSpatial
library(bfastSpatial)
library(parallel)

# and set tmpdir
tmpDir <- rasterOptions()$tmpdir

# set the path to the location of data
inDir <- file.path(path, 'data')
```

```
# stepDir is where intermediary outputs are stored
stepDir <- file.path(inDir, 'datastep')

# directory for Landsat data (copy all data in tar.gz format, without stats and other files. Only
"L0720046589956T1" files).
# landsatDir <- file.path(stepDir, 'landsat')
# landsatDir57 <- file.path("/media/stevie/HD710 PRO/ESPA/BFast/FCP/L57")
# landsatDir8 <- file.path("/media/stevie/HD710 PRO/ESPA/BFast/FCP/L08_2020")

# directory for KIUIC and PALMAR path/row 20/46
# directory for FCP images path/row 20/47
# landsatDir57 <- file.path("E:/ESPA/BFast/FCP/L57")
# landsatDir8 <- file.path("E:/ESPA/BFast/KIUIC/L08")#directory for FCP
# where individual VI layers are stored prior to being stacked; ndviDir, eviDir, etc. are
subdirectories of stepDir (Here we only used NDVI)
ndviDir <- file.path(stepDir, 'ndvi')
#ndviDir <- 'direccion/de/carpeta'
# eviDir <- file.path(stepDir, 'evi')
# msaviDir <- file.path(stepDir, 'msavi')
# ndmiDir <- file.path(stepDir, 'ndmi')
# nbrDir <- file.path(stepDir, 'nbr')
# nbr2Dir <- file.path(stepDir, 'nbr2')

#----- Set tempdir to create directory
#srdir <- dirout <- file.path(rasterOptions()$tmpdir, 'bfmspatial')
#dir.create(dirout, showWarning=FALSE)


# outDir is where outputs are stored
outDir <- file.path(inDir, 'out')
#outDir <- 'direccion/de/carpeta'
# create an extent object in order to clip processing extent to 60 x 60 km window (UTM 16 N
coords).
# It is extremely important for all the images to have the same extent, therefore we have to
specify via
# an extent object with four coordinates in UTM (xmin, xmax, ymin, ymax).

e <- extent(201753.52, 262685.59, 2170910.51, 2231840.28) # extent in Kaxil Kiuic
#e <- extent(159727,221807.4,2269844,2332127) # extent in Palmar
#e <- extent(331533.8, 391974.4, 2099930, 2160368) #extent in FCP

# processLandsatBatch is variable due to the change in USGS ESPA file naming convention. If
using developers version of bfastSpatial use the following to apply the cloud mask: keep =
c(322, 386) applies to Landsat 8 data. Change to: keep = c(66, 130) for Landsat 5-7 data
# for landsat 7 keep = c(66, 130))
# for landsat 8 keep = c(322, 386))
# unzip Landsat files, apply cloud mask, and calculate VI if not available,
# loop is created to read files when they have already created, if not function
processLandsatBatch
```

```
# will calculate Vi and apply cloud mask.

# processLandsatBatch(x = landsatDir8, outdir = ndviDir,
#                    delete = TRUE, e=e, overwrite = FALSE, mask = 'pixel_qa', vi = 'ndvi',
#                    keep = c(322, 386))
#


#
# if (!file.exists(file.path(inDir, 'ndvi_stack.grd'))) {
#                    processLandsatBatch(x = landsatDir8, outdir = ndviDir,
#                    delete = TRUE, e=e, overwrite = FALSE, mask = 'pixel_qa', vi = 'ndvi',
#                    keep = c(322, 386))
#                # make temporal ndvi stack
#                    ndviStack <- timeStack(x = ndviDir, pattern = glob2rx('*.grd'),
#                    filename = file.path(inDir, 'ndvi_stack.grd'),
#                    datatype = 'INT2S')
#                    } else {
#                    ndviStack <- brick(file.path(inDir, 'ndvi_stack.grd'))
#                    }
#
#
# if (!file.exists(file.path(inDir, 'ndvi_stack.grd'))) {
#                    processLandsatBatch(x = landsatDir57, outdir = ndviDir,
#                    delete = TRUE, e=e, overwrite = FALSE, mask = 'pixel_qa', vi = 'ndvi',
#                    keep = c(66, 130))
#                # make temporal ndvi stack
#                    ndviStack <- timeStack(x = ndviDir, pattern = glob2rx('*.grd'),
#                    filename = file.path(inDir, 'ndvi_stack.grd'),
#                    datatype = 'INT2S')
#                    } else {
#                    ndviStack <- brick(file.path(inDir, 'ndvi_stack.grd'))
#                    }


# filename = '/home/stevie/Change_detection/FCP/out/ndvi_stack.grd'
# filename = '/home/stevie/Change_detection/PALMAR/out/ndvi_stack.grd'

filename = '/home/stevie/Change_detection/KIUIC/out/ndvi_stack.grd'



ndviStack <- brick(filename)
# when running only ndviStack for 1st time use:
ndviStack <- timeStack(x = ndviDir, pattern = glob2rx('*.grd'), filename =
'/home/stevie/Change_detection/KIUIC/out/ndvi_stack.grd', datatype = 'INT2S')




# set ndviStack to x to prepare to run through bfmSpatial
x <- ndviStack
```

```
# Section for checking ndviStack has been created  correctly and have a visual overview of data
# show scene info from  ndviStack layers. Check for duplicate dates and incorrect names, which
are a problem for bfmSpatial.
# show the layer names
names(x)
  s <- getSceneinfo(names(x))
  s


  ### ADD THIS FUNCTION
  # filter the scene to show pixels above a certain threshold ( NDVI >.7 in this case)
  # define a function that takes a vector as an argument
checkThresh <- function(x){
    # first, get rid of NA's
    x <- x[!is.na(x)]
    # if there still values left, count how many are above the threshold
    # otherwise, return a 0
    if(length(x) > 0){
        y <- length(x[x > 7000])
    } else {
        y <- 0
    }
    # return the value
    return(y)
}

# pass this function summaryBrick
customStat <- summaryBrick(x, fun=checkThresh)
plot(customStat, main = "# of observations where NDVI > 0.7")

# IMPORTANT: create histogram for number of scenes per year
# add a column for years and plot # of scenes per year one must change start:end dates
s$year <- as.numeric(substr(s$date, 1, 4))
hist(s$year, main="Scenes per Year",
     xlab="year", ylab="# of scenes")

# plot count of valid observations
obs <- countObs(x)
plot(obs)

# obtain summary of valid observations
obs <- countObs(x, as.perc=TRUE)
summary(obs)
hist(obs, main ="percent obs")
# % NA per pixel
percNA <- 100 - countObs(x, as.perc=TRUE)
hist(percNA, main = "percent NA per pixel", xlab = "% NA per pixel")
plot(percNA, main="percent NA per pixel")
summary(percNA)
```

```
### ADD THIS FUNCTION
### Calculates annual summary statistics of a Raster Brick

annualSummary <- function(x, fun, dates=NULL, years=NULL, sensor=NULL, na.rm=NULL, ...){

   # if sensor is given (!is.null(sensor)), then limit the analysis to a particular sensor
   if(!is.null(sensor)){
      if ("ETM+" %in% sensor) {
         sensor <- unique(c(sensor, "ETM+ SLC-on", "ETM+ SLC-off"))
      }
      if(!.isLandsatSceneID(x)){
         warning("Scene IDs should be supplied as names(x) to subset by sensor. Ignoring...\n")
         scenes <- NULL
      } else {
         # 'allowed' scenes
         scenes <- which(getSceneinfo(names(x))$sensor %in% sensor)
      }
   } else {
      scenes <- NULL
   }

   # get dates (if is.null(dates))
   if(is.null(dates)) {
      if(is.null(getZ(x))) {
         if(!.isLandsatSceneID(x)){ # Check if dates can be extracted from layernames
            stop('A date vector must be supplied, either via the date argument, the z dimension of
x or comprised in names(x)')
         } else {
            dates <- as.Date(getSceneinfo(names(x))$date)
         }
      } else {
         dates <- getZ(x)
      }
   } else {
      if(length(dates) != nlayers(x)){
         stop("dates should be of same length as nlayers(x)")
      }
   }

   # trim dates if a sensor had been supplied
   if(!is.null(scenes)){
      dates <- dates[scenes]
   }

   # extract years
   y <- substr(dates, 1, 4)

   # vector of years over which to process
   yrs <- sort(unique(y))
```

```
    # limit to user-defined period
    if(!is.null(years))
        yrs <- yrs[yrs %in% years]

    # function to be applied over each pixel in the RasterBrickStack
    pixStat <- function(b){
        if(!is.null(scenes))
            b <- b[scenes]
        ps <- vector("numeric", length(yrs))
        for(i in 1:length(yrs)){
            args <- list(b[which(y == yrs[i])])
            if(is.logical(na.rm))
                args$na.rm <- na.rm
            ps[i] <- do.call(fun, args)
        }

        names(ps) <- yrs
        return(ps)
    }

    out <- mc.calc(x, fun=pixStat, ...)

    return(out)
}


#Calculate Statistics pixel wise per year function median
annualMed <- annualSummary(x, fun=median, na.rm=TRUE)
plot(annualMed, main = "Annual median")

# calculate mean and standard deviation values per year
annualMean <- annualSummary(x, fun=mean, na.rm=TRUE)
plot(annualMean, main = "Annual mean")
hist(annualMean, main = "Annual mean")

annualSD <- annualSummary(x, fun=sd, na.rm=TRUE)
plot(annualSD, main = "Annual SD")
hist(annualSD, main "Annual SD")
# custom function to calculate # of non-NA values per pixel per year (similar to countObs())
ff <- function(x)
length(x[!is.na(x)])
annualObs <- annualSummary(x,fun=ff)


###################################################################################
##########################
# BFM INTERACTIVE
# in order to use bfmPixel in interactive mode it is important to first plot a layer with visible data.
plot(x, 322)
```

```
# run bfmPixel() in interactive mode with a monitoring period
# starting @ the 1st day in 1990
bfm <- bfmPixel(x, start=2016, interactive=TRUE)
# choose the pixel whose time series you want to see by clicking on the map you plotted a moment ago
bfm$cell
# assign same pixel as a target cell
targcell <- bfm$cell
# inspect and plot the $bfm output
bfm <- bfmPixel(x, cell=targcell, start=c(2016, 1))
bfm
plot(bfm$bfm)

# trial pixel run for research parameter adjustment
bfm2 <- bfmPixel(x, cell=targcell, start=1995,
                formula=response~trend+harmon, h=0.25, history=c(1991, 4),type="OLS-MOSUM", order=1, plot=TRUE)

                                              # only trend
#bfm3 <- bfmPixel(x, cell=targcell, start=c(1990, 1),
            #    formula=response~trend, plot=TRUE)

# bfmPixel using a 1-year monitoring period
#bfm4 <- bfmPixel(x, cell=targcell, start=c(1990, 1),
           #     monend=c(1991, 1), plot=TRUE)

# it is possible to filter the analysis by sensor
# e.g. apply bfmPixel only on ETM+ data
#bfm5 <- bfmPixel(x, cell=targcell, start=c(2009, 1),
          #      sensor="ETM+", plot=TRUE)


# get MEDIAN value for timestack, it is also possible to obtain mean and other statistics and plot them
if (!file.exists(fn <- file.path(outDir, 'medianVI.grd')))
  # median values for all layers
  medVI <- summaryBrick(ndviStack, fun=median, na.rm=TRUE,
                       filename = fn) else {
                         medVI <- brick(fn)
                       }
# produce median plot
plot(medVI/10000)


###############################################################################################################
# BFMSPATIAL
# run bfmSpatial through the entire timeStack (all pixels)
# This is a computationally demanding process, multicore processing is preferred and can be specified (mc.cores= ) a set of parameters need to be set: formula (harmonic or trend or both),
```

history, start of monitoring period (start) level (significance), (h=) it is possible to retrieve the following layers via returnLayers = c("breakpoint", "magnitude", "error", "history", "r.squared", "adj.r.squared", "coefficients"). For editing parameters start= , monend, history

```
# Write breakpoint, yearly break month product, and breakpoint magnitude raster layers to GeoTiff files as well as the raster brick to a .grd file.
writeRaster(out[[1]], filename = "Kiuic1_NDVI_breaks.tif", format = "GTiff", overwrite = TRUE)
writeRaster(months$changeMonth1995, filename = "Kiuic1_NDVI_breaksmos95.tif", format = "GTiff", overwrite = TRUE)
writeRaster(months$changeMonth1996, filename = "Kiuic1_NDVI_breaksmos96.tif", format = "GTiff", overwrite = TRUE)
writeRaster(months$changeMonth1997, filename = "Kiuic1_NDVI_breaksmos97.tif", format = "GTiff", overwrite = TRUE)
writeRaster(months$changeMonth1998, filename = "Kiuic1_NDVI_breaksmos98.tif", format = "GTiff", overwrite = TRUE)
writeRaster(months$changeMonth1999, filename = "Kiuic1_NDVI_breaksmos99.tif", format = "GTiff", overwrite = TRUE)
writeRaster(months$changeMonth2000, filename = "Kiuic1_NDVI_breaksmos00.tif", format = "GTiff", overwrite = TRUE)
writeRaster(months$changeMonth2001, filename = "Kiuic1_NDVI_breaksmos01.tif", format = "GTiff", overwrite = TRUE)
writeRaster(months$changeMonth2002, filename = "Kiuic1_NDVI_breaksmos02.tif", format = "GTiff", overwrite = TRUE)
writeRaster(months$changeMonth2003, filename = "Kiuic1_NDVI_breaksmos03.tif", format = "GTiff", overwrite = TRUE)
writeRaster(months$changeMonth2004, filename = "Kiuic1_NDVI_breaksmos04.tif", format = "GTiff", overwrite = TRUE)
writeRaster(months$changeMonth2005, filename = "Kiuic1_NDVI_breaksmos05.tif", format = "GTiff", overwrite = TRUE)
writeRaster(months$changeMonth2006, filename = "Kiuic1_NDVI_breaksmos06.tif", format = "GTiff", overwrite = TRUE)
writeRaster(months$changeMonth2007, filename = "Kiuic1_NDVI_breaksmos07.tif", format = "GTiff", overwrite = TRUE)
writeRaster(months$changeMonth2008, filename = "Kiuic1_NDVI_breaksmos08.tif", format = "GTiff", overwrite = TRUE)
writeRaster(months$changeMonth2009, filename = "Kiuic1_NDVI_breaksmos09.tif", format = "GTiff", overwrite = TRUE)
writeRaster(months$changeMonth2010, filename = "Kiuic1_NDVI_breaksmos10.tif", format = "GTiff", overwrite = TRUE)
writeRaster(months$changeMonth2011, filename = "Kiuic1_NDVI_breaksmos11.tif", format = "GTiff", overwrite = TRUE)
writeRaster(months$changeMonth2012, filename = "Kiuic1_NDVI_breaksmos12.tif", format = "GTiff", overwrite = TRUE)
writeRaster(months$changeMonth2013, filename = "Kiuic1_NDVI_breaksmos13.tif", format = "GTiff", overwrite = TRUE)
writeRaster(months$changeMonth2014, filename = "Kiuic1_NDVI_breaksmos14.tif", format = "GTiff", overwrite = TRUE)
writeRaster(months$changeMonth2015, filename = "Kiuic1_NDVI_breaksmos15.tif", format = "GTiff", overwrite = TRUE)
```

```
writeRaster(months$changeMonth2016, filename = "Kiuic1_NDVI_breaksmos16.tif", format =
"GTiff", overwrite = TRUE)
writeRaster(months$changeMonth2017, filename = "Kiuic1_NDVI_breaksmos17.tif", format =
"GTiff", overwrite = TRUE)
writeRaster(months$changeMonth2018, filename = "Kiuic1_NDVI_breaksmos18.tif", format =
"GTiff", overwrite = TRUE)

# Test breakpoints
plot(ndviStack[[322]], col = grey.colors(255), legend = F)
plot(bfm[[1]], add=TRUE)
# Test months product
plot(months, col=cols, breaks=c(1:12), legend=FALSE)
legend("bottomright", legend=monthlabs, cex=0.5, fill=cols, ncol=2)
# Test magnitudes
plot(magn_bkp, main="Magnitude of a breakpoint")
plot(magn, main="Magnitude: all pixels")

rsq_map <- raster(bfm, 5)

# Extract R2 from map

writeRaster(
  rsq_map,
  filename="rsq_95-4y_Kiuic.tif",
  format="GTiff",
  overwrite=TRUE)

#Apply ndviStack function to all images

x <- ndviStack

#####  Predicting one year with all previous history
#######################################
############################################################################
################



  ######################################### 2020
###########################################



        if (!file.exists(fn <- file.path(outDir, 'bfm_20-all_harmon_1.grd'))) {
          # make sure the filename is correct and the folder exists
          bfm <- bfmSpatial(x = ndviStack, pptype = 'irregular',
                            start = 2020, history = c("all"), h=0.25, monend=NULL, level=0.05,
                            formula = response ~ harmon, type = "OLS-MOSUM",
                            order = 1, mc.cores = 1, returnLayers = c("breakpoint", "magnitude", "error",
                                                                      "history", "r.squared", "adj.r.squared", "coefficients"),
                            filename = file.path(outDir, 'bfm_20-all_harmon_1.grd')
          )
```

```
    } else {
      bfm <- brick(fn)
    }







########################################## 2019
############################################



      if (!file.exists(fn <- file.path(outDir, 'bfm_19-all_harmon_1.grd'))) {
        # make sure the filename is correct and the folder exists
        bfm <- bfmSpatial(x = ndviStack, pptype = 'irregular',
                          start = 2019, history = c("all"), h=0.25, monend=2020, level=0.05,
                          formula = response ~ harmon, type = "OLS-MOSUM",
                          order = 1, mc.cores = 1, returnLayers = c("breakpoint", "magnitude", "error",
                                                                    "history", "r.squared", "adj.r.squared",
"coefficients"),
                          filename = file.path(outDir, 'bfm_19-all_harmon_1.grd')
        )
      } else {
        bfm <- brick(fn)
      }



########################################## 2018
############################################


    if (!file.exists(fn <- file.path(outDir, 'bfm_18-all_harmon_1.grd'))) {
      # make sure the filename is correct and the folder exists
      bfm <- bfmSpatial(x = ndviStack, pptype = 'irregular',
                        start = 2018, history = c("all"), h=0.25, monend=2019, level=0.05,
                        formula = response ~ harmon, type = "OLS-MOSUM",
                        order = 1, mc.cores = 1, returnLayers = c("breakpoint", "magnitude", "error",
                                                                  "history", "r.squared", "adj.r.squared", "coefficients"),
                        filename = file.path(outDir, 'bfm_18-all_harmon_1.grd')
      )
    } else {
      bfm <- brick(fn)
    }

########################################## 2017
```

```
##############################################


  if (!file.exists(fn <- file.path(outDir, 'bfm_17-all_harmon_1.grd'))) {
    # make sure the filename is correct and the folder exists
    bfm <- bfmSpatial(x = ndviStack, pptype = 'irregular',
                      start = 2017, history = c("all"), h=0.25, monend=2018, level=0.05,
                      formula = response ~ harmon, type = "OLS-MOSUM",
                      order = 1, mc.cores = 1, returnLayers = c("breakpoint", "magnitude", "error",
                                                             "history", "r.squared", "adj.r.squared", "coefficients"),
                      filename = file.path(outDir, 'bfm_17-all_harmon_1.grd')
    )
  } else {
    bfm <- brick(fn)
  }

############################################   2016
##############################################


if (!file.exists(fn <- file.path(outDir, 'bfm_16-all_harmon_1.grd'))) {
  # make sure the filename is correct and the folder exists
  bfm <- bfmSpatial(x = ndviStack, pptype = 'irregular',
                    start = 2016, history = c("all"), h=0.25, monend=2017, level=0.05,
                    formula = response ~ harmon, type = "OLS-MOSUM",
                    order = 1, mc.cores = 4, returnLayers = c("breakpoint", "magnitude", "error",
                                                           "history", "r.squared", "adj.r.squared", "coefficients"),
                    filename = file.path(outDir, 'bfm_16-all_harmon_1.grd')
  )
} else {
  bfm <- brick(fn)
}

###########################################   2015
##############################################

if (!file.exists(fn <- file.path(outDir, 'bfm_15-all_harmon_1.grd'))) {
  # make sure the filename is correct and the folder exists
  bfm <- bfmSpatial(x = ndviStack, pptype = 'irregular',
                    start = 2015, history = c("all"), h=0.25, monend=2016, level=0.05,
                    formula = response ~ harmon, type = "OLS-MOSUM",
                    order = 1, mc.cores = 4, returnLayers = c("breakpoint", "magnitude", "error",
                                                           "history", "r.squared", "adj.r.squared", "coefficients"),
                    filename = file.path(outDir, 'bfm_15-all_harmon_1.grd')
  )
} else {
  bfm <- brick(fn)
}
############################################   2014
##############################################
```

```
if (!file.exists(fn <- file.path(outDir, 'bfm_14-all_harmon_1.grd'))) {
  # make sure the filename is correct and the folder exists
  bfm <- bfmSpatial(x = ndviStack, pptype = 'irregular',
                  start = 2014, history = c("all"), h=0.25, monend=2015, level=0.05,
                  formula = response ~ harmon, type = "OLS-MOSUM",
                  order = 1, mc.cores = 4, returnLayers = c("breakpoint", "magnitude", "error",
                                                    "history", "r.squared", "adj.r.squared", "coefficients"),
                  filename = file.path(outDir, 'bfm_14-all_harmon_1.grd')
  )
} else {
  bfm <- brick(fn)
}

#########################################   2013
###########################################

if (!file.exists(fn <- file.path(outDir, 'bfm_13-all_harmon_1.grd'))) {
  # make sure the filename is correct and the folder exists
  bfm <- bfmSpatial(x = ndviStack, pptype = 'irregular',
                  start = 2013, history = c("all"), h=0.25, monend=2014, level=0.05,
                  formula = response ~ harmon, type = "OLS-MOSUM",
                  order = 1, mc.cores = 4, returnLayers = c("breakpoint", "magnitude", "error",
                                                    "history", "r.squared", "adj.r.squared", "coefficients"),
                  filename = file.path(outDir, 'bfm_13-all_harmon_1.grd')
  )
} else {
  bfm <- brick(fn)
}

#########################################   2012
###########################################

if (!file.exists(fn <- file.path(outDir, 'bfm_12-all_harmon_1.grd'))) {
  # make sure the filename is correct and the folder exists
  bfm <- bfmSpatial(x = ndviStack, pptype = 'irregular',
                  start = 2012, history = c("all"), h=0.25, monend=2013, level=0.05,
                  formula = response ~ harmon, type = "OLS-MOSUM",
                  order = 1, mc.cores = 4, returnLayers = c("breakpoint", "magnitude", "error",
                                                    "history", "r.squared", "adj.r.squared", "coefficients"),
                  filename = file.path(outDir, 'bfm_12-all_harmon_1.grd')
  )
} else {
  bfm <- brick(fn)
}

#########################################   2011
###########################################
```

```
if (!file.exists(fn <- file.path(outDir, 'bfm_11-all_harmon_1.grd'))) {
  # make sure the filename is correct and the folder exists
  bfm <- bfmSpatial(x = ndviStack, pptype = 'irregular',
                    start = 2011, history = c("all"), h=0.25, monend=2012, level=0.05,
                    formula = response ~ harmon, type = "OLS-MOSUM",
                    order = 1, mc.cores = 4, returnLayers = c("breakpoint", "magnitude", "error",
                                                              "history", "r.squared", "adj.r.squared", "coefficients"),
                    filename = file.path(outDir, 'bfm_11-all_harmon_1.grd')
  )
} else {
  bfm <- brick(fn)
}

#########################################   2010
###########################################

if (!file.exists(fn <- file.path(outDir, 'bfm_10-all_harmon_1.grd'))) {
  # make sure the filename is correct and the folder exists
  bfm <- bfmSpatial(x = ndviStack, pptype = 'irregular',
                    start = 2010, history = c("all"), h=0.25, monend=2011, level=0.05,
                    formula = response ~ harmon, type = "OLS-MOSUM",
                    order = 1, mc.cores = 4, returnLayers = c("breakpoint", "magnitude", "error",
                                                              "history", "r.squared", "adj.r.squared", "coefficients"),
                    filename = file.path(outDir, 'bfm_10-all_harmon_1.grd')
  )
} else {
  bfm <- brick(fn)
}

#########################################   2009
###########################################


if (!file.exists(fn <- file.path(outDir, 'bfm_09-all_harmon_1.grd'))) {
  # make sure the filename is correct and the folder exists
  bfm <- bfmSpatial(x = ndviStack, pptype = 'irregular',
                    start = 2009, history = c("all"), h=0.25, monend=2010, level=0.05,
                    formula = response ~ harmon, type = "OLS-MOSUM",
                    order = 1, mc.cores = 4, returnLayers = c("breakpoint", "magnitude", "error",
                                                              "history", "r.squared", "adj.r.squared", "coefficients"),
                    filename = file.path(outDir, 'bfm_09-all_harmon_1.grd')
  )
} else {
  bfm <- brick(fn)
}

#########################################   2008
###########################################

if (!file.exists(fn <- file.path(outDir, 'bfm_08-all_harmon_1.grd'))) {
```

```
  # make sure the filename is correct and the folder exists
  bfm <- bfmSpatial(x = ndviStack, pptype = 'irregular',
                  start = 2008, history = c("all"), h=0.25, monend=2009, level=0.05,
                  formula = response ~ harmon, type = "OLS-MOSUM",
                  order = 1, mc.cores = 4, returnLayers = c("breakpoint", "magnitude", "error",
                                                        "history", "r.squared", "adj.r.squared", "coefficients"),
                  filename = file.path(outDir, 'bfm_08-all_harmon_1.grd')
  )
} else {
  bfm <- brick(fn)
}

##########################################   2007
############################################

if (!file.exists(fn <- file.path(outDir, 'bfm_07-all_harmon_1.grd'))) {
  # make sure the filename is correct and the folder exists
  bfm <- bfmSpatial(x = ndviStack, pptype = 'irregular',
                  start = 2007, history = c("all"), h=0.25, monend=2008, level=0.05,
                  formula = response ~ harmon, type = "OLS-MOSUM",
                  order = 1, mc.cores = 4, returnLayers = c("breakpoint", "magnitude", "error",
                                                        "history", "r.squared", "adj.r.squared", "coefficients"),
                  filename = file.path(outDir, 'bfm_07-all_harmon_1.grd')
  )
} else {
  bfm <- brick(fn)
}

##########################################   2006
############################################

if (!file.exists(fn <- file.path(outDir, 'bfm_06-all_harmon_1.grd'))) {
  # make sure the filename is correct and the folder exists
  bfm <- bfmSpatial(x = ndviStack, pptype = 'irregular',
                  start = 2006, history = c("all"), h=0.25, monend=2007, level=0.05,
                  formula = response ~ harmon, type = "OLS-MOSUM",
                  order = 1, mc.cores = 4, returnLayers = c("breakpoint", "magnitude", "error",
                                                        "history", "r.squared", "adj.r.squared", "coefficients"),
                  filename = file.path(outDir, 'bfm_06-all_harmon_1.grd')
  )
} else {
  bfm <- brick(fn)
}

##########################################   2005
############################################

if (!file.exists(fn <- file.path(outDir, 'bfm_05-all_harmon_1.grd'))) {
  # make sure the filename is correct and the folder exists
  bfm <- bfmSpatial(x = ndviStack, pptype = 'irregular',
```

```
                 start = 2005, history = c("all"), h=0.25, monend=2006, level=0.05,
                 formula = response ~ harmon, type = "OLS-MOSUM",
                 order = 1, mc.cores = 4, returnLayers = c("breakpoint", "magnitude", "error",
                                                     "history", "r.squared", "adj.r.squared", "coefficients"),
                 filename = file.path(outDir, 'bfm_05-all_harmon_1.grd')
  )
} else {
  bfm <- brick(fn)
}

############################################   2004
##############################################

if (!file.exists(fn <- file.path(outDir, 'bfm_04-all_harmon_1.grd'))) {
  # make sure the filename is correct and the folder exists
  bfm <- bfmSpatial(x = ndviStack, pptype = 'irregular',
                 start = 2004, history = c("all"), h=0.25, monend=2005, level=0.05,
                 formula = response ~ harmon, type = "OLS-MOSUM",
                 order = 1, mc.cores = 4, returnLayers = c("breakpoint", "magnitude", "error",
                                                     "history", "r.squared", "adj.r.squared", "coefficients"),
                 filename = file.path(outDir, 'bfm_04-all_harmon_1.grd')
  )
} else {
  bfm <- brick(fn)
}

############################################   2003
##############################################

if (!file.exists(fn <- file.path(outDir, 'bfm_03-all_harmon_1.grd'))) {
  # make sure the filename is correct and the folder exists
  bfm <- bfmSpatial(x = ndviStack, pptype = 'irregular',
                 start = 2003, history = c("all"), h=0.25, monend=2004, level=0.05,
                 formula = response ~ harmon, type = "OLS-MOSUM",
                 order = 1, mc.cores = 4, returnLayers = c("breakpoint", "magnitude", "error",
                                                     "history", "r.squared", "adj.r.squared", "coefficients"),
                 filename = file.path(outDir, 'bfm_03-all_harmon_1.grd')
  )
} else {
  bfm <- brick(fn)
}

############################################   2002
##############################################

if (!file.exists(fn <- file.path(outDir, 'bfm_02-all_harmon_1.grd'))) {
  # make sure the filename is correct and the folder exists
  bfm <- bfmSpatial(x = ndviStack, pptype = 'irregular',
                 start = 2002, history = c("all"), h=0.25, monend=2003, level=0.05,
                 formula = response ~ harmon, type = "OLS-MOSUM",
```

```
                 order = 1, mc.cores = 4, returnLayers = c("breakpoint", "magnitude", "error",
                                                 "history", "r.squared", "adj.r.squared", "coefficients"),
                 filename = file.path(outDir, 'bfm_02-all_harmon_1.grd')
  )
} else {
  bfm <- brick(fn)
}

##########################################   2001
############################################

if (!file.exists(fn <- file.path(outDir, 'bfm_01-all_harmon_1.grd'))) {
  # make sure the filename is correct and the folder exists
  bfm <- bfmSpatial(x = ndviStack, pptype = 'irregular',
                 start = 2001, history = c("all"), h=0.25, monend=2002, level=0.05,
                 formula = response ~ harmon, type = "OLS-MOSUM",
                 order = 1, mc.cores = 4, returnLayers = c("breakpoint", "magnitude", "error",
                                                 "history", "r.squared", "adj.r.squared", "coefficients"),
                 filename = file.path(outDir, 'bfm_01-all_harmon_1.grd')
  )
} else {
  bfm <- brick(fn)
}

##########################################   2000
############################################

if (!file.exists(fn <- file.path(outDir, 'bfm_00-all_harmon_1.grd'))) {
  # make sure the filename is correct and the folder exists
  bfm <- bfmSpatial(x = ndviStack, pptype = 'irregular',
                 start = 2000, history = c("all"), h=0.25, monend=2001, level=0.05,
                 formula = response ~ harmon, type = "OLS-MOSUM",
                 order = 1, mc.cores = 4, returnLayers = c("breakpoint", "magnitude", "error",
                                                 "history", "r.squared", "adj.r.squared", "coefficients"),
                 filename = file.path(outDir, 'bfm_00-all_harmon_1.grd')
  )
} else {
  bfm <- brick(fn)
}

##########################################   1999
############################################

if (!file.exists(fn <- file.path(outDir, 'bfm_99-all_harmon_1.grd'))) {
  # make sure the filename is correct and the folder exists
  bfm <- bfmSpatial(x = ndviStack, pptype = 'irregular',
                 start = 1999, history = c("all"), h=0.25, monend=2000, level=0.05,
                 formula = response ~ harmon, type = "OLS-MOSUM",
                 order = 1, mc.cores = 4, returnLayers = c("breakpoint", "magnitude", "error",
                                                 "history", "r.squared", "adj.r.squared", "coefficients"),
```

```
                filename = file.path(outDir, 'bfm_99-all_harmon_1.grd')
  )
} else {
  bfm <- brick(fn)
}

#########################################   1998
###########################################

if (!file.exists(fn <- file.path(outDir, 'bfm_98-all_harmon_1.grd'))) {
  # make sure the filename is correct and the folder exists
  bfm <- bfmSpatial(x = ndviStack, pptype = 'irregular',
                start = 1998, history = c("all"), h=0.25, monend=1999, level=0.05,
                formula = response ~ harmon, type = "OLS-MOSUM",
                order = 1, mc.cores = 4, returnLayers = c("breakpoint", "magnitude", "error",
                                        "history", "r.squared", "adj.r.squared", "coefficients"),
                filename = file.path(outDir, 'bfm_98-all_harmon_1.grd')
  )
} else {
  bfm <- brick(fn)
}

#########################################   1997
###########################################

if (!file.exists(fn <- file.path(outDir, 'bfm_97-all_harmon_1.grd'))) {
  # make sure the filename is correct and the folder exists
  bfm <- bfmSpatial(x = ndviStack, pptype = 'irregular',
                start = 1997, history = c("all"), h=0.25, monend=1998, level=0.05,
                formula = response ~ harmon, type = "OLS-MOSUM",
                order = 1, mc.cores = 4, returnLayers = c("breakpoint", "magnitude", "error",
                                        "history", "r.squared", "adj.r.squared", "coefficients"),
                filename = file.path(outDir, 'bfm_97-all_harmon_1.grd')
  )
} else {
  bfm <- brick(fn)
}

#########################################   1996
###########################################

if (!file.exists(fn <- file.path(outDir, 'bfm_96-all_harmon_1.grd'))) {
  # make sure the filename is correct and the folder exists
  bfm <- bfmSpatial(x = ndviStack, pptype = 'irregular',
                start = 1996, history = c("all"), h=0.25, monend=1997, level=0.05,
                formula = response ~ harmon, type = "OLS-MOSUM",
                order = 1, mc.cores = 4, returnLayers = c("breakpoint", "magnitude", "error",
                                        "history", "r.squared", "adj.r.squared", "coefficients"),
                filename = file.path(outDir, 'bfm_96-all_harmon_1.grd')
  )
```

```
} else {
  bfm <- brick(fn)
}

############################################   1995
##############################################

if (!file.exists(fn <- file.path(outDir, 'bfm_95-all_harmon_1.grd'))) {
  # make sure the filename is correct and the folder exists
  bfm <- bfmSpatial(x = ndviStack, pptype = 'irregular',
                  start = 1995, history = c("all"), h=0.25, monend=1996, level=0.05,
                  formula = response ~ harmon, type = "OLS-MOSUM",
                  order = 1, mc.cores = 4, returnLayers = c("breakpoint", "magnitude", "error",
                                                      "history", "r.squared", "adj.r.squared", "coefficients"),
                  filename = file.path(outDir, 'bfm_95-all_harmon_1.grd')
  )
} else {
  bfm <- brick(fn)
}



# Extraction of year segment output
#----------------------- 2020 ----------------------------------------------------

# filename: bfm_20-all_harmon_1.grd

fn <- file.path(outDir, 'bfm_20-all_harmon_1.grd')

bfm <- brick(fn)

# the first layer corresponds to breakpoints per year, which will correspond to change.
# write a raster to extract change layer

change <- raster(bfm, 1)

plot(change, main="Change: Breakpoints 2020")

writeRaster(
  change,
  filename="breaks_20-all_harmon_1.tif",
  format="GTiff",
  overwrite=TRUE)


# make months object
months <- changeMonth(change)
# set up labels and color map for months
monthlabs <- c("jan", "feb", "mar", "apr", "may", "jun",
              "jul", "aug", "sep", "oct", "nov", "dec")
```

```
cols <- rainbow(12)

# produce plot with changes per month
plot(months, col=cols, breaks=c(1:12), legend=FALSE)
# insert custom legend
legend("bottomright", legend=monthlabs, cex=0.5, fill=cols, ncol=2)

# second layer corresponds to magnitude
magn <- raster(bfm, 2)

plot(magn, main="Magnitude")
# store magnitude output in separate layer
writeRaster(
  magn,
  filename="magn_20-all_FCP.tif",
  format="GTiff",
  overwrite=TRUE)

# make a version showing only breakpoint pixels
magn_bkp <- magn
magn_bkp[is.na(change)] <- NA
op <- par(mfrow=c(1, 2))
plot(magn_bkp, main="Magnitude: breakpoints")
plot(magn, main="Magnitude: all pixels")


# store magnitude bkpts output in separate layer
writeRaster(
  magn_bkp,
  filename="magn_bkp_20-all_FCP.tif",
  format="GTiff",
  overwrite=TRUE)


#----------------------- 2019 ----------------------------------------------------

# filename: bfm_19-all_harmon_1.grd

fn <- file.path(outDir, 'bfm_19-all_harmon_1.grd')

bfm <- brick(fn)

# the first layer corresponds to breakpoints per year, which will correspond to change.
# write a raster to extract change layer

change <- raster(bfm, 1)

writeRaster(
  change,
  filename="breaks_19-all_harmon_1.tif",
```

```
  format="GTiff",
  overwrite=TRUE)


# make months object
months <- changeMonth(change)
# set up labels and color map for months
monthlabs <- c("jan", "feb", "mar", "apr", "may", "jun",
               "jul", "aug", "sep", "oct", "nov", "dec")
cols <- rainbow(12)

# produce plot with changes per month
plot(months, col=cols, breaks=c(1:12), legend=FALSE)
# insert custom legend
legend("bottomright", legend=monthlabs, cex=0.5, fill=cols, ncol=2)

# second layer corresponds to magnitude
magn <- raster(bfm, 2)
# store magnitude output in separate layer
writeRaster(
  magn,
  filename="magn_19-all_FCP.tif",
  format="GTiff",
  overwrite=TRUE)

# make a version showing only breakpoint pixels
magn_bkp <- magn
magn_bkp[is.na(change)] <- NA
op <- par(mfrow=c(1, 2))
plot(magn_bkp, main="Magnitude: breakpoints")
plot(magn, main="Magnitude: all pixels")


# store magnitude bkpts output in separate layer
writeRaster(
  magn_bkp,
  filename="magn_bkp_19-all_FCP.tif",
  format="GTiff",
  overwrite=TRUE)







#----------------------- 2018 --------------------------------------------------

# filename: bfm_18-all_harmon_1.grd
```

```
fn <- file.path(outDir, 'bfm_18-all_harmon_1.grd')

bfm <- brick(fn)

# the first layer corresponds to breakpoints per year, which will correspond to change.
# write a raster to extract change layer

change <- raster(bfm, 1)

writeRaster(
  change,
  filename="breaks_18-all_harmon_1.tif",
  format="GTiff",
  overwrite=TRUE)



# make months object
months <- changeMonth(change)
# set up labels and color map for months
monthlabs <- c("jan", "feb", "mar", "apr", "may", "jun",
               "jul", "aug", "sep", "oct", "nov", "dec")
cols <- rainbow(12)

# produce plot with changes per month
plot(months, col=cols, breaks=c(1:12), legend=FALSE)
# insert custom legend
legend("bottomright", legend=monthlabs, cex=0.5, fill=cols, ncol=2)

# second layer corresponds to magnitude
magn <- raster(bfm, 2)
# store magnitude output in separate layer
writeRaster(
  magn,
  filename="magn_18-all_FCP.tif",
  format="GTiff",
  overwrite=TRUE)

# make a version showing only breakpoint pixels
magn_bkp <- magn
magn_bkp[is.na(change)] <- NA
op <- par(mfrow=c(1, 2))
plot(magn_bkp, main="Magnitude: breakpoints")
plot(magn, main="Magnitude: all pixels")



# store magnitude bkpts output in separate layer
writeRaster(
  magn_bkp,
  filename="magn_bkp_18-all_FCP.tif",
```

```
  format="GTiff",
  overwrite=TRUE)





#------------------------ 2017 ----------------------------------------------------

# filename: bfm_17-all_harmon_1.grd

fn <- file.path(outDir, 'bfm_17-all_harmon_1.grd')

bfm <- brick(fn)

# the first layer corresponds to breakpoints per year, which will correspond to change.
# write a raster to extract change layer

change <- raster(bfm, 1)

writeRaster(
  change,
  filename="breaks_17-all_harmon_1.tif",
  format="GTiff",
  overwrite=TRUE)


# make months object
months <- changeMonth(change)
# set up labels and color map for months
monthlabs <- c("jan", "feb", "mar", "apr", "may", "jun",
               "jul", "aug", "sep", "oct", "nov", "dec")
cols <- rainbow(12)

# produce plot with changes per month
plot(months, col=cols, breaks=c(1:12), legend=FALSE)
# insert custom legend
legend("bottomright", legend=monthlabs, cex=0.5, fill=cols, ncol=2)

# second layer corresponds to magnitude
magn <- raster(bfm, 2)
# store magnitude output in separate layer
writeRaster(
  magn,
  filename="magn_17-all_FCP.tif",
  format="GTiff",
  overwrite=TRUE)

# make a version showing only breakpoint pixels
```

```
magn_bkp <- magn
magn_bkp[is.na(change)] <- NA
op <- par(mfrow=c(1, 2))
plot(magn_bkp, main="Magnitude: breakpoints")
plot(magn, main="Magnitude: all pixels")


# store magnitude bkpts output in separate layer
writeRaster(
  magn_bkp,
  filename="magn_bkp_17-all_FCP.tif",
  format="GTiff",
  overwrite=TRUE)

#------------------------ 2016 ----------------------------------------------------

# filename: bfm_16-all_harmon_1.grd

fn <- file.path(outDir, 'bfm_16-all_harmon_1.grd')

bfm <- brick(fn)

# the first layer corresponds to breakpoints per year, which will correspond to change.
# write a raster to extract change layer

change <- raster(bfm, 1)

writeRaster(
  change,
  filename="breaks_16-all_harmon_1.tif",
  format="GTiff",
  overwrite=TRUE)


# make months object
months <- changeMonth(change)
# set up labels and color map for months
monthlabs <- c("jan", "feb", "mar", "apr", "may", "jun",
               "jul", "aug", "sep", "oct", "nov", "dec")
cols <- rainbow(12)

# produce plot with changes per month
plot(months, col=cols, breaks=c(1:12), legend=FALSE)
# insert custom legend
legend("bottomright", legend=monthlabs, cex=0.5, fill=cols, ncol=2)

# second layer corresponds to magnitude
magn <- raster(bfm, 2)
# store magnitude output in separate layer
writeRaster(
```

```
  magn,
  filename="magn_16-all_Palmar.tif",
  format="GTiff",
  overwrite=TRUE)

# make a version showing only breakpoint pixels
magn_bkp <- magn
magn_bkp[is.na(change)] <- NA
op <- par(mfrow=c(1, 2))
plot(magn_bkp, main="Magnitude: breakpoints")
plot(magn, main="Magnitude: all pixels")


# store magnitude bkpts output in separate layer
writeRaster(
  magn_bkp,
  filename="magn_bkp_16-all_Palmar.tif",
  format="GTiff",
  overwrite=TRUE)

#----------------------- 2015 ----------------------------------------------------

# filename: bfm_15-all_harmon_1.grd

fn <- file.path(outDir, 'bfm_15-all_harmon_1.grd')

bfm <- brick(fn)

# the first layer corresponds to breakpoints per year, which will correspond to change.
# write a raster to extract change layer

change <- raster(bfm, 1)

writeRaster(
  change,
  filename="breaks_15-all_harmon_1.tif",
  format="GTiff",
  overwrite=TRUE)


# make months object
months <- changeMonth(change)
# set up labels and color map for months
monthlabs <- c("jan", "feb", "mar", "apr", "may", "jun",
               "jul", "aug", "sep", "oct", "nov", "dec")
cols <- rainbow(12)

# produce plot with changes per month
plot(months, col=cols, breaks=c(1:12), legend=FALSE)
# insert custom legend
```

```
legend("bottomright", legend=monthlabs, cex=0.5, fill=cols, ncol=2)

# second layer corresponds to magnitude
magn <- raster(bfm, 2)
# store magnitude output in separate layer
writeRaster(
  magn,
  filename="magn_15-all_Palmar.tif",
  format="GTiff",
  overwrite=TRUE)

# make a version showing only breakpoint pixels
magn_bkp <- magn
magn_bkp[is.na(change)] <- NA
op <- par(mfrow=c(1, 2))
plot(magn_bkp, main="Magnitude: breakpoints")
plot(magn, main="Magnitude: all pixels")


# store magnitude bkpts output in separate layer
writeRaster(
  magn_bkp,
  filename="magn_bkp_15-all_Palmar.tif",
  format="GTiff",
  overwrite=TRUE)

#------------------------ 2014 -----------------------------------------------------

# filename: bfm_14-all_harmon_1.grd

fn <- file.path(outDir, 'bfm_14-all_harmon_1.grd')

bfm <- brick(fn)

# the first layer corresponds to breakpoints per year, which will correspond to change.
# write a raster to extract change layer

change <- raster(bfm, 1)

writeRaster(
  change,
  filename="breaks_14-all_harmon_1.tif",
  format="GTiff",
  overwrite=TRUE)


# make months object
months <- changeMonth(change)
# set up labels and color map for months
monthlabs <- c("jan", "feb", "mar", "apr", "may", "jun",
```

```
        "jul", "aug", "sep", "oct", "nov", "dec")
cols <- rainbow(12)

# produce plot with changes per month
plot(months, col=cols, breaks=c(1:12), legend=FALSE)
# insert custom legend
legend("bottomright", legend=monthlabs, cex=0.5, fill=cols, ncol=2)

# second layer corresponds to magnitude
magn <- raster(bfm, 2)
# store magnitude output in separate layer
writeRaster(
  magn,
  filename="magn_14-all_Palmar.tif",
  format="GTiff",
  overwrite=TRUE)

# make a version showing only breakpoint pixels
magn_bkp <- magn
magn_bkp[is.na(change)] <- NA
op <- par(mfrow=c(1, 2))
plot(magn_bkp, main="Magnitude: breakpoints")
plot(magn, main="Magnitude: all pixels")


# store magnitude bkpts output in separate layer
writeRaster(
  magn_bkp,
  filename="magn_bkp_14-all_Palmar.tif",
  format="GTiff",
  overwrite=TRUE)


#----------------------- 2013 --------------------------------------------------

# filename: bfm_13-all_harmon_1.grd

fn <- file.path(outDir, 'bfm_13-all_harmon_1.grd')

bfm <- brick(fn)

# the first layer corresponds to breakpoints per year, which will correspond to change.
# write a raster to extract change layer

change <- raster(bfm, 1)

writeRaster(
  change,
  filename="breaks_13-all_harmon_1.tif",
  format="GTiff",
```

```
  overwrite=TRUE)


# make months object
months <- changeMonth(change)
# set up labels and color map for months
monthlabs <- c("jan", "feb", "mar", "apr", "may", "jun",
               "jul", "aug", "sep", "oct", "nov", "dec")
cols <- rainbow(12)

# produce plot with changes per month
plot(months, col=cols, breaks=c(1:12), legend=FALSE)
# insert custom legend
legend("bottomright", legend=monthlabs, cex=0.5, fill=cols, ncol=2)

# second layer corresponds to magnitude
magn <- raster(bfm, 2)
# store magnitude output in separate layer
writeRaster(
  magn,
  filename="magn_13-all_Palmar.tif",
  format="GTiff",
  overwrite=TRUE)

# make a version showing only breakpoint pixels
magn_bkp <- magn
magn_bkp[is.na(change)] <- NA
op <- par(mfrow=c(1, 2))
plot(magn_bkp, main="Magnitude: breakpoints")
plot(magn, main="Magnitude: all pixels")


# store magnitude bkpts output in separate layer
writeRaster(
  magn_bkp,
  filename="magn_bkp_13-all_Palmar.tif",
  format="GTiff",
  overwrite=TRUE)

#------------------------ 2012 ------------------------------------------------------

# filename: bfm_12-all_harmon_1.grd

fn <- file.path(outDir, 'bfm_12-all_harmon_1.grd')

bfm <- brick(fn)

# the first layer corresponds to breakpoints per year, which will correspond to change.
# write a raster to extract change layer
```

```
change <- raster(bfm, 1)

writeRaster(
  change,
  filename="breaks_12-all_harmon_1.tif",
  format="GTiff",
  overwrite=TRUE)


# make months object
months <- changeMonth(change)
# set up labels and color map for months
monthlabs <- c("jan", "feb", "mar", "apr", "may", "jun",
               "jul", "aug", "sep", "oct", "nov", "dec")
cols <- rainbow(12)

# produce plot with changes per month
plot(months, col=cols, breaks=c(1:12), legend=FALSE)
# insert custom legend
legend("bottomright", legend=monthlabs, cex=0.5, fill=cols, ncol=2)

# second layer corresponds to magnitude
magn <- raster(bfm, 2)
# store magnitude output in separate layer
writeRaster(
  magn,
  filename="magn_12-all_Palmar.tif",
  format="GTiff",
  overwrite=TRUE)

# make a version showing only breakpoint pixels
magn_bkp <- magn
magn_bkp[is.na(change)] <- NA
op <- par(mfrow=c(1, 2))
plot(magn_bkp, main="Magnitude: breakpoints")
plot(magn, main="Magnitude: all pixels")


# store magnitude bkpts output in separate layer
writeRaster(
  magn_bkp,
  filename="magn_bkp_12-all_Palmar.tif",
  format="GTiff",
  overwrite=TRUE)

#----------------------- 2011 ---------------------------------------------------

# filename: bfm_11-all_harmon_1.grd

fn <- file.path(outDir, 'bfm_11-all_harmon_1.grd')
```

```
bfm <- brick(fn)

# the first layer corresponds to breakpoints per year, which will correspond to change.
# write a raster to extract change layer

change <- raster(bfm, 1)

writeRaster(
  change,
  filename="breaks_11-all_harmon_1.tif",
  format="GTiff",
  overwrite=TRUE)



# make months object
months <- changeMonth(change)
# set up labels and color map for months
monthlabs <- c("jan", "feb", "mar", "apr", "may", "jun",
               "jul", "aug", "sep", "oct", "nov", "dec")
cols <- rainbow(12)

# produce plot with changes per month
plot(months, col=cols, breaks=c(1:12), legend=FALSE)
# insert custom legend
legend("bottomright", legend=monthlabs, cex=0.5, fill=cols, ncol=2)

# second layer corresponds to magnitude
magn <- raster(bfm, 2)
# store magnitude output in separate layer
writeRaster(
  magn,
  filename="magn_11-all_Palmar.tif",
  format="GTiff",
  overwrite=TRUE)

# make a version showing only breakpoint pixels
magn_bkp <- magn
magn_bkp[is.na(change)] <- NA
op <- par(mfrow=c(1, 2))
plot(magn_bkp, main="Magnitude: breakpoints")
plot(magn, main="Magnitude: all pixels")



# store magnitude bkpts output in separate layer
writeRaster(
  magn_bkp,
  filename="magn_bkp_11-all_Palmar.tif",
  format="GTiff",
  overwrite=TRUE)
```

```
#------------------------ 2010 -----------------------------------------------------

# filename: bfm_10-all_harmon_1.grd

fn <- file.path(outDir, 'bfm_10-all_harmon_1.grd')

bfm <- brick(fn)

# the first layer corresponds to breakpoints per year, which will correspond to change.
# write a raster to extract change layer

change <- raster(bfm, 1)

writeRaster(
  change,
  filename="breaks_10-all_harmon_1.tif",
  format="GTiff",
  overwrite=TRUE)


# make months object
months <- changeMonth(change)
# set up labels and color map for months
monthlabs <- c("jan", "feb", "mar", "apr", "may", "jun",
               "jul", "aug", "sep", "oct", "nov", "dec")
cols <- rainbow(12)

# produce plot with changes per month
plot(months, col=cols, breaks=c(1:12), legend=FALSE)
# insert custom legend
legend("bottomright", legend=monthlabs, cex=0.5, fill=cols, ncol=2)

# second layer corresponds to magnitude
magn <- raster(bfm, 2)
# store magnitude output in separate layer
writeRaster(
  magn,
  filename="magn_10-all_Palmar.tif",
  format="GTiff",
  overwrite=TRUE)

# make a version showing only breakpoint pixels
magn_bkp <- magn
magn_bkp[is.na(change)] <- NA
op <- par(mfrow=c(1, 2))
plot(magn_bkp, main="Magnitude: breakpoints")
plot(magn, main="Magnitude: all pixels")
```

```
# store magnitude bkpts output in separate layer
writeRaster(
  magn_bkp,
  filename="magn_bkp_10-all_Palmar.tif",
  format="GTiff",
  overwrite=TRUE)

#----------------------- 2009 ---------------------------------------------------

# filename: bfm_09-all_harmon_1.grd

fn <- file.path(outDir, 'bfm_09-all_harmon_1.grd')

bfm <- brick(fn)

# the first layer corresponds to breakpoints per year, which will correspond to change.
# write a raster to extract change layer

change <- raster(bfm, 1)

writeRaster(
  change,
  filename="breaks_09-all_harmon_1.tif",
  format="GTiff",
  overwrite=TRUE)


# make months object
months <- changeMonth(change)
# set up labels and color map for months
monthlabs <- c("jan", "feb", "mar", "apr", "may", "jun",
               "jul", "aug", "sep", "oct", "nov", "dec")
cols <- rainbow(12)

# produce plot with changes per month
plot(months, col=cols, breaks=c(1:12), legend=FALSE)
# insert custom legend
legend("bottomright", legend=monthlabs, cex=0.5, fill=cols, ncol=2)

# second layer corresponds to magnitude
magn <- raster(bfm, 2)
# store magnitude output in separate layer
writeRaster(
  magn,
  filename="magn_09-all_Palmar.tif",
  format="GTiff",
  overwrite=TRUE)

# make a version showing only breakpoint pixels
```

```
magn_bkp <- magn
magn_bkp[is.na(change)] <- NA
op <- par(mfrow=c(1, 2))
plot(magn_bkp, main="Magnitude: breakpoints")
plot(magn, main="Magnitude: all pixels")


# store magnitude bkpts output in separate layer
writeRaster(
  magn_bkp,
  filename="magn_bkp_09-all_Palmar.tif",
  format="GTiff",
  overwrite=TRUE)

#----------------------- 2008 --------------------------------------------------

# filename: bfm_08-all_harmon_1.grd

fn <- file.path(outDir, 'bfm_08-all_harmon_1.grd')

bfm <- brick(fn)

# the first layer corresponds to breakpoints per year, which will correspond to change.
# write a raster to extract change layer

change <- raster(bfm, 1)

writeRaster(
  change,
  filename="breaks_08-all_harmon_1.tif",
  format="GTiff",
  overwrite=TRUE)


# make months object
months <- changeMonth(change)
# set up labels and color map for months
monthlabs <- c("jan", "feb", "mar", "apr", "may", "jun",
               "jul", "aug", "sep", "oct", "nov", "dec")
cols <- rainbow(12)

# produce plot with changes per month
plot(months, col=cols, breaks=c(1:12), legend=FALSE)
# insert custom legend
legend("bottomright", legend=monthlabs, cex=0.5, fill=cols, ncol=2)

# second layer corresponds to magnitude
magn <- raster(bfm, 2)
# store magnitude output in separate layer
writeRaster(
```

```
  magn,
  filename="magn_08-all_Palmar.tif",
  format="GTiff",
  overwrite=TRUE)

# make a version showing only breakpoint pixels
magn_bkp <- magn
magn_bkp[is.na(change)] <- NA
op <- par(mfrow=c(1, 2))
plot(magn_bkp, main="Magnitude: breakpoints")
plot(magn, main="Magnitude: all pixels")


# store magnitude bkpts output in separate layer
writeRaster(
  magn_bkp,
  filename="magn_bkp_08-all_Palmar.tif",
  format="GTiff",
  overwrite=TRUE)

#----------------------- 2007 --------------------------------------------------

# filename: bfm_07-all_harmon_1.grd

fn <- file.path(outDir, 'bfm_07-all_harmon_1.grd')

bfm <- brick(fn)

# the first layer corresponds to breakpoints per year, which will correspond to change.
# write a raster to extract change layer

change <- raster(bfm, 1)

writeRaster(
  change,
  filename="breaks_07-all_harmon_1.tif",
  format="GTiff",
  overwrite=TRUE)


# make months object
months <- changeMonth(change)
# set up labels and color map for months
monthlabs <- c("jan", "feb", "mar", "apr", "may", "jun",
               "jul", "aug", "sep", "oct", "nov", "dec")
cols <- rainbow(12)

# produce plot with changes per month
plot(months, col=cols, breaks=c(1:12), legend=FALSE)
# insert custom legend
```

```
legend("bottomright", legend=monthlabs, cex=0.5, fill=cols, ncol=2)

# second layer corresponds to magnitude
magn <- raster(bfm, 2)
# store magnitude output in separate layer
writeRaster(
  magn,
  filename="magn_07-all_Palmar.tif",
  format="GTiff",
  overwrite=TRUE)

# make a version showing only breakpoint pixels
magn_bkp <- magn
magn_bkp[is.na(change)] <- NA
op <- par(mfrow=c(1, 2))
plot(magn_bkp, main="Magnitude: breakpoints")
plot(magn, main="Magnitude: all pixels")


# store magnitude bkpts output in separate layer
writeRaster(
  magn_bkp,
  filename="magn_bkp_07-all_Palmar.tif",
  format="GTiff",
  overwrite=TRUE)


#----------------------- 2006 ----------------------------------------------------

# filename: bfm_06-all_harmon_1.grd

fn <- file.path(outDir, 'bfm_06-all_harmon_1.grd')

bfm <- brick(fn)

# the first layer corresponds to breakpoints per year, which will correspond to change.
# write a raster to extract change layer

change <- raster(bfm, 1)

writeRaster(
  change,
  filename="breaks_06-all_harmon_1.tif",
  format="GTiff",
  overwrite=TRUE)


# make months object
months <- changeMonth(change)
# set up labels and color map for months
```

```
monthlabs <- c("jan", "feb", "mar", "apr", "may", "jun",
              "jul", "aug", "sep", "oct", "nov", "dec")
cols <- rainbow(12)

# produce plot with changes per month
plot(months, col=cols, breaks=c(1:12), legend=FALSE)
# insert custom legend
legend("bottomright", legend=monthlabs, cex=0.5, fill=cols, ncol=2)

# second layer corresponds to magnitude
magn <- raster(bfm, 2)
# store magnitude output in separate layer
writeRaster(
  magn,
  filename="magn_06-all_Palmar.tif",
  format="GTiff",
  overwrite=TRUE)

# make a version showing only breakpoint pixels
magn_bkp <- magn
magn_bkp[is.na(change)] <- NA
op <- par(mfrow=c(1, 2))
plot(magn_bkp, main="Magnitude: breakpoints")
plot(magn, main="Magnitude: all pixels")


# store magnitude bkpts output in separate layer
writeRaster(
  magn_bkp,
  filename="magn_bkp_06-all_Palmar.tif",
  format="GTiff",
  overwrite=TRUE)

#----------------------- 2005 ---------------------------------------------------

# filename: bfm_05-all_harmon_1.grd

fn <- file.path(outDir, 'bfm_05-all_harmon_1.grd')

bfm <- brick(fn)

# the first layer corresponds to breakpoints per year, which will correspond to change.
# write a raster to extract change layer

change <- raster(bfm, 1)

writeRaster(
  change,
  filename="breaks_05-all_harmon_1.tif",
  format="GTiff",
```

```
  overwrite=TRUE)


# make months object
months <- changeMonth(change)
# set up labels and color map for months
monthlabs <- c("jan", "feb", "mar", "apr", "may", "jun",
               "jul", "aug", "sep", "oct", "nov", "dec")
cols <- rainbow(12)

# produce plot with changes per month
plot(months, col=cols, breaks=c(1:12), legend=FALSE)
# insert custom legend
legend("bottomright", legend=monthlabs, cex=0.5, fill=cols, ncol=2)

# second layer corresponds to magnitude
magn <- raster(bfm, 2)
# store magnitude output in separate layer
writeRaster(
  magn,
  filename="magn_05-all_Palmar.tif",
  format="GTiff",
  overwrite=TRUE)

# make a version showing only breakpoint pixels
magn_bkp <- magn
magn_bkp[is.na(change)] <- NA
op <- par(mfrow=c(1, 2))
plot(magn_bkp, main="Magnitude: breakpoints")
plot(magn, main="Magnitude: all pixels")


# store magnitude bkpts output in separate layer
writeRaster(
  magn_bkp,
  filename="magn_bkp_05-all_Palmar.tif",
  format="GTiff",
  overwrite=TRUE)




#------------------------ 2004 ----------------------------------------------------

# filename: bfm_04-all_harmon_1.grd

fn <- file.path(outDir, 'bfm_04-all_harmon_1.grd')

bfm <- brick(fn)
```

```
# the first layer corresponds to breakpoints per year, which will correspond to change.
# write a raster to extract change layer

change <- raster(bfm, 1)

writeRaster(
  change,
  filename="breaks_04-all_harmon_1.tif",
  format="GTiff",
  overwrite=TRUE)



# make months object
months <- changeMonth(change)
# set up labels and color map for months
monthlabs <- c("jan", "feb", "mar", "apr", "may", "jun",
              "jul", "aug", "sep", "oct", "nov", "dec")
cols <- rainbow(12)

# produce plot with changes per month
plot(months, col=cols, breaks=c(1:12), legend=FALSE)
# insert custom legend
legend("bottomright", legend=monthlabs, cex=0.5, fill=cols, ncol=2)

# second layer corresponds to magnitude
magn <- raster(bfm, 2)
# store magnitude output in separate layer
writeRaster(
  magn,
  filename="magn_04-all_Palmar.tif",
  format="GTiff",
  overwrite=TRUE)

# make a version showing only breakpoint pixels
magn_bkp <- magn
magn_bkp[is.na(change)] <- NA
op <- par(mfrow=c(1, 2))
plot(magn_bkp, main="Magnitude: breakpoints")
plot(magn, main="Magnitude: all pixels")



# store magnitude bkpts output in separate layer
writeRaster(
  magn_bkp,
  filename="magn_bkp_04-all_Palmar.tif",
  format="GTiff",
  overwrite=TRUE)

#----------------------- 2003 ---------------------------------------------------
```

```
# filename: bfm_03-all_harmon_1.grd

fn <- file.path(outDir, 'bfm_03-all_harmon_1.grd')

bfm <- brick(fn)

# the first layer corresponds to breakpoints per year, which will correspond to change.
# write a raster to extract change layer

change <- raster(bfm, 1)

writeRaster(
  change,
  filename="breaks_03-all_harmon_1.tif",
  format="GTiff",
  overwrite=TRUE)



# make months object
months <- changeMonth(change)
# set up labels and color map for months
monthlabs <- c("jan", "feb", "mar", "apr", "may", "jun",
              "jul", "aug", "sep", "oct", "nov", "dec")
cols <- rainbow(12)

# produce plot with changes per month
plot(months, col=cols, breaks=c(1:12), legend=FALSE)
# insert custom legend
legend("bottomright", legend=monthlabs, cex=0.5, fill=cols, ncol=2)

# second layer corresponds to magnitude
magn <- raster(bfm, 2)
# store magnitude output in separate layer
writeRaster(
  magn,
  filename="magn_03-all_Palmar.tif",
  format="GTiff",
  overwrite=TRUE)

# make a version showing only breakpoint pixels
magn_bkp <- magn
magn_bkp[is.na(change)] <- NA
op <- par(mfrow=c(1, 2))
plot(magn_bkp, main="Magnitude: breakpoints")
plot(magn, main="Magnitude: all pixels")



# store magnitude bkpts output in separate layer
writeRaster(
  magn_bkp,
```

```
  filename="magn_bkp_03-all_Palmar.tif",
  format="GTiff",
  overwrite=TRUE)

#------------------------ 2002 -----------------------------------------------------

# filename: bfm_02-all_harmon_1.grd

fn <- file.path(outDir, 'bfm_02-all_harmon_1.grd')

bfm <- brick(fn)

# the first layer corresponds to breakpoints per year, which will correspond to change.
# write a raster to extract change layer

change <- raster(bfm, 1)

writeRaster(
  change,
  filename="breaks_02-all_harmon_1.tif",
  format="GTiff",
  overwrite=TRUE)


# make months object
months <- changeMonth(change)
# set up labels and color map for months
monthlabs <- c("jan", "feb", "mar", "apr", "may", "jun",
               "jul", "aug", "sep", "oct", "nov", "dec")
cols <- rainbow(12)

# produce plot with changes per month
plot(months, col=cols, breaks=c(1:12), legend=FALSE)
# insert custom legend
legend("bottomright", legend=monthlabs, cex=0.5, fill=cols, ncol=2)

# second layer corresponds to magnitude
magn <- raster(bfm, 2)
# store magnitude output in separate layer
writeRaster(
  magn,
  filename="magn_02-all_Palmar.tif",
  format="GTiff",
  overwrite=TRUE)

# make a version showing only breakpoint pixels
magn_bkp <- magn
magn_bkp[is.na(change)] <- NA
op <- par(mfrow=c(1, 2))
plot(magn_bkp, main="Magnitude: breakpoints")
```

```
plot(magn, main="Magnitude: all pixels")


# store magnitude bkpts output in separate layer
writeRaster(
  magn_bkp,
  filename="magn_bkp_02-all_Palmar.tif",
  format="GTiff",
  overwrite=TRUE)



#----------------------- 2001 -----------------------------------------------------

# filename: bfm_01-all_harmon_1.grd

fn <- file.path(outDir, 'bfm_01-all_harmon_1.grd')

bfm <- brick(fn)

# the first layer corresponds to breakpoints per year, which will correspond to change.
# write a raster to extract change layer

change <- raster(bfm, 1)

writeRaster(
  change,
  filename="breaks_01-all_harmon_1.tif",
  format="GTiff",
  overwrite=TRUE)


# make months object
months <- changeMonth(change)
# set up labels and color map for months
monthlabs <- c("jan", "feb", "mar", "apr", "may", "jun",
               "jul", "aug", "sep", "oct", "nov", "dec")
cols <- rainbow(12)

# produce plot with changes per month
plot(months, col=cols, breaks=c(1:12), legend=FALSE)
# insert custom legend
legend("bottomright", legend=monthlabs, cex=0.5, fill=cols, ncol=2)

# second layer corresponds to magnitude
magn <- raster(bfm, 2)
# store magnitude output in separate layer
writeRaster(
  magn,
  filename="magn_01-all_Palmar.tif",
  format="GTiff",
```

```
  overwrite=TRUE)

# make a version showing only breakpoint pixels
magn_bkp <- magn
magn_bkp[is.na(change)] <- NA
op <- par(mfrow=c(1, 2))
plot(magn_bkp, main="Magnitude: breakpoints")
plot(magn, main="Magnitude: all pixels")


# store magnitude bkpts output in separate layer
writeRaster(
  magn_bkp,
  filename="magn_bkp_01-all_Palmar.tif",
  format="GTiff",
  overwrite=TRUE)

#------------------------ 2000 ----------------------------------------------------

# filename: bfm_00-all_harmon_1.grd

fn <- file.path(outDir, 'bfm_00-all_harmon_1.grd')

bfm <- brick(fn)

# the first layer corresponds to breakpoints per year, which will correspond to change.
# write a raster to extract change layer

change <- raster(bfm, 1)

writeRaster(
  change,
  filename="breaks_00-all_harmon_1.tif",
  format="GTiff",
  overwrite=TRUE)


# make months object
months <- changeMonth(change)
# set up labels and color map for months
monthlabs <- c("jan", "feb", "mar", "apr", "may", "jun",
              "jul", "aug", "sep", "oct", "nov", "dec")
cols <- rainbow(12)

# produce plot with changes per month
plot(months, col=cols, breaks=c(1:12), legend=FALSE)
# insert custom legend
legend("bottomright", legend=monthlabs, cex=0.5, fill=cols, ncol=2)

# second layer corresponds to magnitude
```

```
magn <- raster(bfm, 2)
# store magnitude output in separate layer
writeRaster(
  magn,
  filename="magn_00-all_Palmar.tif",
  format="GTiff",
  overwrite=TRUE)

# make a version showing only breakpoint pixels
magn_bkp <- magn
magn_bkp[is.na(change)] <- NA
op <- par(mfrow=c(1, 2))
plot(magn_bkp, main="Magnitude: breakpoints")
plot(magn, main="Magnitude: all pixels")


# store magnitude bkpts output in separate layer
writeRaster(
  magn_bkp,
  filename="magn_bkp_00-all_Palmar.tif",
  format="GTiff",
  overwrite=TRUE)

#----------------------- 1999 ---------------------------------------------------

# filename: bfm_99-all_harmon_1.grd

fn <- file.path(outDir, 'bfm_99-all_harmon_1.grd')

bfm <- brick(fn)

# the first layer corresponds to breakpoints per year, which will correspond to change.
# write a raster to extract change layer

change <- raster(bfm, 1)

writeRaster(
  change,
  filename="breaks_99-all_harmon_1.tif",
  format="GTiff",
  overwrite=TRUE)


# make months object
months <- changeMonth(change)
# set up labels and color map for months
monthlabs <- c("jan", "feb", "mar", "apr", "may", "jun",
               "jul", "aug", "sep", "oct", "nov", "dec")
cols <- rainbow(12)
```

```
# produce plot with changes per month
plot(months, col=cols, breaks=c(1:12), legend=FALSE)
# insert custom legend
legend("bottomright", legend=monthlabs, cex=0.5, fill=cols, ncol=2)

# second layer corresponds to magnitude
magn <- raster(bfm, 2)
# store magnitude output in separate layer
writeRaster(
  magn,
  filename="magn_99-all_Palmar.tif",
  format="GTiff",
  overwrite=TRUE)

# make a version showing only breakpoint pixels
magn_bkp <- magn
magn_bkp[is.na(change)] <- NA
op <- par(mfrow=c(1, 2))
plot(magn_bkp, main="Magnitude: breakpoints")
plot(magn, main="Magnitude: all pixels")


# store magnitude bkpts output in separate layer
writeRaster(
  magn_bkp,
  filename="magn_bkp_99-all_Palmar.tif",
  format="GTiff",
  overwrite=TRUE)

#---------------------- 1998 -------------------------------------------------

# filename: bfm_98-all_harmon_1.grd

fn <- file.path(outDir, 'bfm_98-all_harmon_1.grd')

bfm <- brick(fn)

# the first layer corresponds to breakpoints per year, which will correspond to change.
# write a raster to extract change layer

change <- raster(bfm, 1)

writeRaster(
  change,
  filename="breaks_98-all_harmon_1.tif",
  format="GTiff",
  overwrite=TRUE)


# make months object
```

```
months <- changeMonth(change)
# set up labels and color map for months
monthlabs <- c("jan", "feb", "mar", "apr", "may", "jun",
              "jul", "aug", "sep", "oct", "nov", "dec")
cols <- rainbow(12)

# produce plot with changes per month
plot(months, col=cols, breaks=c(1:12), legend=FALSE)
# insert custom legend
legend("bottomright", legend=monthlabs, cex=0.5, fill=cols, ncol=2)

# second layer corresponds to magnitude
magn <- raster(bfm, 2)
# store magnitude output in separate layer
writeRaster(
  magn,
  filename="magn_98-all_Palmar.tif",
  format="GTiff",
  overwrite=TRUE)

# make a version showing only breakpoint pixels
magn_bkp <- magn
magn_bkp[is.na(change)] <- NA
op <- par(mfrow=c(1, 2))
plot(magn_bkp, main="Magnitude: breakpoints")
plot(magn, main="Magnitude: all pixels")


# store magnitude bkpts output in separate layer
writeRaster(
  magn_bkp,
  filename="magn_bkp_98-all_Palmar.tif",
  format="GTiff",
  overwrite=TRUE)

#----------------------- 1997 ---------------------------------------------------

# filename: bfm_97-all_harmon_1.grd

fn <- file.path(outDir, 'bfm_97-all_harmon_1.grd')

bfm <- brick(fn)

# the first layer corresponds to breakpoints per year, which will correspond to change.
# write a raster to extract change layer

change <- raster(bfm, 1)

writeRaster(
  change,
```

```
  filename="breaks_97-all_harmon_1.tif",
  format="GTiff",
  overwrite=TRUE)


# make months object
months <- changeMonth(change)
# set up labels and color map for months
monthlabs <- c("jan", "feb", "mar", "apr", "may", "jun",
               "jul", "aug", "sep", "oct", "nov", "dec")
cols <- rainbow(12)

# produce plot with changes per month
plot(months, col=cols, breaks=c(1:12), legend=FALSE)
# insert custom legend
legend("bottomright", legend=monthlabs, cex=0.5, fill=cols, ncol=2)

# second layer corresponds to magnitude
magn <- raster(bfm, 2)
# store magnitude output in separate layer
writeRaster(
  magn,
  filename="magn_97-all_Palmar.tif",
  format="GTiff",
  overwrite=TRUE)

# make a version showing only breakpoint pixels
magn_bkp <- magn
magn_bkp[is.na(change)] <- NA
op <- par(mfrow=c(1, 2))
plot(magn_bkp, main="Magnitude: breakpoints")
plot(magn, main="Magnitude: all pixels")


# store magnitude bkpts output in separate layer
writeRaster(
  magn_bkp,
  filename="magn_bkp_97-all_Palmar.tif",
  format="GTiff",
  overwrite=TRUE)

#----------------------- 1996 --------------------------------------------------

# filename: bfm_96-all_harmon_1.grd

fn <- file.path(outDir, 'bfm_96-all_harmon_1.grd')

bfm <- brick(fn)

# the first layer corresponds to breakpoints per year, which will correspond to change.
```

```
# write a raster to extract change layer

change <- raster(bfm, 1)

writeRaster(
  change,
  filename="breaks_96-all_harmon_1.tif",
  format="GTiff",
  overwrite=TRUE)



# make months object
months <- changeMonth(change)
# set up labels and color map for months
monthlabs <- c("jan", "feb", "mar", "apr", "may", "jun",
               "jul", "aug", "sep", "oct", "nov", "dec")
cols <- rainbow(12)

# produce plot with changes per month
plot(months, col=cols, breaks=c(1:12), legend=FALSE)
# insert custom legend
legend("bottomright", legend=monthlabs, cex=0.5, fill=cols, ncol=2)

# second layer corresponds to magnitude
magn <- raster(bfm, 2)
# store magnitude output in separate layer
writeRaster(
  magn,
  filename="magn_96-all_Palmar.tif",
  format="GTiff",
  overwrite=TRUE)

# make a version showing only breakpoint pixels
magn_bkp <- magn
magn_bkp[is.na(change)] <- NA
op <- par(mfrow=c(1, 2))
plot(magn_bkp, main="Magnitude: breakpoints")
plot(magn, main="Magnitude: all pixels")



# store magnitude bkpts output in separate layer
writeRaster(
  magn_bkp,
  filename="magn_bkp_96-all_Palmar.tif",
  format="GTiff",
  overwrite=TRUE)

#----------------------- 1995 ---------------------------------------------------

# filename: bfm_95-all_harmon_1.grd
```

```
fn <- file.path(outDir, 'bfm_95-all_harmon_1.grd')

bfm <- brick(fn)

# the first layer corresponds to breakpoints per year, which will correspond to change.
# write a raster to extract change layer

change <- raster(bfm, 1)

writeRaster(
  change,
  filename="breaks_95-all_harmon_1.tif",
  format="GTiff",
  overwrite=TRUE)



# make months object
months <- changeMonth(change)
# set up labels and color map for months
monthlabs <- c("jan", "feb", "mar", "apr", "may", "jun",
               "jul", "aug", "sep", "oct", "nov", "dec")
cols <- rainbow(12)

# produce plot with changes per month
plot(months, col=cols, breaks=c(1:12), legend=FALSE)
# insert custom legend
legend("bottomright", legend=monthlabs, cex=0.5, fill=cols, ncol=2)

# second layer corresponds to magnitude
magn <- raster(bfm, 2)
# store magnitude output in separate layer
writeRaster(
  magn,
  filename="magn_95-all_Palmar.tif",
  format="GTiff",
  overwrite=TRUE)

# make a version showing only breakpoint pixels
magn_bkp <- magn
magn_bkp[is.na(change)] <- NA
op <- par(mfrow=c(1, 2))
plot(magn_bkp, main="Magnitude: breakpoints")
plot(magn, main="Magnitude: all pixels")



# store magnitude bkpts output in separate layer
writeRaster(
  magn_bkp,
  filename="magn_bkp_95-all_Palmar.tif",
```

```
  format="GTiff",
  overwrite=TRUE)

# References

        # DeVries, B. Decuyper, M. Verbesselt, J. Zeileis, A. Herold, M. and Joseph, S. (2015). Tracking disturbance-regrowth dynamics in tropical forests using structural change detection and Landsat time series. Remote Sensing of Environment, 169, 320-334.

        # Smith V. Portillo-Quintero C. Sanchez-Azofeifa A. Hernández-Stefanoni J.L. (2019). Assessing the accuracy of detected breaks in Landsat time series as predictors of small-scale deforestation in tropical dry forests of Mexico and Costa Rica. Remote Sensing of Environment  221 (2019) 707 -721.
```

Supplementary 2

Validation locations for estimating accuracy measures in change (orange) and no change (red) estimations. Locations are shown in percent tree cover, in Landsat tree cover product (Sexton et al., 2016).

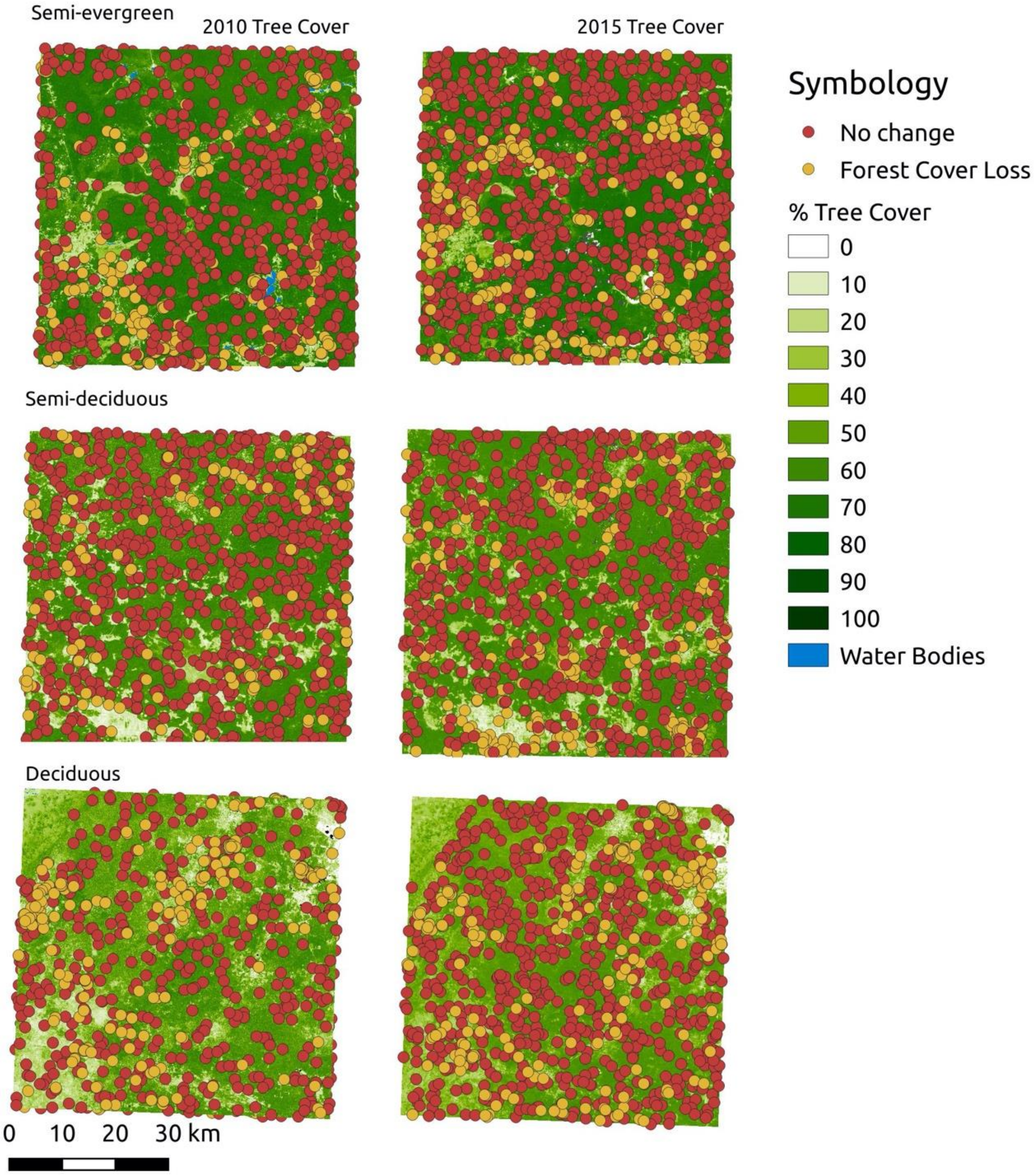

Supplementary 3 Relationship between aboveground biomass and forest age

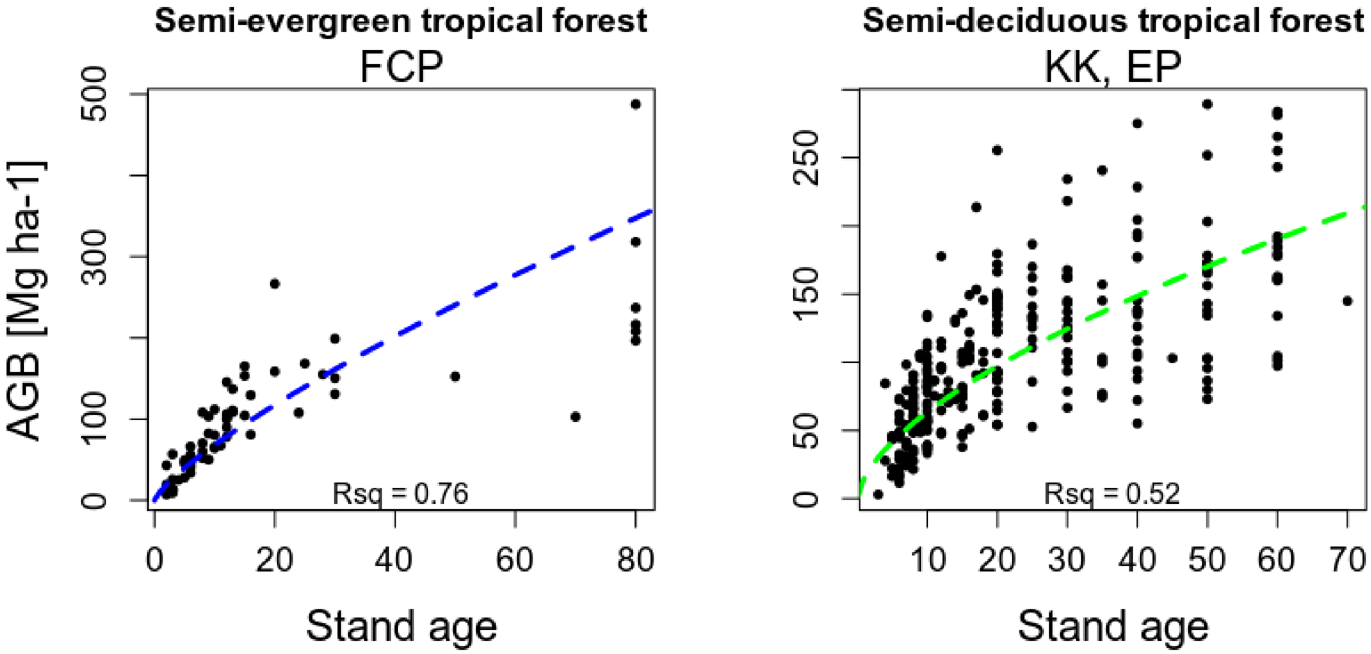

Supplementary figure 3. The AGB-age model derived from chronosequence data and used to estimate the spatial distribution of AGB with year of forest cover loss yielded an R^2 of 0.76 in semi-evergreen tropical forest, and 0.52 in semi-deciduous tropical forest (Supplementary Figure 3, Supplementary Table 3).

Supplementary Table 1. Model parameters for the AGB-age model in a) semi-deciduous and b) semi-evergreen forests. *** Variable was statistically significant at P <0.00.

Site	Dependent variable	Independent variable	ß	Standard error	R^2
Semi-evergreen	AGB	logAge***	0.78	0.14	0.76
Semi-deciduous	AGB	logAge***	0.61	0.10	0.52

Supplementary 4

Confusion matrix for change, and no change (NC) classes for accuracy assessment. Values are expressed as proportion of study area mapped following best practices by Olofsson et al., 2014.

Site	**Year**		**Reference**		
Deciduous	**2008**		Loss	NC	Total
		Loss	0.87	0.01	0.88
		NC	1.03	97.96	98.99
		Total	1.90	97.97	100.00
	2015				
		Loss	1.88	0.12	2.00
		NC	4.13	93.86	97.99
		Total	6.01	93.98	100.00
Semi-deciduous	**2006**				
		Loss	0.93	0.07	1.00
		NC	0.68	98.31	98.99
		Total	1.61	98.38	100.00
	2015				
		Loss	5.71	0.29	6.00
		NC	2.78	91.22	94.00
		Total	8.49	91.51	100.00
Semi-evergreen	**2010**				
		Loss	0.97	0.02	0.99
		NC	0.48	98.51	98.99
		Total	1.45	98.53	100.00
	2015				
		Loss	0.98	0.01	0.99
		NC	0.00	99.00	99.00
		Total	0.98	99.01	100.00

Supplementary 5

```
### FOREST COVER LOSS AND AGB MAP PRODUCTION
## This script contains Age/biomass relationships derived from chronosequence data
## application of AGB-age model to forest cover loss maps


# written by: Stephanie P. George, 2018
# stephanie.p.george@gmail.com


# install.packages("spatstat")
# library(spatstat)
library(raster)
library(rgdal)
site = "FCP"
setwd('/home/stevie/Change_detection/FCP/')


#### Part 1. Get yearmaps
### get yearmaps ####


 setwd("./tifs/sieves/")
 files <- list.files(getwd())


 years <- seq(2000,2020)
 get_yearmaps <- function(files, years) {
   for (i in 1:(length(files))) {
     mask1 <- raster(files[i])
```

```
    mask1 <- (mask1/mask1) + years[i]-1
    plot(mask1)
    writeRaster(mask1, filename = paste("yearmap",years[i], sep = "_"), format="GTiff")
  }}

 get_yearmaps(files, years)

 get oldest year from FNF mask
 year21 <- raster('/home/stevie/Change_detection/FCP/tifs/FCP_fnf.tif')
 year21[year21==0] <- NA
 year21 = year21 + 1998
 plot(year21)
 writeRaster(year21, filename = "year_21", format ="GTiff")

### Part 2. stitch maps together
## In QGIS use r.patch function and patch years 2020, 2019, 2018 to fill in NA's from younguest to oldest
### Part 3. Get AGE - BIOMASS model from chronosequence
## read in chronosequence data for obtaining model
chrono_data_kiuic<- read.csv("/home/stevie/CARDAMOM/chrono/Kiuic_Chrono_2010_DALEC.csv")

chrono_data_fcp <- read.csv("/home/stevie/Change_detection/FCP/QROO_oct_13_BIOMASA.csv")

## Get AGB from age - biomass relationship obtained from chronosequence mode.
# FCP
```

```
chrono_data_fcp <- chrono_data_fcp[ which(chrono_data_fcp$Edad < 100), ]
# plot(chrono_data_fcp$Edad, chrono_data_fcp$Biomasa, pch = 20, xlab = "Stand age", ylab ="AGB")


lm1 <- lm((chrono_data_fcp$Biomasa)~ log(chrono_data_fcp$Edad))
summary(lm1)
lm2 <- lm(log(chrono_data_fcp$Biomasa)~ log(chrono_data_fcp$Edad))
summary(lm2)
lm3 <- lm(log(chrono_data_fcp$Biomasa)~ (chrono_data_fcp$Edad))
summary(lm3)
lm4 <- lm((chrono_data_fcp$Biomasa)~ log(chrono_data_fcp$Edad))
summary(lm4)
lm5 <- lm(sqrt(chrono_data_fcp$Biomasa)~ sqrt(chrono_data_fcp$Edad))
summary(lm5)


##### Get AGB from age - biomass relationship obtained from chronosequence
### function to obtain AGB from age using a log-transformed agb-age relationship


# get_agb <- function(age) {
#   exp(lm2$coefficients[1] + log(age)*lm2$coefficients[2])
# }


get_agb <- function(age) {
  exp(lm2$coefficients[1] + log(age)*lm2$coefficients[2])
}
```

```
# kiuic & Palmar - read in Kiuic chrono
head(chrono_data_kiuic)

lm1 <- lm(chrono_data_kiuic$ALL~ log(chrono_data_kiuic$Edad.Estimada))
summary(lm1)
lm2 <- lm(log(chrono_data_kiuic$ALL)~ log(chrono_data_kiuic$Edad.Estimada))
summary(lm2)
lm3 <- lm(log(chrono_data_kiuic$ALL)~ (chrono_data_kiuic$Edad.Estimada))
summary(lm3)
lm4 <- lm((chrono_data_kiuic$ALL)~ log(chrono_data_kiuic$Edad.Estimada))
summary(lm4)
lm5 <- lm(sqrt(chrono_data_kiuic$ALL)~ sqrt(chrono_data_kiuic$Edad.Estimada))
summary(lm5)
## Part 4. Production of AGB map from age raster from agb-age relationship obtained from chronosequence data
# ### function to obtain AGB from age using a log-transformed agb-age relationship
#
 get_agb <- function(age) {
   exp(lm2$coefficients[1] + log(age)*lm2$coefficients[2])
 }
```

```
age_year <- raster('../../agemap/FCP_agemap_2020.tif') # introduce the year of forest loss raster

plot(age_year)

age <- 2020 - age_year

plot(age)

 ### apply function to age raster

 age_agb <- get_agb(age)

 plot(age_agb, main = site)

 write AGB raster

writeRaster(age_agb, filename=paste(site,"AGB", sep = "_"), format ="GTiff", overwrite =T)
```

Supplementary 6

Error maps obtained considering 18 months temporal lag between estimated forest cover loss and forest cover loss in reference imagery for Deciduous a), Semi-deciduous b) and semi-evergreen c) forests. Black areas correspond to non-forest areas (urban areas, permanent agriculture, roads and water bodies.

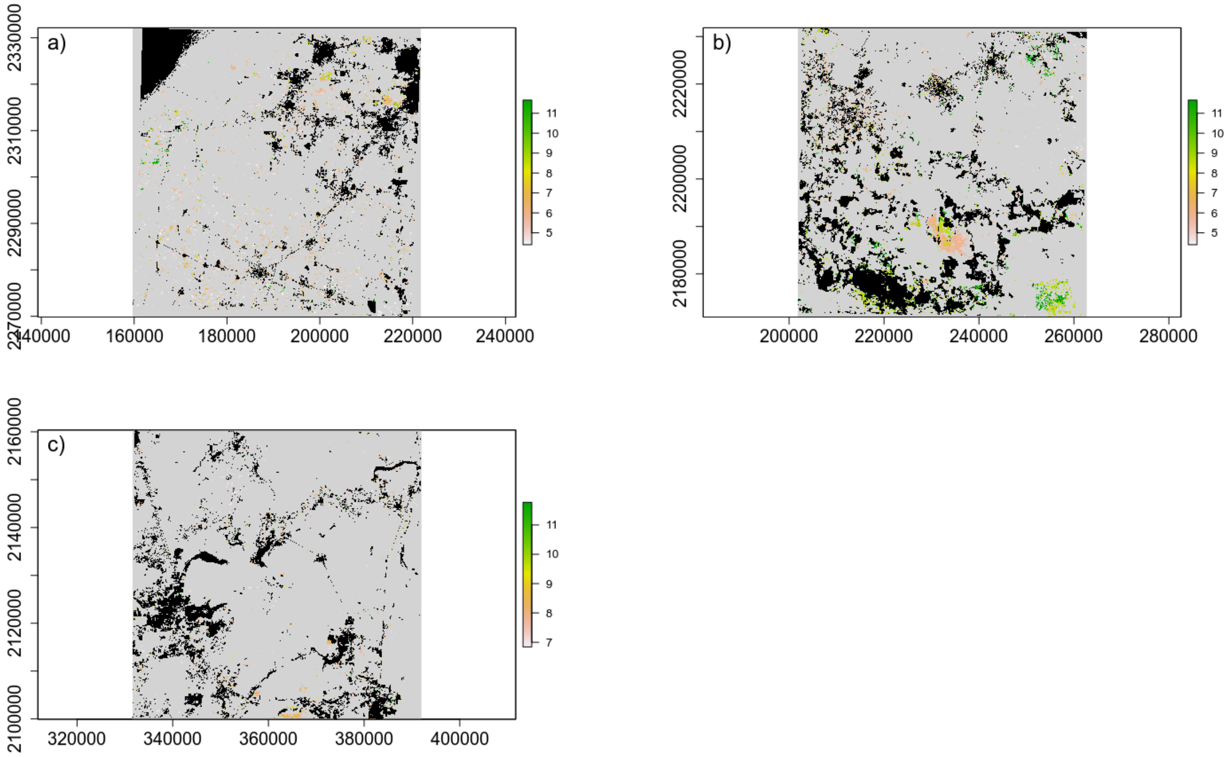

Frequency histograms showing the distribution of errors in the study sites.

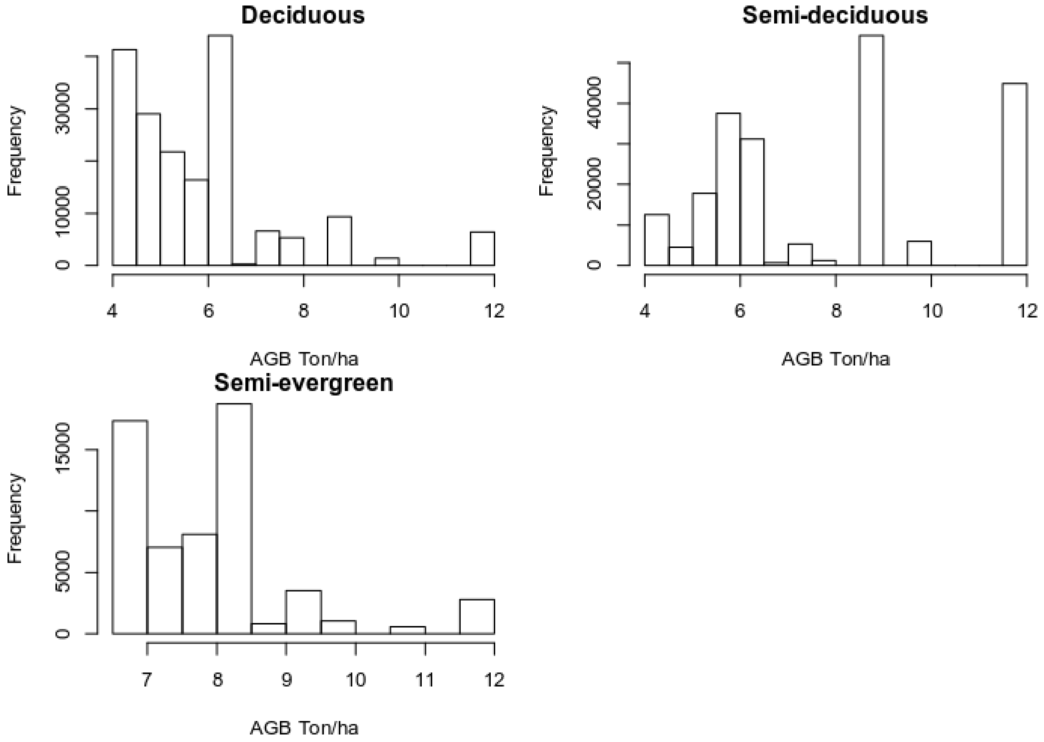

ANEXO 2

Material suplementario para el Capítulo 3.

Supplementary 1

Flowchart of methods described in this study. Parallelograms represent input data, while green boxes represent processes and output.

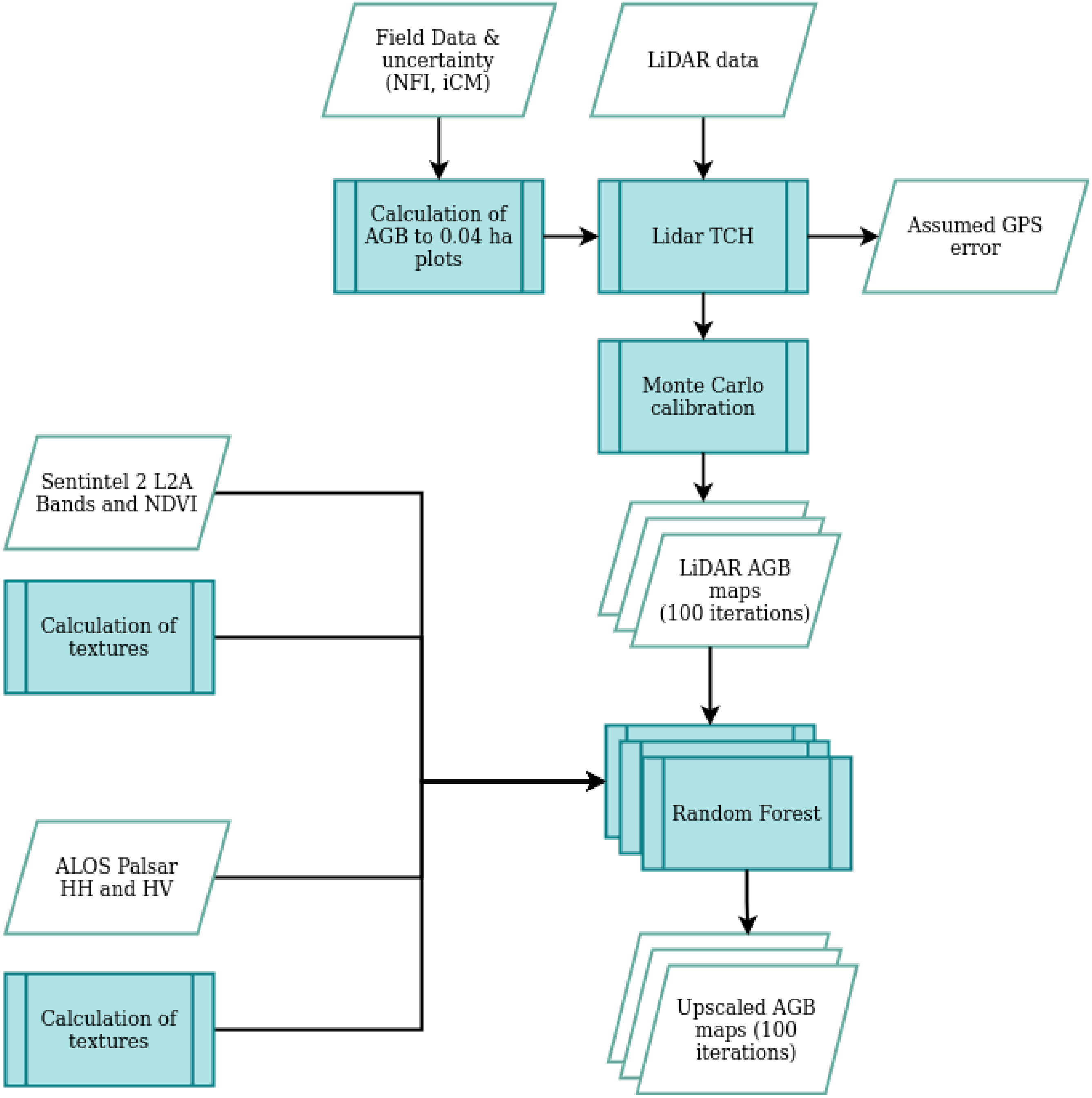

Supplementary Figure 2

Supplementary 1. Leave-One-Out (LOO) cross-validation of field AGB vs AGB modelled by TCH for 0.04 ha inventory plots.

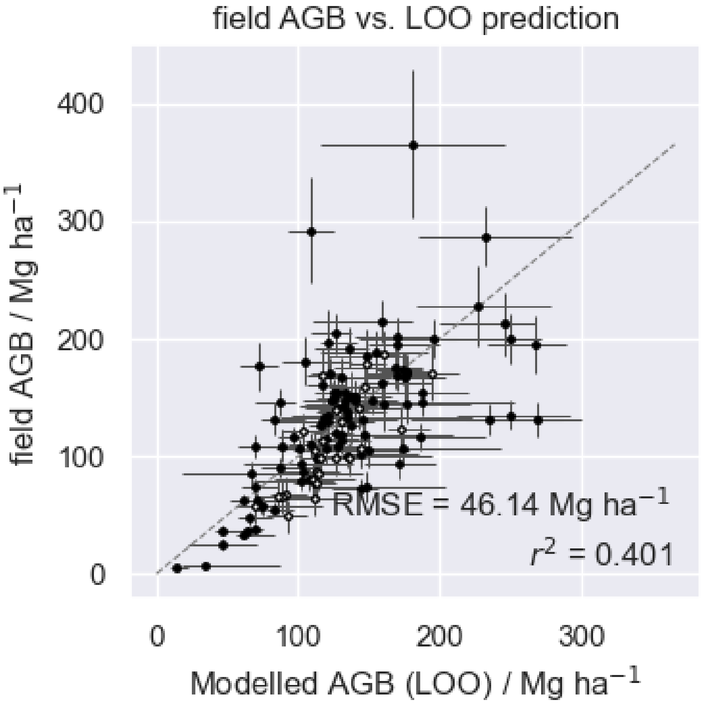

Supplementary Figure 3

Supplementary 2. Regression lines, R^2, RMSE and relative %RMSE based on a five-fold buffered-blocked cross-validation between LiDAR estimated AGB (AGB_{lidar}) and upscaled AGB ($AGB_{satellite}$) for models using both sensors in three different resolutions (20 m, 50 m and 100 m). The dashed line represents the 1:1 line, the solid and dotted lines represent the median estimate and 95% confidence interval for a 20 Mg ha^{-1} moving window across the predicted AGB range ($AGB_{satellite}$).